TEXTURE AND COMPOSITION OF AN ARID-CLIMATE WEATHERING PROFILE AND THE LINK BETWEEN BEDROCK AND DERIVED SEDIMENT COMPOSITION

A Thesis Presented for the

Master of Science

Degree

The University of Tennessee, Knoxville

Kristan L. Watkins

May 2022

ACKNOWLEDGEMENTS

First, I would like to thank my Mom and Dad for always being so supportive of my goals and helping me through school. Thank you to all my friends, and fur friends, I've made along the way because, without them, this process would have been impossible. I couldn't have done this without the help and support of my boyfriend, Damian, thank you so much for keeping me motivated to finish. Thank you to the Southeast Geological Society of America for the funding that made this project possible. I would also like to thank the entire Department of Earth and Planetary Sciences for their support and guidance during my time here at the University of Tennessee. Lastly, I would like to thank my advisor, Chris Fedo, for all his support, and the Fedo lab group for all the late-night group chat memes.

ABSTRACT

Multiple compositional aspects of Holocene, terrigenous-clastic sediment differ from its source, the underlying Cretaceous Stepladder granodiorite (Mojave Desert, California). Different processes can cause sediments to change in composition from source, including chemical weathering, hydrodynamic sorting during transport, and diagenesis. To assess the relative contributions of these processes to understand provenance reconstruction, the textures and compositions of an exposed Holocene saprolite weathering profile, grus, and granodiorite bedrock were studied. Fracture density in the weathering profile decreased from ~10% at the top to ~2% at the bottom of the profile in contact with the bedrock. The entire weathering profile was dominated mineralogically by plagioclase, potassium feldspar, and biotite. All phases showed evidence of chemical weathering through hydrolysis, and the alteration intensity was estimated using a semi-quantitative scoring system for three main minerals, plagioclase, potassium feldspar, and biotite, each showing various degrees of chemical weathering. Samples above the 70 cm depth break had a greater abundance of weathered plagioclase, while potassium feldspar and biotite showed minimal alteration throughout the profile. However, weathering profile samples had chemical index of alteration values that ranged from 53.5 to 56.5, which suggested minimal chemical weathering. Trace element concentrations in the profile showed slight enrichments relative to bedrock for some elements (Rb avg. 1.47 ppm; Sr avg. 1.24 ppm; Cs avg. 1.07 ppm; U avg. 2.10 ppm; Th avg. 1.24 ppm) and slight depletions for others (Ba avg. 0.86 ppm; Zr avg. 0.76 ppm; Y avg. 0.95 ppm; Hf avg. 0.83 ppm). Eu/Eu^*_{BN} was slightly positive (avg. 1.11). There was an overall negative slope (avg. 1.31) for rare earth element (REE) concentrations relative to bedrock, with light REE averaging 1.03 and heavy REE averaging 1.24. Consequently, results from this study indicate that the geochemical data for the saprolite

weathering profile do not directly match the source bedrock composition, and the sediment and bedrock compositions differ. Grus, the non-transported material that lies directly on top of the weathering profile, is compositionally the bridge between sediment and bedrock.

TABLE OF CONTENTS

SECTION 1. INTRODUCTION 1

SECTION 2. PROBLEM AND THESIS OVERVIEW 3

SECTION 3. GEOLOGIC SETTING 5

3.1 Geologic History 5
3.2 Climatic History 6
3.3 Generation of Stepladder Weathering Profile 6

SECTION 4. MATERIALS AND METHODS 9

4.1 Field Work 9
4.2 Sample Preparation 9
4.2.1 Petrographic Analysis 9
4.2.2 Geochemical Analysis 9
4.3 Technical Approach 13
4.3.1 Fracture Density 13
4.3.2 Quantifying Weathering Intensity 13
4.3.3 Caliche and CO_2 Calculations 17

SECTION 5. ANALAYSIS OF STEPLADDER BEDROCK 18

5.1 Petrology 18
5.1.1 Field and hand sample 18
5.1.2 Mineralogy 18
5.1.3 Weathering Textures 21
5.2 Geochemistry 21
5.2.1 Major Elements – Classification 21
5.2.2 Major Elements – Weathering 24
5.2.3 Trace Elements 26
5.2.4 Rare Earth Elements 26

SECTION 6. CHARACTERIZATION OF THE STEPLADDER WEATHERING PROFILE AND GRUS 34

6.1 Petrology 34
6.1.1 Textural Analysis 34
6.1.2 Mineralogy 37
6.1.3 Evidence for Weathering 37
6.2 Geochemistry 40
6.2.1 Major Elements 40
6.2.2 Trace Elements 42
6.2.3 Rare Earth Elements 47
6.3 Grus 49
6.3.1 Major Elements 49
6.3.2 Trace Elements 49
6.3.3 Rare Earth Elements 50
7.1 Compositional Homogeneity Within the Bedrock 51
7.2 Major Elements 51
7.2.1 A-CN-K and A-CNK-FM plots 51
7.3 Trace Elements 54
7.3.1 Incompatible vs. Compatible Element Plots 54
7.3.2 Discriminatory plots 54
7.4.1 REE Normalized to Stepladder Bedrock 56
7.4.2 REE vs Eu/Eu* 58

SECTION 8. DISCUSSION 59

SECTION 9. SUMMARY AND CONCLUSIONS 62

REFERENCES 65
APPENDICES 75
VITA 129

LIST OF TABLES

Table 1. Reference table for sample numbers. 10

Table 2. Alteration score criteria for plagioclase, K-feldspar and biotite. Scoring criteria based on Eswaran and Heng (1976) for biotite. 15

Table 3. Major element in weight percentages for all Stepladder samples. FeO (T) = Fe_2O_3 (T) x 0.8998. * denotes data from Modi (2011) study. – denotes element not analyized. 25

Table 4. Concentrations of trace and rare earth elements (in ppm) for Stepladder bedrock, grus, caliche, and the weathering profile. * denotes data from Modi (2011), which has a different significant values than data collected from this study. The instrument or method used for an analysis is listed with the detection limit for each element. † denotes element below detection limit. – denotes element not analyzed. 27

LIST OF FIGURES

Figure 1. (A) Thematic mapper image (which shows sediment that was sampled being the same red band as the Stepladder source) modified from Bonich-Wissink (2017) showing the northern end of the Stepladder Mountains and field site. Data from Modi (2011). (B) An aerial photo from Google Earth and showing the field area within the Stepladder pluton. The yellow box outlines the exposed weathering profile studied in this study. (C) Panoramic image of the entire weathering profile outcrop. 4

Figure 2. Potential hypothesis for the development of the Stepladder weathering profile. Zone 4 is minimally weathered and zone 1 is extremely weathered, as adapted from Nesbitt and Markovics (1997). (A) A weathering profile is a relic profile where the heavily weathered (of zones 1 through 3) have eroded away, to leave only zone 4 in the present-day. (B) A weathering profile developed in current climatic conditions (<10,000 years), with the top of the profile only starting to show evidence of weathering as zone 4. 7

Figure 3. **(**A) Outcrop images of stepladder weathering profile. (B) Weathering profile where sampling occurred with 0-7 corresponding to samples 0119SL_0 – 0119SL_7, respectively, and grus, sample 0119SL_13. 11

Figure 4. Fractures traced on to standard (2.5 cm x 5 cm) billets using Adobe Draw. Line thickness varies with varying fracture size. Images A to H correspond to samples 0 to 7, respectively. Larger images for A to I can be found in Appendix A. Note, sample 6 is pictured in the figure, but the data from this sample was not used because the sample broke apart during transport. Fracture area calculations from these data are shown in Appendix B1. The scale bar applies to all samples. 14

Figure 5. Images of the Stepladder bedrock. (A) Outcrop showing large scale fractures in bedrock. The yellow line indicates joint set 3 and the red lines indicate joint set 1. Joint set 2 not seen at this angle. Joint data are from Driscoll (2016). (B) Hand sample (19_SL_2), showing fresh granodiorite. (C) Outcrop showing small scale fractures within the bedrock (red lines).....19

Figure 6. Photomicrographs of the Stepladder pluton, showing the mineralogy and textures associated with the bedrock. Minimal clay is seen in plagioclase. Small-scale fractures are present (noted in blue, image A). Bt = biotite, qtz= quartz, pl = plagioclase feldspar, ksp = potassium feldspar, mt =magnetite. Areas outlined in green are clay, and yellow lines indicate zoning. Pink-lined areas show twins. (A) Plain polarized light (ppl) image showing twins, clay, fracturing, and common minerology. (B) Cross polarized light (xpl) image of image A. (C) Ppl photomicrograph showing main mineralogy and (D) Xpl image of image C. 20

Figure 7. (A) Fracture lines traced on fresh Stepladder bedrock. (B) CIA plot for all bedrock samples for the Stepladder mountains. A= Al_2O_3, CN = CaO + Na_2O, K = K_2O, kao = kaolinite, gi = gibbsite, chl = chlorite, sme = smectite, ill = illite, pl = plagioclase, kfs = potassium feldspar, ton = tonalite, di = diorite, grd = granodiorite, gr = granite, bas = basalt, cal = calcite. (C) Plagioclase weathering score. (D) Potassium feldspar weathering score. (E) Biotite weathering score.....22

Figure 8. Geochemical plots characterizing the Stepladder pluton. (A) Histogram of major elements in Stepladder pluton samples in weight percent. (B) Total alkalis versus silica diagram ($Na_2O + K_2O$ vs SiO_2) for all bedrock samples. (C) Aluminum, iron, and magnesium (AFM) plot for determining calc-alkaline vs tholetic rocks. (D) N + K + Ca vs Si to classify bedrock samples into calc-alkalic and alkali-calcic compositions.....23

Figure 9. Trace element and rare earth element plots for unweathered Stepladder pluton. ST09-02 and CF00-18 are data from Modi (2011). (A) Trace elements normalized to McLennan (2001). (B) REEs normalized to chondrite for each bedrock sample. Chondrite values from Anders and Grevesse (1989). (C) Bedrock samples normalized to average Post-Archean Australian Average Shale (PAAS; McLennan, 1989). 32
Figure 10. Samples collected from the Stepladder weathering profile. (A) Weathering profile with sample localities marked, 0 – 7 and corresponding to C – J. (B) Grus collected from the top of the weathering profile (sample 0119SL_13). (C) Sample 0119SL_0. (D) Sample 0119SL_1. (E) Sample 0119SL_2. (F) Sample 0119SL_3. (G) Sample 0119SL_4. (H) Sample 0119SL_5. (I) Sample 0119SL_6. (J) Sample 0119SL_7. Larger images of each sample can be found in Appendix A. 35
Figure 11. Percent fracture area vs. depth along the weathering profile. The red box denotes samples that had a high fracture density (> ~8 %) and individual samples are marked in warm colors. The blue box denotes samples with a low fracture density (< 6 %) and are shown with cool colors. Sample 19_SL_2 (average bedrock) is marked in black for comparison. 36
Figure 12. Photomicrographs of the main mineral phases from the Stepladder weathering profile samples. Bt = biotite, qtz= quartz, pl = plagioclase feldspar, ksp = potassium feldspar, mt =magnetite, ap = apatite, ep =epidote, chl= chlorite. Outlines in green denote clay, lines in blue denote fracturing, outlines in yellow denote zoning, and outlines in pink denote twins. (A) Sample 0119SL_0 (5 cm) in xpl. (B) Sample 0119SL_0 (5 cm) in ppl. (C) Sample 0119SL_3 (75 cm) in xpl (D) Sample 0119SL_3 (75 cm) in ppl. (E) Sample 0119SL_7 (140 cm) in xpl. (F) Sample 0119SL_7 (140 cm) in ppl. 38
Figure 13. Distribution of scored for weathered mineral phases, plagioclase, K-feldspar, and biotite, respectively (in columns from left to right). Warm colors on the histogram represent samples with high fracture density and cool colors show low fracture density. Weathering intensity was scored on a scale of 1 to 5 for plagioclase feldspar, 1 to 3 for K-feldspar, and 1 to 3 for biotite. Black stars indicate average scores for each sample. (A) Sample 0 scores. (B) Sample 1 scores. (C) Sample 2 scores. (D) Sample 3 scores. (E) Sample 4 scores. (F) Sample 5 scores. (G) Sample 6 scores. (H) Sample 7 scores. 39
Figure 14. Major oxide weight percent (wt%) vs. depth for samples collected from the saprolite weathering profile. The red dashed lines indicate the average bedrock composition. The red shaded boxes represent one standard deviation from the average bedrock composition. 41
Figure 15. Plots modified from Nesbitt and Young (1984, 1989) for the Stepladder pluton and saprolite weathering profile. (A) A-CN-K plot for Stepladder bedrock (black square), weathering profile, and grus. A= Al_2O_3, CN = CaO + Na_2O, K = K_2O, kao = kaolinite, gi = gibbsite, chl = chlorite, sme = smectite, ill = illite, pl = plagioclase, kfs = potassium feldspar, ton = tonalite, di = diorite, grd = granodiorite, gr = granite, bas = basalt, cal = calcite. (B) Transition from sample to sample based on their location in the weathering profile, marked by arrows. (C) A-CNK-FM plot for Stepladder bedrock (black square), weathering profile, and grus. (D) Arrows indicate order from top of the profile (1) to bottom of the profile (7) A= Al_2O_3, CNK = CaO + Na_2O + K_2O, FM = FeO(t) + MgO, kao = kaolinite, gi = gibbsite, chl = chlorite, sme = smectite, ill = illite, ms =

muscovite, pl = plagioclase, kfs = potassium feldspar, cal = calcite, hbl = hornblende, bt = biotite, px = pyroxene, ol = olivine. 43
Figure 16. Trace element spider plots for stepladder weathering profile. (A) Weathering profile samples normalized to bedrock. (B) Weathering profile normalized to the average Stepladder sediment composition from Modi (2011) and Driscoll (2016). (C) The Stepladder weathering profile normalized to grus. Not shown are Co, Cr, Ni, Cu, and As because their concentrations were below detection limits. 44
Figure 17. Bedrock-normalized trace elements vs depth (cm) for (A) high field strength elements (HFSE), Y = yttrium, Zr = zircon, Hf = hafnium, Nb = niobium. (B) large ion lithophiles elements (LILE), Rb = rubidium, Ba = barium, Cs = cesium, Sr = strontium. (C) transition metals, V = vanadium, Zn = zinc. (D) and U (uranium) Th (thorium) Pb (lead). 46
Figure 18. (A) Weathering profile rare-earth elements normalized to average bedrock. Transparent lines represent stepladder sediment from Modi (2011) and Driscoll (2016). (B) Weathering profile REEs normalized to Post-Archean Australian Shale (PAAS; McLennan, 1989). 48
Figure 19. (A) Average bedrock normalized (ABN) total REEs vs. Eu/Eu * ABN for all bedrock samples used to create average bedrock. Data for ST09-02 and CF00-18 come from Modi (2011). The range in bedrock compositions was used to create grey boxes in all of the plots, which are effectively error bars within 0.05 of the average value. The grus and saprolite weathering profile samples are compositionally comparable to bedrock. (B) Total REEs ABN vs. Eu/Eu * ABN for sediment from Modi (2011) and Driscoll (2016). Pastel orange represents data from Modi (2011) and pastel green represents samples from Driscoll (2016). (C) Total REEs ABN vs. Eu/Eu * ABN results for the weathering profile samples and grus. (D) All samples plotted together. 52
Figure 20. Figures from Modi (2011) indicating compositional variation in the sediment. (A) Zr – Al_2O_3 (x15) – TiO_2 (x300) ternary diagram from Garcia et al. (1994) showing sediment maturity. (B) Cr/V vs Y/Ni plot showing basaltic mixture present in sediment (McLennan et al., 1993) end members from Condie (1993). (C) Cr vs Ni plot also indicating multiple sources for the Stepladder sediment (Taylor and McLennan, 1985), end members from Condie (1993). (D) La/Th vs Hf plot to identify source of clastic sediment (Floyd and Leveridge, 1987). 53
Figure 21. Ratios of incompatible and compatible trace element concentrations (in ppm). Black circles indicate groups of like patterns drawn around Stepladder pluton data, weathering profile data, and sediment data (Modi, 2011; Driscoll; 2016). (A). Th/Sc vs. Sc plot for sediment, weathering profile, grus, and bedrock. (B) La/Th vs. Hf. (C) Th/Ta vs. Yb. (D) Zr vs. SiO_2 wt% for bedrock, weathering profile, grus, and sediment. (E) Y vs. SiO_2 wt%. (F) Rb vs. SiO_2 wt%. 55
Figure 22. Plot modified from Floyd and Leveridge (1987). La/Th vs Hf ppm diagram indicating the range of sources for the Stepladder sediment (Modi, 2011; Driscoll, 2016), grus, and weathering profile into saprolite. 57

SECTION 1. INTRODUCTION

Provenance reconstruction of sediment and sedimentary rocks can determine past tectonic and climatic histories (Johnsson, 1993) by using sediment and whole-rock mineralogy, geochemistry, isotope geochemistry, and geochronology (e.g., Taylor and McLennan, 1985; Cullers et al., 1988; Condie et al., 1992; Johnsson 1993; Fedo et al., 2003; Descourvieres et al., 2011; Schoenborn and Fedo, 2011; Um et al., 2013; Zhang et al., 2014). However, although source rocks should exert the primary control on the composition of derived sediment (Johnsson, 1993), the mineralogy and geochemistry of sediment or a sedimentary rock may not represent the source rock (Nesbitt and Young, 1989; Rainbird et al., 1990; Nesbitt, 1992; Fedo et al., 1995; Cox et al., 1995; Fedo et al., 1997; Medaris et al., 2015; Novoselov and de Souza Filho, 2015). In sedimentary geology and provenance reconstruction research, determining the reasons why there are compositional differences between sediment and source rock is a fundamental challenge.

Chemical weathering, diagenesis, mechanical weathering, and hydrodynamic sorting during transport have been used to explain why sediment and source-rock compositionally differ (e.g., Nesbitt and Young 1989; Rainbird et al., 1990; Fedo et al., 1995). Abundant research has been done to understand the effects of chemical weathering on bedrock and during temporary storage of sediment in exposed settings during transport (e.g., Suttner et al., 1981; Johnsson et al., 1988; Stewart, 1990; Johnsson, 1993; Nesbitt and Young, 1996; Nesbitt and Markovics, 1997; Xiong et al., 2010). Hydrolysis of silicate mineral phases is one of the most critical processes involved in the production and compositional modification of siliciclastic sediment relative to source rocks, as hydrolysis results in the production of clay and changes in mobile-element (Ca, Na, K, P, Sr, Rb, Ba, Mg, Si) abundances and release into solution (Nesbitt and

Young, 1984; Nesbitt and Young, 1989). Silicate hydrolysis reactions are most effective in tectonically stable settings that are also in hot and humid climates, where extreme changes in bedrock compositional modifications have been documented (Nesbitt and Young, 1996; Nesbitt and Markovics, 1997; Olivia et al., 2003; Norton et al., 2014). Intense chemical weathering can also exist in humid temperate climates over long periods of time in stable tectonic settings that permit reactions to go to completion. Albitization can also cause sediment to differ compositionally from a source rock (Kastner and Siever, 1979; Van de Kamp and Leake, 1997), and metasomatism causes unpredictable geochemical signatures that do not follow observed weathering trends, and thus would incorrectly identify the amount of weathering that the rock may have experienced (e.g., Fedo et al., 1995). Once sediment enters the transport system, density-based hydrodynamic sorting can separate mineral phases and produce sediment compositions with different grain size populations that deviate compositionally from each other and the source (e.g., McLennan et al., 1993; Nesbitt and Young, 1996; Fralick, 2003; McLennan et al., 2006; Mangold et al., 2011; Fedo et al., 2015). For example, Nesbitt and Young (1996), studying modern sediment transport in the Guys Bight Basin, Canada, found quartz and feldspar concentrated in coarse sand, but biotite and other accessory minerals concentrated in fine-grained sands, which resulted in differences in both major- and trace- elements relative to grain size and with respect to source bedrock. Fralick (2003) also determined that accessory minerals will sort with increasing distance from source into fine-grained sediments during transport. In the absence of chemical weathering (i.e., temperature too low for effective chemical weathering), Nesbitt and Young (1996) found that abrasion, even after extreme mechanical weathering (i.e., glacial comminution), did not change the composition of sediment.

SECTION 2. PROBLEM AND THESIS OVERVIEW

Because hot, arid climates lack a sustained presence of water needed for hydrolysis, the hypothesis is that only minimal compositional change between sediment and source rock would occur, such that sediment should be compositionally similar to its source, and especially sediment that has experienced little to no transport for hydrodynamic sorting. Several research projects done in the Stepladder Mountains, California (Fig. 1A; Modi, 2011; Driscoll, 2016; Bonich-Wissink, 2017) have addressed this hypothesis to determine the accuracy of common provenance-seeking geochemical tools used to match sediment to its granodiorite source in a setting where extensive external controls governing composition modification (e.g., chemical weathering, diagenesis, and a complex source) are minimalized or well characterized. However, these studies found significant differences between sediment and source rock compositions, including sediment that experienced short transport distances. Their findings collectively call into question various aspects of the geochemical "toolbox," and lead to the hypothesis that the compositional changes may develop before sediments enter the transport system.

This thesis research tests this hypothesis by analyzing the petrology and chemistry of a meter thick weathering profile on the Stepladder pluton and its overlying unlithified active sediment carapace (i.e., saprolite; Fig. 1B, 1C). Study of the saprolite weathering profile composition removes any concerns about potential influences from transport while also permitting identification of compositional changes related to hydrolysis or other chemical processes.

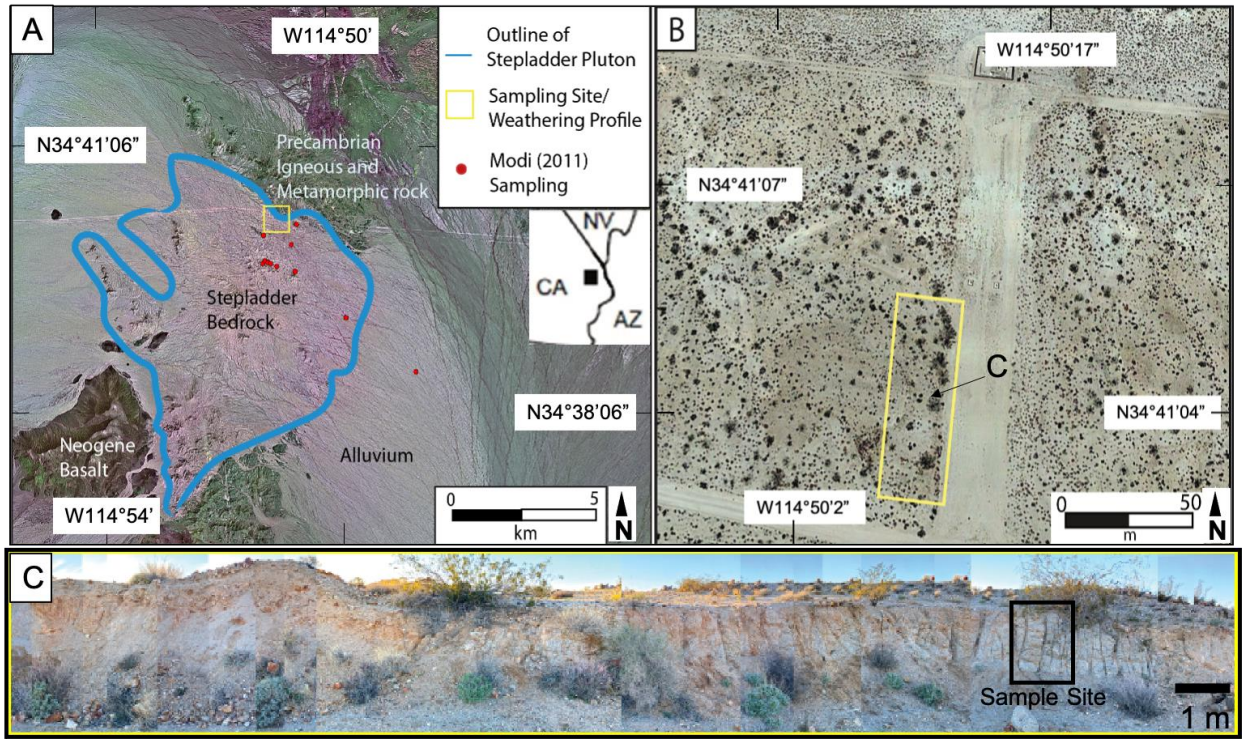


Figure 1. (A) Thematic mapper image (which shows sediment that was sampled being the same red band as the Stepladder source) modified from Bonich-Wissink (2017) showing the northern end of the Stepladder Mountains and field site. Data from Modi (2011). (B) An aerial photo from Google Earth and showing the field area within the Stepladder pluton. The yellow box outlines the exposed weathering profile studied in this study. (C) Panoramic image of the entire weathering profile outcrop.

SECTION 3. GEOLOGIC SETTING

3.1 Geologic History

The oldest basement rocks in the eastern Mojave Desert are granitic gneisses that were deformed during the Ivanpah orogeny [~1.71–1.69 billion years ago (Ga); Dewitt et al., 1984; Wooden and Miller, 1990; Barth et al., 2000; Duebendorfer et al., 2001; Barth et al., 2009]. Of the Paleoproterozoic deformation events in the Mojave Desert, the ~1.7 Ga gneiss is a part of the middle stage of metamorphic events, with pre-orogenic to post-orogenic events existing from 1.79 Ga to 1.65 Ga (Wooden and Miller, 1990; Barth et al., 2000; Duebendorfer et al., 2001; Barth et al., 2009; Strickland et al., 2013). Other Proterozoic rocks found in the field area include ~1.4 Ga potassic-rich granites (Anderson, 1983; Anderson and Bender, 1989), which occur as xenoliths in the Stepladder pluton. This suite of granites is different from most orogenic granites but correlates with A-type granites spread across North America (Goodge and Vevoort, 2006). After assembly of the basement terrane at about 1.1 Ga, the region experienced rift-through-passive-margin formation associated with the breaking apart of the supercontinent Rodina (Prave, 1999).

Resting nonconformably upon the basement complex is a succession of Neoproterozoic through Paleozoic siliciclastic and carbonate rocks that document this rifting of Rodina and transition to passive margin (e.g., Fedo and Cooper, 2001). Following the deposition of this succession, regional tectonism began in the Jurassic and extended into the Cretaceous. Tectonism started in the Middle to Late Jurassic (Foster et al., 1992) with intrusions emplaced from 145-160 million years ago (Ma; Gerber et al., 1991; Kingsbury et al., 1993). Granitic intrusions spread across the Mojave as early as 110 Ma (Allen, 1992; Miller and Wooden, 1994). Following the emplacement of the Lower Cretaceous and Jurassic pluton, regional metamorphism began with a

new flux of increased magmatism (Anderson and Cullers, 1999), recognized as the Laramide orogeny (75 to 35 Ma; Bird, 1998). The Stepladder pluton, which has been dated at 74.1 Ma (Foster et al., 1990; Bonich-Wissink, 2017), intruded during this event.

Miocene continental extension in the Colorado River extensional corridor (Burchfiel and Davis, 1981) occurred along listric normal faults and exhumed 10–15 km of crust (Howard and John, 1987), including raising the Stepladder pluton to the surface. Widespread basaltic and rhyolitic volcanism accompanied Basin-and-Range extension (Burchfiel and Davis, 1981; Spencer 1985). Extension and block rotation, along with active volcanism and sedimentation, ended at about 14 Ma (Foster et al., 1991) and generated the modern-day geomorphology of the eastern Mojave Desert, including exposure of the Stepladder pluton.

3.2 Climatic History

Near the end of the Pleistocene [2.58 Ma – 12 thousand years ago (ka)], climate began to warm. This marked the end of the last northern hemisphere glacial advance (Nichols, 2005). The Mojave Desert during this time was not covered in ice, but global climatic change resulted in increased rainfall (Stoffer, 2004; Hereford et al., 2006), which could have provided the conditions needed for chemical weathering to occur. Since the end of the last glacial maximum, the climate in eastern California has continued to become hotter and more arid, leading to present conditions (Hereford et al., 2006) that include current average annual temperatures of ~24 °C and annual rainfall of less than 9 cm/yr (National Park Service, 2016; U.S. Climate Data, 2019).

3.3 Generation of Stepladder Weathering Profile

There are two potential hypotheses for the development of the Stepladder weathering profile (Fig. 2). First, as illustrated in Figure 2A, a thick, well-developed weathering profile that

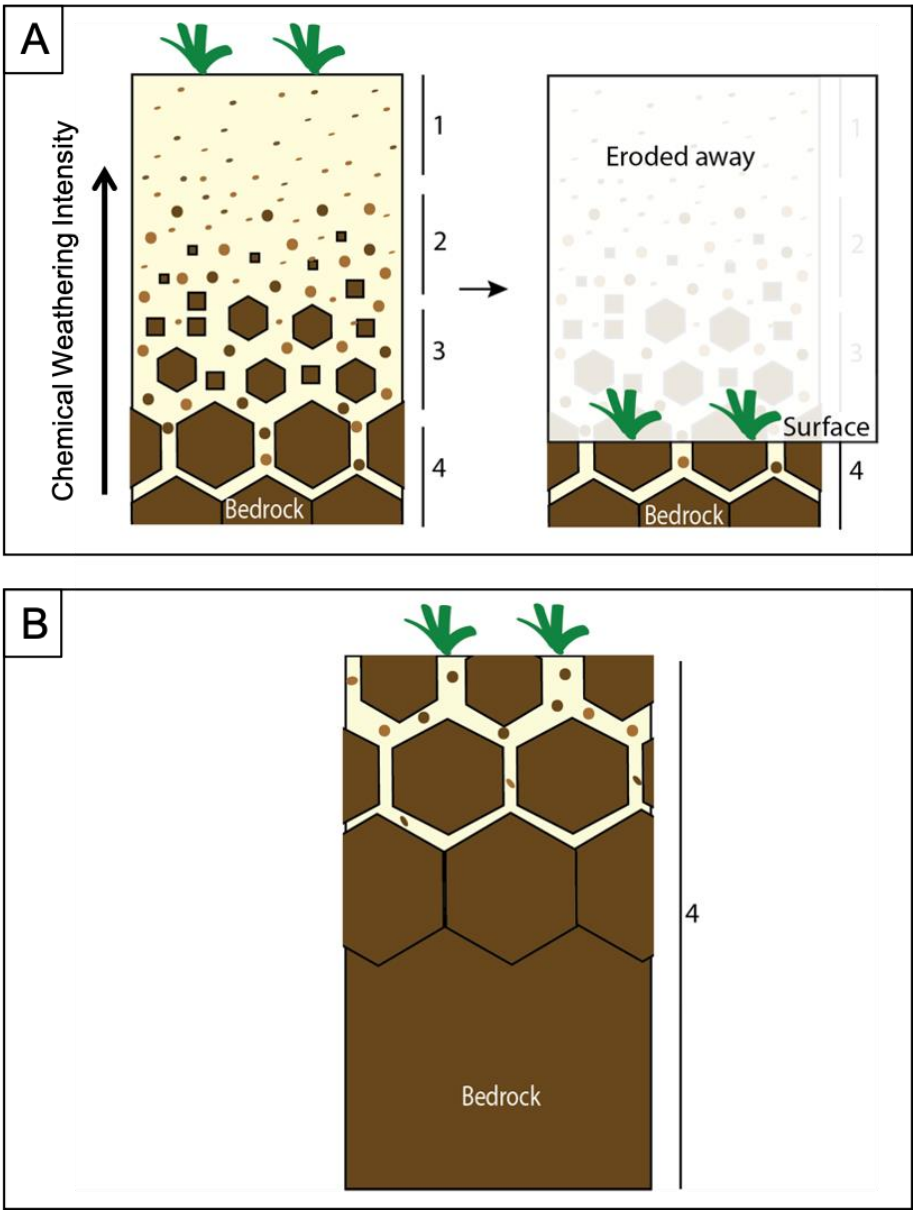


Figure 2. Potential hypothesis for the development of the Stepladder weathering profile. Zone 4 is minimally weathered and zone 1 is extremely weathered, as adapted from Nesbitt and Markovics (1997). (A) A weathering profile is a relic profile where the heavily weathered (of zones 1 through 3) have eroded away, to leave only zone 4 in the present-day. (B) A weathering profile developed in current climatic conditions (<10,000 years), with the top of the profile only starting to show evidence of weathering as zone 4.

could have formed during wetter times prior to the present arid climate of the Mojave Desert. The four geochemical zones, from least to most weathered, represent the corestone zone (4), exfoliate zone (3), incompetent zone (2), and soil zone (1), according to the nomenclature of Nesbitt and Markovics (1997). Zone 4, the corestone zone, is characterized by semi-spherical boulders of unweathered rock with its original igneous texture, separated by fractures where incipient hydrolysis occurs. The exfoliate zone has thickened, clay-filled fractures that separate the corestone into pieces with their original igneous textures. Mineralogically, clays tend to be immature and accompanied by kaolinite from plagioclase hydrolysis. The incompetent zone is also referred to as the texture clay zone and consists of small bedrock clasts, but mostly comprised individual mineral phases with increased clay content. Lastly, zone 1, the soil zone, consists of massive fracture-fill clay and accumulation of refracturing sand-sized phases (e.g., quartz, zircon, iron-oxides). Plagioclase is completely converted to clays, Fe^{+2} rich phases are mostly oxidized to Fe^{+3}, and potassium-bearing feldspars show incipient alteration to clay. In tectonically stable settings, each higher zone would consume the underlying zone as weathering proceeds and would result in a zone 1 that has no compositional resemblance to the unweathered igneous rock over time. However, the present-day Stepladder weathering profile has zone 4 is at the surface. One of the hypothesized results for this profile would be that after development of all four zones, the upper zones would have eroded away until zone 4 was at the surface.

In contrast, the second hypothesis (Figure 2B) represents a modern-day weathering profile that developed in equilibrium with current arid conditions. Regardless of how the profile formed, the results are the same: a thin, minimally weathered profile exposed at the surface from which sediments are presently being drawn from.

SECTION 4. MATERIALS AND METHODS

4.1 Field Work

Table 1 depicts the sample numbers, depth, and fracture density for each of the nine samples (0 – 7 and 13) collected from a vertically-exposed weathering profile, ~100 m from a road (Fig. 3A). Samples were collected about every ~20 cm (Fig. 3B). Grus, non-transported detritus sitting atop the profile, was sampled directly above sample 0. Fresh bedrock was also collected. Additionally, a caliche sample from the large fractures throughout the exposed profile was collected. Samples were carefully removed from the weathering profile, wrapped in foil, and closed with tape to retain rock texture and prevent disintegration.

4.2 Sample Preparation

4.2.1 Petrographic Analysis

Intact pieces of the saprolite (Appendix A1 – 10) were impregnated with epoxy to stabilize the material and fill pore space, then cut into a billet. The bedrock sample did not need to be impregnated. Billets were sent to Spectrum Petrographics in Vancouver, Canada and were prepared into standard, 30 μm thick, singly polished 2.5 x 5 cm thin sections.

4.2.2 Geochemical Analysis

Remaining sample material was crushed into pebble-sized grains or smaller, either by hand because of the friable texture or by using a rubber mallet. Each crushed sample was subsampled using a modified cone-and-quarter method (Appendix A11). Reduced-volume samples were placed into a ceramic dish and powdered in a SPEX Shatterbox for four minutes (Appendix A12). Between each sample the ceramic dish was thoroughly cleaned to make sure no cross-contamination occurred. Each sample made between 35 g to 70 g of powder. An

Table 1. Reference table for sample numbers.

Sample #	Sample Reference #	Depth (cm) from top of the profile	Fracture Density (described in Section 4.3.1)	Notes
0119SL_13	13	0	n/a	Grus, no fracture density test on sediment
0119SL_0	0	5	abundant	
0119SL_1	1	20	abundant	
0119SL_2	2	40	abundant	
0119SL_3	3	75	limited	
0119SL_4	4	85	limited	
0119SL_5	5	105	limited	
0119SL_6	6	125	n/a	Sample broken during transport, could not do fracture density
0119SL_7	7	150	limited	
19_SL_2	Br	n/a	limited	Fresh bedrock
19_SL_5	Caliche	n/a	n/a	Caliche collected from inside a fracture in the profile

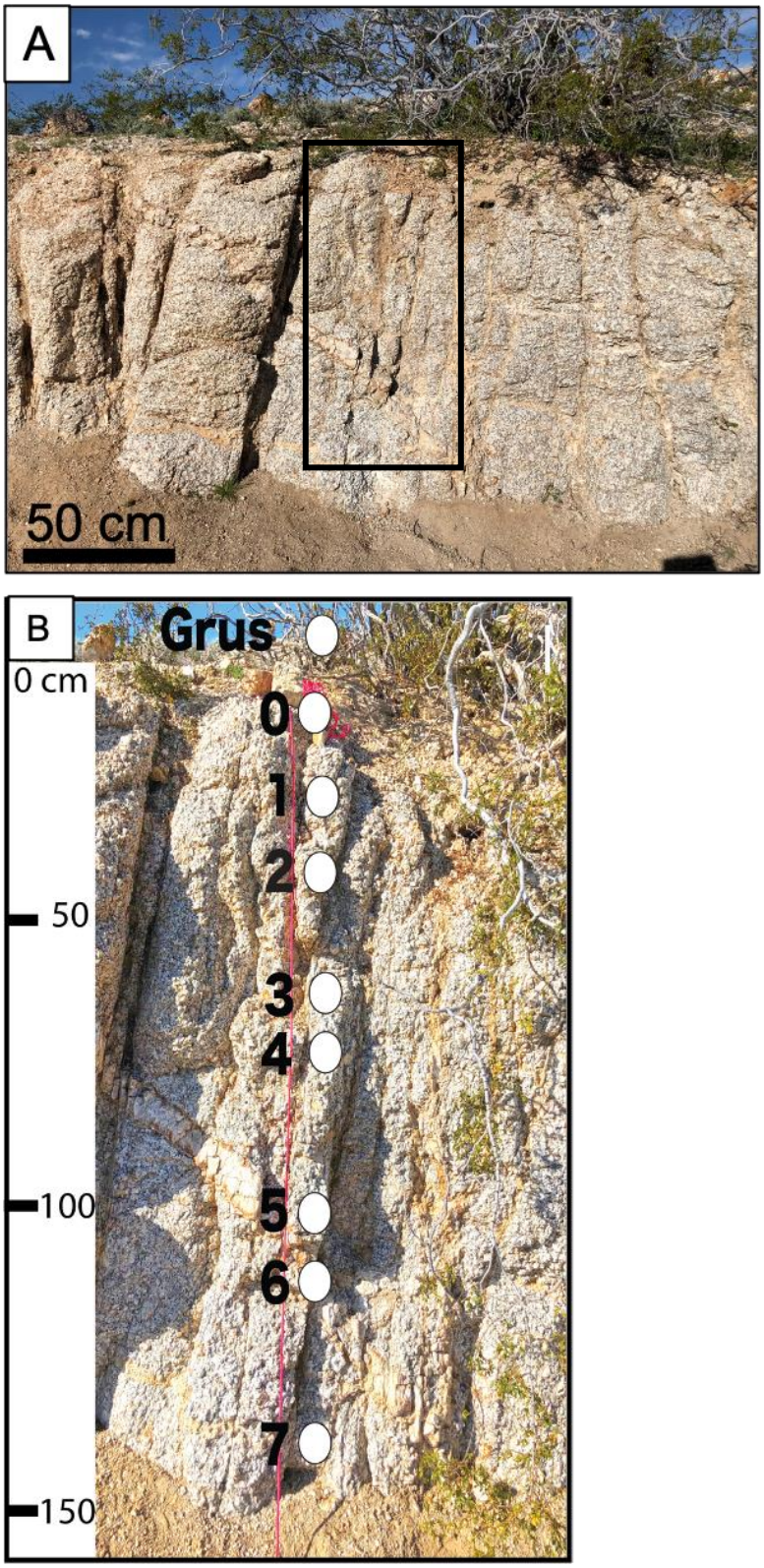


Figure 3. **(**A) Outcrop images of stepladder weathering profile. (B) Weathering profile where sampling occurred with 0-7 corresponding to samples 0119SL_0 – 0119SL_7, respectively, and grus, sample 0119SL_13.

approximate aliquot of 10 g of powder for each sample was sent to Activation Laboratories (Actlabs, Ltd., Ontario, Canada) for geochemical analysis. Duplicate samples of fresh bedrock, sample 4, and USGS standard RGM-1 (Glass Mountain rhyolite) were re-numbered and analyzed blindly at Actlabs to test the reproducibility of digestions and comparison with a known reference standard (Govindaraju, 1994). Duplicate samples, along with standard error calculation for each element, are in Appendix s B1 – B3. Activation Laboratories also ran standards and duplicate analyses of solutions to determine machine reproducibility.

Trace-element (TE) compositions (including the rare earth elements) are important for provenance reconstruction because they can identify a range of igneous source compositions (McLennan and Taylor, 1980; McLennan, 1989; McLennan et al., 1993; Munksgaard et al., 2003; Eker et al., 2012) and their low solubilities cause quantitative transfer to the sedimentary record (e.g., Taylor and McLennan, 1985). Rare earth elements (REE) divide into two groups that behave differently from one another, specifically light REE (LREE, La through Sm) and heavy REE (HREE, Gd through Lu), separated by europium (Eu). Both Ce and Eu behave differently from other REEs because each have two redox states (Eu^{+3} and Eu^{+4}, and Ce^{+2} and Ce^{+3}). Europium (II) substitutes for Ca^{+2} in plagioclase.

As outlined in Actlabs procedures for the 4LithoResearch analytical package, samples were digested using a multi-acid digestion process to ensure all elements went into solution for inductively coupled plasma mass spectrometry (ICP-MS) analyses. The base analysis package used on the samples was lithium metaborate/tetraborate fusion ICP whole rock (FUS-MS) and trace element ICP-MS (4B2-Research). Each sample was analyzed by a Perkin Elmer Sciex ELAN 6000, 6100, or 9000 ICP-MS. “Geochemical analyses have an expected precision of ± 1% at ≥100x the detection limit…for trace levels of metals and base metals generally less than 20%”

(ActLabs, 2021). Five of the fourteen samples were also analyzed by Instrumental Neutron Activation Analysis (INAA) using the 4B-INAA package to lower the detection limits for many trace elements, including transition metals Cr, Co, Ni, and Cu.

4.3 Technical Approach

4.3.1 Fracture Density

Determining a value for the fracture density in each saprolite sample quantified the physical changes in samples from the weathering profile. High-resolution images of each thin section billet were used to document fracture area in each sample using Adobe Draw (Fig. 4). Fracture sizes vary in width, which was accounted for to track fracture area properly. Using software package Image J (https://imagej.nih.gov/ij/), the total areas of a billet and its fractures were calculated to determine percent fracture area (Appendix B4). The average and standard deviation for each fracture density score were also determined and reported.

4.3.2 Quantifying Weathering Intensity

Alteration is documented on three main mineral phases that comprise the pluton and could be estimated visually, specifically plagioclase feldspar ($NaCaAlSi_3O_8$), potassium feldspar ($KAlSi_3O_8$), and biotite. Plagioclase alters to kaolinite ($Al_2Si_2O_5(OH)_4$) according to the following reaction (Hemley and Jones, 1964; Equation 1):

$$NaCaAlSi_3O_8 + 2H^+ + 9H_2O \rightarrow Al_2Si_2O_5(OH)_4 + 2Na^+(aq) + 2Ca^+(aq) + 4H_4SiO_4\,(aq) \quad \text{Eq. 1}$$

Plagioclase crystals accumulate secondary clays as micrometer-sized crystals (Banfield and Eggleton, 1990). This alteration was scored visually on a one-to-five scale (Table 2, Appendix

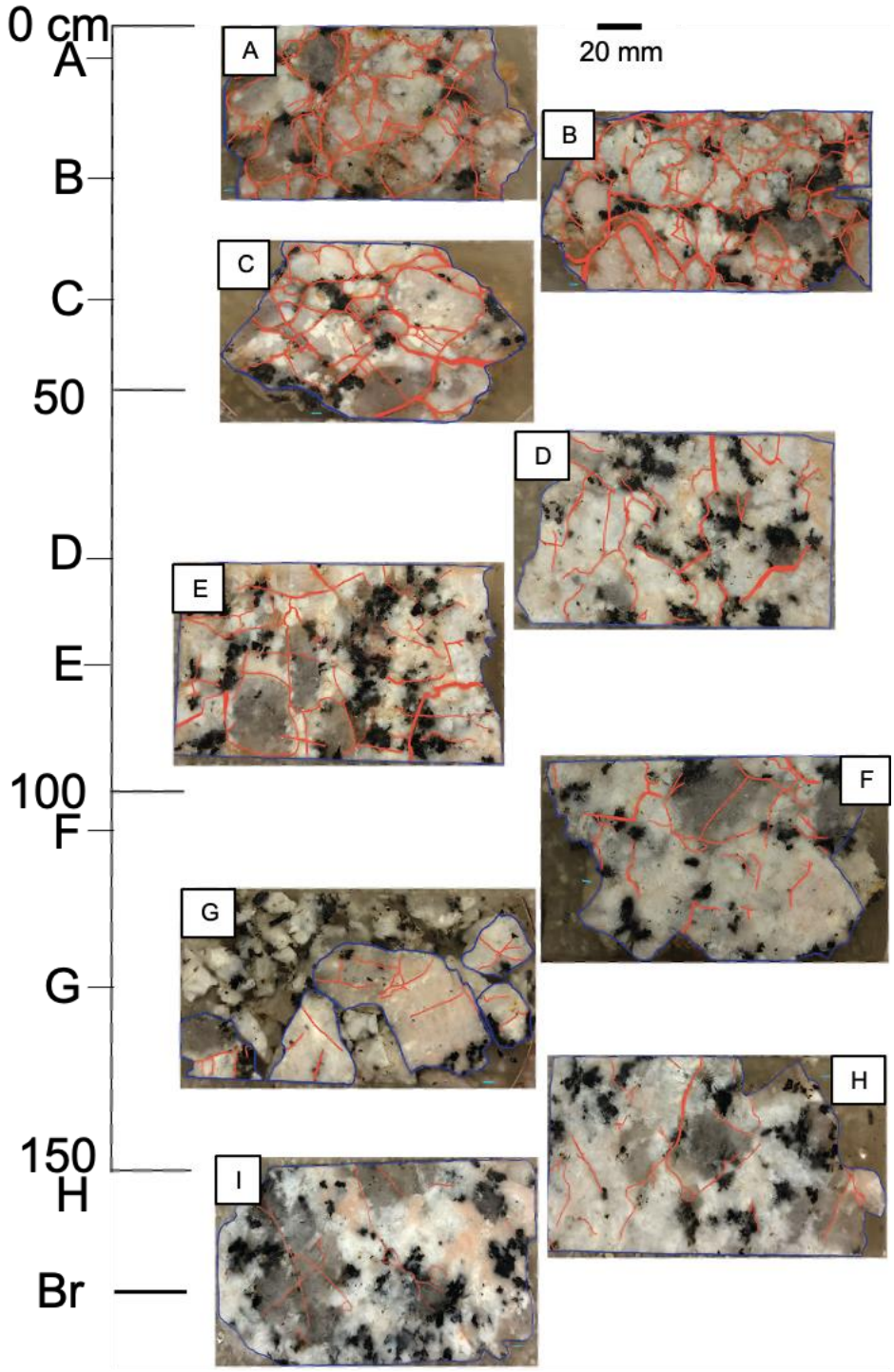


Figure 4. Fractures traced on to standard (2.5 cm x 5 cm) billets using Adobe Draw. Line thickness varies with varying fracture size. Images A to H correspond to samples 0 to 7, respectively. Larger images for A to I can be found in Appendix A. Note, sample 6 is pictured in the figure, but the data from this sample was not used because the sample broke apart during transport. Fracture area calculations from these data are shown in Appendix B1. The scale bar applies to all samples.

Table 2. Alteration score criteria for plagioclase, K-feldspar and biotite. Scoring criteria based on Eswaran and Heng (1976) for biotite.

Score	Plagioclase	K-Feldspar	Biotite
1	Limited to no clay alteration along cleavage planes Limited to no clay alteration along fractures Limited surface alteration Original grain shape intact	Minor clay alteration along sodium- rich twin planes Limited to no clay alteration along fractures No surface alteration Original grain shape intact	Minor to no chloritization Interference colors are normal No loss of pleochroism Birds eye extinction present
2	Minor clay alteration along cleavage planes Minor clay alteration along fractures Minor to no surface alteration Original grain shape intact	Minor clay alteration along sodium- rich twin planes Minor clay alteration along fractures Minor surface alteration Original grain shape intact	Minor to moderate chloritization Minor decrease in interference colors Minor loss of pleochroism Birds eye extinction present
3	Moderate clay alteration along cleavage planes Moderate clay alteration along fractures Minor to moderate surface alteration Original grain shape intact	Moderate clay alteration along sodium- rich twin planes Minor to moderate clay alteration along fractures Minor to moderate surface alteration Original grain shape intact	Moderate chloritization Decrease in interference colors Loss of pleochroism Loss of birds-eye extinction
4	Moderate to high clay alteration along cleavage planes Moderate to high clay alteration along fractures Moderate to high surface alteration Original grain shape intact	n/a	n/a
5	High clay alteration along cleavage planes High clay alteration along fractures Complete surface alteration Original grain shape intact	n/a	n/a

A21). A score of 1 would represent a nearly pristine plagioclase grain, where clay alteration was barely present, whereas a score of 5 would represent plagioclase that is completely altered (converted to clay) to where only the grain shape remained. Each of the scored minerals selected on each sample can be found in Appendix A22 – 29. The average and standard deviation of values for each sample are noted in Appendix B5.

Potassium feldspar alters to illite [$1/3KAl_3Si_3O_{10}(OH)_2$] via hydrolysis; after additional weathering, illite converts to kaolinite in the following reactions (Thyne et al., 2001; Equations 2 and 3):

$$KAlSi_3O_8 + 2/3H^+ \rightarrow 1/3KAl_3Si_3O_{10}(OH)_2 + 1/3\ K^+ + SiO_2\,(aq) \qquad \text{Eq. 2}$$

$$2/3KAl_3Si_3O_{10}(OH)_2 + 2/3H^+ \rightarrow Al_2Si_2O_5(OH)_4 + 2/3\ K^+ + H_2O\ (aq) \qquad \text{Eq. 3}$$

Alkali feldspar was scored on a scale of one to three because the range of the alteration was less extensive than plagioclase (Table 2; Appendix A30). A score of 1 would indicate minor clay alteration on sodic-rich planes, no surface alteration, and grain shape remains intact, whereas a score of 3 would represent moderate alteration along sodic rich twin planes and minor alteration along fractures and surface area. In each scoring, the original grain shape is present.

Biotite also was scored on a scale of one to three. Scoring criteria for weathered biotite are based on work from Eswaran and Heng (1976), which states initial weathering of biotite is seen by buckling of lamellae, loss of pleochroism, and lowering of interference colors. The scoring rubric is: 1, minor chlorite alteration; 2, some loss of pleochroism or slight decrease in interference colors; 3, loss of pleochroism, lowering of interference colors, and loss of birds-eye extinction (Table 2; Appendix A31). After scoring each grain in each sample, the score averages and standard deviations were calculated (Appendix B5).

4.3.3 Caliche and CO_2 Calculations

As is common in arid settings (Schlesinger, 1982), caliche (comprised predominately of calcite, $CaCO_3$) is present in the Stepladder weathering profile as fracture fills. Additionally, sediment derived from the pluton has clasts of caliche that derive from the fracture fills (Modi, 2011). Due to the systematic loss of calcium in silicate hydrolysis (Eq. 1), it is important to ensure that calcium data represent only that from igneous silicate phases. Therefore, an iterative compositional mixing model using the average CO_2 weight percent (wt%) for caliche (30.6 wt%) and bedrock (0 wt%) was created in 0.02% increments from 0% to 10% (Appendix B7). The results of the mixing model produced a wt% CO_2 that was used to compare calculated CO_2 content in the weathering profile and eliminate values that could have been contributed from caliche ($CaCO_3$) that locally fills fractures in the weathering profile and shows up as clasts in the sediment (e.g., Modi, 2011). As explained in detail in Modi (2011), the value for lost on ignition (LOI, $H_2O + CO_2$). Lost on ignition (LOI) was used to calculate CO_2 content for all samples. Assuming all LOI in unaltered bedrock would be due to water, the following equation was used to calculate CO_2 (Equation 4):

$$\text{wt \% LOI}_{\text{sample}} - \text{wt \% LOI}_{\text{bedrock}} = \text{wt \% CO}_2 \qquad \text{Eq. 4}$$

SECTION 5. ANALAYSIS OF STEPLADDER BEDROCK

Characterizing the Stepladder pluton mineralogy and chemistry was necessary to compare to the composition of the saprolite. Figure 5 illustrates examples of the Stepladder pluton. Geochemical values from three pluton samples were compiled into an average bedrock value because there was minimal variation among the samples. Petrographic images and fracture density analysis of bedrock are solely from the sample collected for this study.

5.1 Petrology

5.1.1 Field and hand sample

Desert varnish locally covers the Stepladder pluton (Fig. 5A), yielding a brown color that masks the fresh color of the granodiorite (Fig. 5B). Large scale (Fig. 5A) and small scale (Fig. 5C) fractures crosscut the bedrock. Driscoll (2016) measured the joint sets in the Stepladder pluton outcrops: (1) NE strike with a steep SE dip, (2) NW strike with a steep NE dip, and (3) a NE strike with a shallow westward dip (Fig. 5A, B). Figure 5B shows the bedrock sample, used for this study and taken from the outcrop in Figure 5C, which had no apparent desert varnish.

5.1.2 Mineralogy

Modi (2011) and Driscoll (2016) classify the Stepladder pluton as a coarse-grained, hypidiomorphic biotite granodiorite from Quartz-Alkali feldspar-Plagioclase (QAP) diagrams (Appendix C1). Average modal composition, described by the detailed study of Modi (2011), was 42% plagioclase feldspar, mainly oligoclase, 28% quartz, 25% potassium feldspar, and 5% biotite. Figure 6 depicts the best representation of the sample from this study, but not all mineral phases and accessory minerals together in one image. Accessory minerals, comprising less than 1% of total mineralogy, included apatite, zircon, magnetite, titanite, hematite, rutile, allanite, and epidote (Modi, 2011).

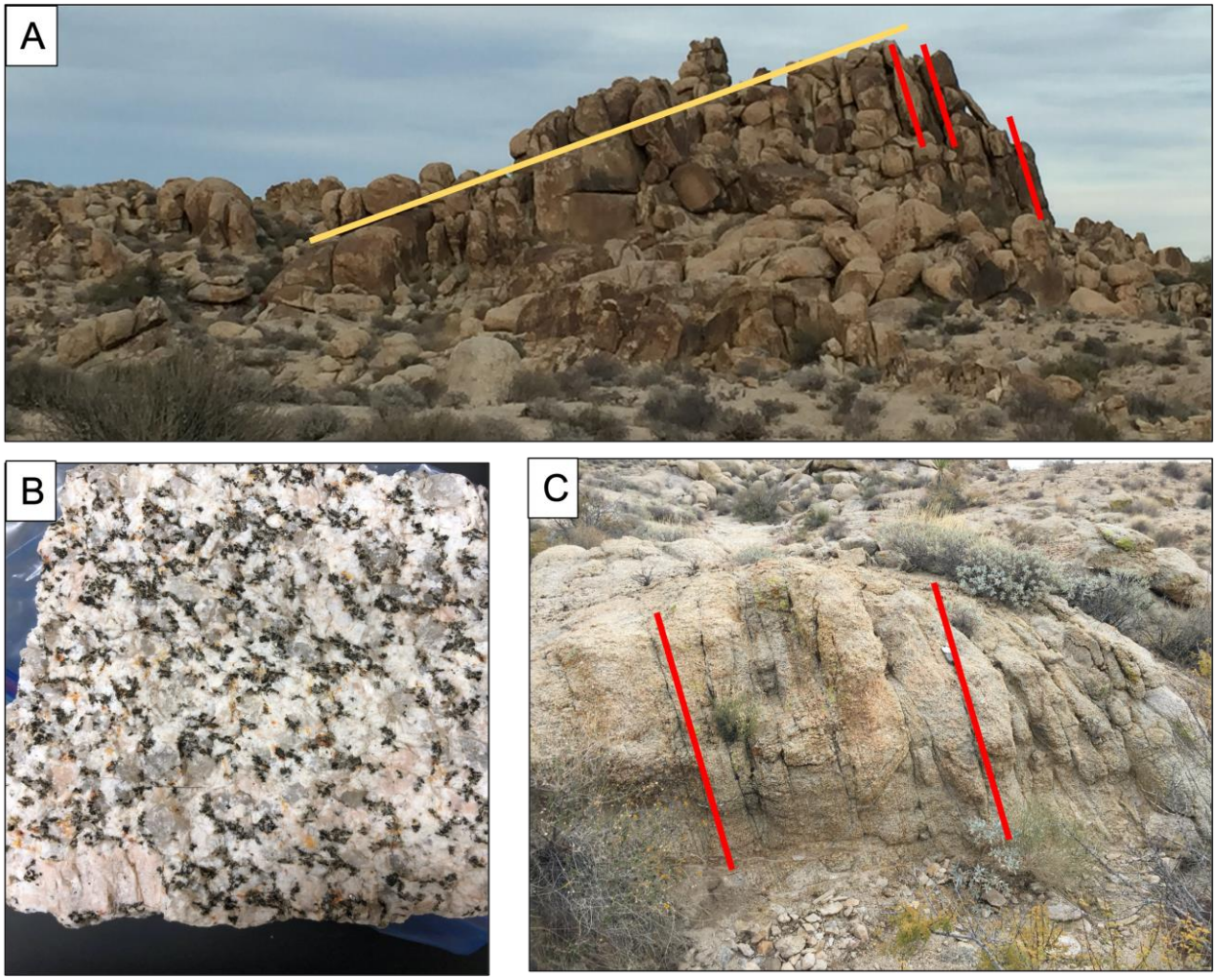


Figure 5. Images of the Stepladder bedrock. (A) Outcrop showing large scale fractures in bedrock. The yellow line indicates joint set 3 and the red lines indicate joint set 1. Joint set 2 not seen at this angle. Joint data are from Driscoll (2016). (B) Hand sample (19_SL_2), showing fresh granodiorite. (C) Outcrop showing small scale fractures within the bedrock (red lines).

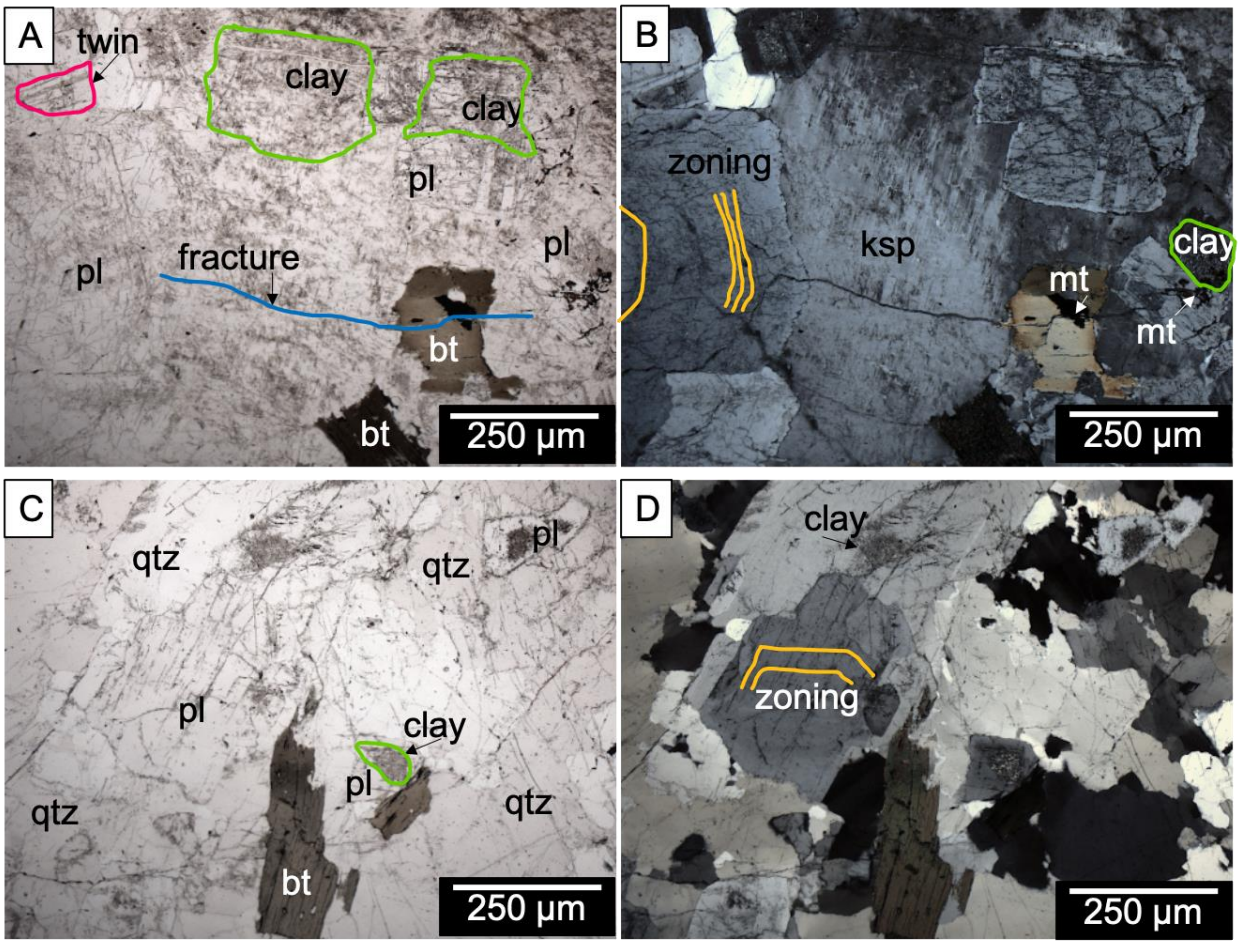


Figure 6. Photomicrographs of the Stepladder pluton, showing the mineralogy and textures associated with the bedrock. Minimal clay is seen in plagioclase. Small-scale fractures are present (noted in blue, image A). Bt = biotite, qtz= quartz, pl = plagioclase feldspar, ksp = potassium feldspar, mt =magnetite. Areas outlined in green are clay, and yellow lines indicate zoning. Pink-lined areas show twins. (A) Plain polarized light (ppl) image showing twins, clay, fracturing, and common minerology. (B) Cross polarized light (xpl) image of image A. (C) Ppl photomicrograph showing main mineralogy and (D) Xpl image of image C.

Plagioclase grains throughout the bedrock exhibited oscillatory zoning (Fig. 6B, D) and albite-law twinning (Fig. 6B). Secondary clay minerals occurred along cleavages (Fig. 6B), zones and twin planes (Fig. 6B). Mrymekitic texture on plagioclase occurred in some contacts with alkali feldspar. In locations where poikilitic plagioclase was included in K-feldspar, clay alteration was greater (Fig. 6B). Quartz mostly exhibited undulatory extinction and occurred as a monocrystalline phase, polycrystalline aggregates, and interstitial grains. Biotite typically occurred as an interstitial or poikilitic grains (Fig. 6B, D). Accessory phases were located interstitially or poikilitic in main phases.

5.1.3 Weathering Textures

There should be minimal weathering evidence from the fresh mineral phases in unexposed bedrock, but weathering intensity of the Stepladder granodiorite was collected from (1) fracture density and (2) alteration textures of weatherable phases to provide a baseline for comparison. The bedrock hand sample had <1% fractures from the total billet area (Fig. 7A; Appendix A20; Appendix B1), although fracture sets could be seen at the outcrop-scale (Fig. 5A, 5B). Plagioclase, K-feldspar, and biotite were scored in the bedrock sample to compare with the weathering profile data (Appendix C3 – C5). The plagioclase score was 1.2 ± 0.4 (Fig. 7B), K-feldspar score was 1.4 ± 0.5 (Fig. 7C), and the biotite score was 2 ± 0.8 (Fig. 7D). These values were expected for bedrock.

5.2 Geochemistry

5.2.1 Major Elements – Classification

Data from Modi (2011), along with the bedrock sample from this study, were used to create an average bedrock composition. Major-element (ME) concentrations are noted in Figure 8A and illustrate the compositional similarity among the samples. Frost et al. (2001) compiled all

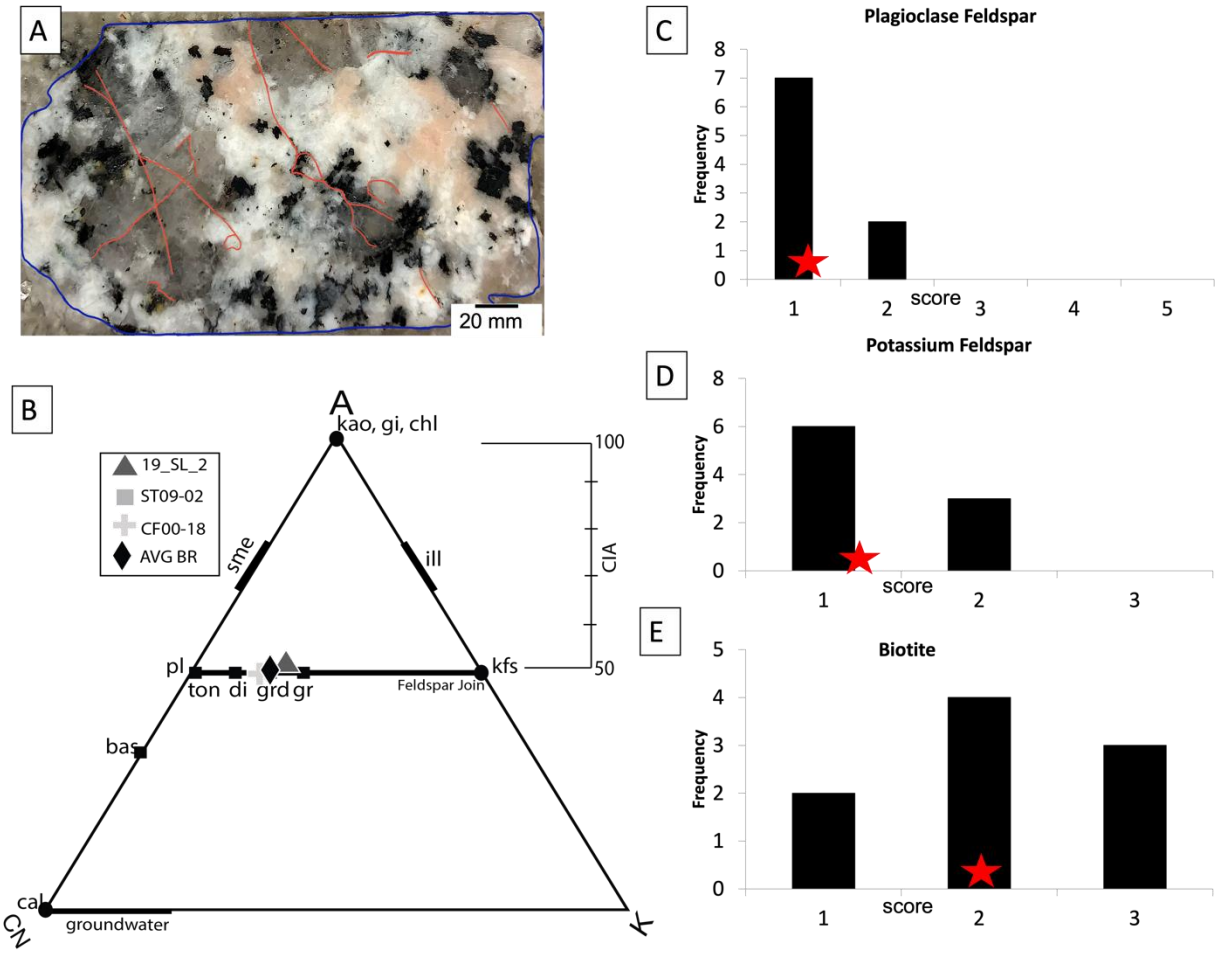


Figure 7. (A) Fracture lines traced on fresh Stepladder bedrock. (B) CIA plot for all bedrock samples for the Stepladder mountains. A= Al_2O_3, CN = CaO + Na_2O, K = K_2O, kao = kaolinite, gi = gibbsite, chl = chlorite, sme = smectite, ill = illite, pl = plagioclase, kfs = potassium feldspar, ton = tonalite, di = diorite, grd = granodiorite, gr = granite, bas = basalt, cal = calcite. (C) Plagioclase weathering score. (D) Potassium feldspar weathering score. (E) Biotite weathering score.

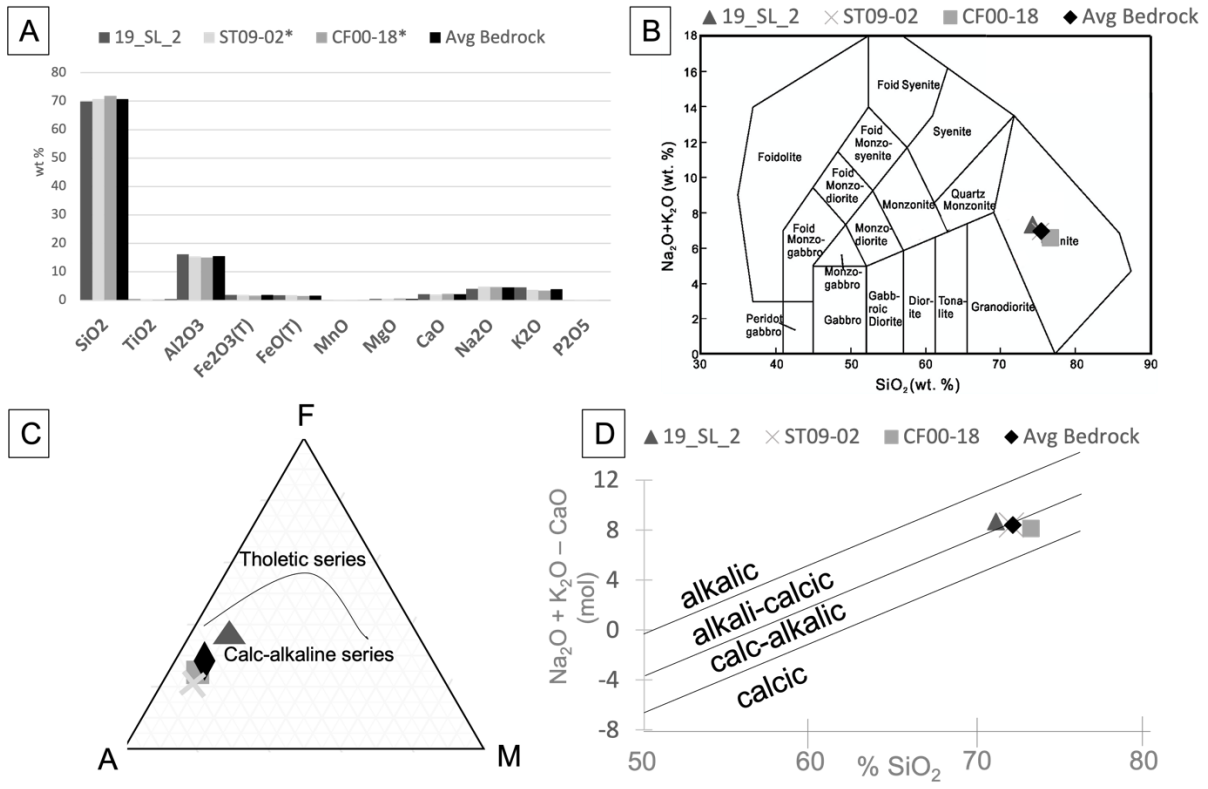


Figure 8. Geochemical plots characterizing the Stepladder pluton. (A) Histogram of major elements in Stepladder pluton samples in weight percent. (B) Total alkalis versus silica diagram ($Na_2O + K_2O$ vs SiO_2) for all bedrock samples. (C) Aluminum, iron, and magnesium (AFM) plot for determining calc-alkaline vs tholetic rocks. (D) N + K + Ca vs Si to classify bedrock samples into calc-alkalic and alkali-calcic compositions.

the useful geochemical tools to classify granites based on ME geochemistry. Using the Fe number (Fe number = FeO / FeO + MgO; Miyashiro, 1970), the Stepladder pluton values ranged from 0.71 – 0.76, with the average at 0.74 (Appendix B8), and classified as magnesian, similar to Cordilleran-type granites (Chappell and White, 1974). However, there was a buffer above and below, and these values fell within the ferroan range. Next, the Aluminum Saturation Index (ASI; ASI= Al/Ca – 1.67P + Na + K; Shand, 1943) identified the Stepladder pluton as a peraluminous granite because the average value was greater than unity (Zen, 1988; Appendix B2). Lastly, the Modified Alkali Lime Index (MALI; MALI = $Na_2O + K_2O$ - CaO; Peacock, 1931) determined the rock samples were alkali-calcic to calc-alkalic granite (Fig. 8B –8D), but the average composition classified the Stepladder pluton as an alkali-calcic granite. Using the values from Appendix B8, C1, and C2, the Stepladder pluton samples obtained for this study were classified as a magnesian peraluminous alkali-calc granodiorite.

5.2.2 Major Elements – Weathering

The effects of chemical weathering was determined from the chemical index of alteration (CIA) value, calculated by using molecular proportions (Equation 5):

$$CIA = [Al_2O_3 / (Al_2O_3 + CaO^* + Na_2O + K_2O)] \times 100 \quad \text{Eq. 5}$$

where CaO* is the amount of calcium in silicate minerals (Nesbitt and Young, 1982). All continental crustal rocks have unweathered CIA values of ~50 (Fedo et al., 1995), the value of both plagioclase and K-feldspar, and that indicates no loss of labile cations through chemical weathering (Fedo et al., 1995). Because CIA is a one-dimensional characteristic that describes a complex system, the Al_2O - $CaO^* + Na_2O$- K_2O (A-CN-K) plot, was created to better track the effects of chemical weathering (Fig. 7E; Nesbitt and Young 1984;1989; Nesbitt, 1992; Fedo et al., 1995). Chemical Index of Alteration values greater than 85 indicate extreme chemical

Table 3. Major element in weight percentages for all Stepladder samples. FeO (T) = Fe_2O_3 (T) x 0.8998. * denotes data from Modi (2011) study. – denotes element not analyzed.

Sample	Depth (cm)	SiO_2	TiO_2	Al_2O_3	Fe_2O_3 (T)	FeO (T)	MnO	MgO	CaO	Na_2O	K_2O	P_2O_5	CO_2	% Caliche	LOI	Total
Grus																
0119SL_13	0.00	66.56	0.39	15.81	2.30	2.07	0.04	0.79	3.21	3.88	3.82	0.15	2.80	0.09	3.40	102.91
Weathering Profile																
0119SL_0	5.00	72.94	0.26	14.23	1.24	1.12	0.02	0.41	1.92	3.61	4.11	0.10	0.59	0.02	1.19	100.50
0119SL_1	20.00	70.40	0.33	15.66	1.89	1.70	0.03	0.61	2.26	4.36	3.51	0.08	0.78	0.03	1.38	101.11
0119SL_2	40.00	69.36	0.36	15.71	1.99	1.79	0.03	0.67	2.06	3.87	3.96	0.08	0.92	0.03	1.52	100.33
0119SL_3	75.00	70.15	0.35	15.43	1.82	1.64	0.04	0.65	2.02	4.01	3.82	0.10	0.96	0.03	1.56	100.72
0119SL_4	85.00	71.42	0.32	15.46	1.58	1.42	0.03	0.59	2.15	4.34	3.25	0.12	0.75	0.02	1.35	101.20
0119SL_5	105.00	69.37	0.36	16.02	1.76	1.58	0.04	0.69	2.55	4.49	3.43	0.13	0.98	0.03	1.58	101.22
0119SL_6	125.00	71.11	0.29	15.31	1.50	1.35	0.03	0.45	2.06	3.88	4.45	0.10	0.62	0.02	1.22	100.87
0119SL_7	150.00	68.31	0.40	15.99	2.04	1.84	0.04	0.81	2.94	4.32	3.33	0.16	1.29	0.04	1.89	101.32
Bedrock																
19_SL_2	-	69.85	0.34	16.22	1.93	1.74	0.04	0.53	2.13	4.08	4.60	0.13	-	-	0.62	100.28
ST09-02*	-	70.71	0.33	15.38	1.93	1.74	0.03	0.57	2.09	4.76	3.63	0.11	-	-	0.85	100.20
CF00-18*	-	71.84	0.31	15.09	1.68	1.51	0.03	0.61	2.27	4.66	3.45	0.10	-	-	0.65	100.52
Avg Bedrock	-	70.80	0.33	15.56	1.85	1.66	0.03	0.57	2.16	4.50	3.89	0.11	-	-	0.71	100.33
Caliche																
19_SL_5	-	13.51	0.12	3.60	0.82	0.74	0.02	0.47	43.7	0.71	1.13	0.10	35.16	1.00	35.76	135.02
*CF00-01	-	26.02	0.57	1.91	0.98	0.88	0.02	3.74	31.3	0.05	0.44	0.11	26.04	1.00	34.78	125.87
Avg Caliche	-	19.77	0.35	2.76	0.90	0.81	0.02	2.11	37.51	0.38	0.79	0.11	30.60	1.00	35.27	130.45

weathering occurred via the hydrolysis of feldspars. High CIA values in A-CN-K space will plot near the A apex and represent the accumulation of clays at the expense of feldspars (Nesbitt and Young, 1982, 1984; Fedo et al., 1995). The CIA values for Stepladder pluton samples are shown in Figure 7E and listed in Table 3. Bedrock values, including those from Modi (2011), range from 49.7 – 51.53, yielding an average CIA of 50.5 (Appendix B6), which is expected for unaltered bedrock (Fig. 7E).

5.2.3 Trace Elements

Stepladder bedrock samples normalized to upper continent crust (values from McLennan, 2001) show minor depletions in Cs, U, Y, Ta, and V and large depletions in Co, Cr, Sc, Ni and Zn (Fig. 7A). From the previous work done on this area, some transition metals fell below detection limit and therefore could not be used to compare sediment to bedrock (Modi, 2011; Driscoll, 2016). Although this study used INAA, which has lower detection limits for some transition metals (e.g., Co, Cr, Ni, and Cu), these elements remained below detection (Table 4, Fig. 9A).

5.2.4 Rare Earth Elements

Figure 9B is a chondrite-normalized REE plot with the data from Modi (2011) and this study. A slight negative Eu anomaly relative to chondrite was observed, with Eu/Eu* values ranging from 0.80 – 1.09 (Fig. 9B). Additionally, there was a negative Ce anomaly in all bedrock samples relative to chondrite (Fig. 9B), which is likely caused from the oxidation of Ce^{3+} to Ce^{4+} (Braun and Pagel, 1994). The LREE in chondrite normalized space had a negative slope (La/Sm = 5.49), with slight separation in concentration amongst the bedrock samples (Fig. 9B). The HREE also had a negative slope (Gd/Lu = 2.70), but the slope was not as steep as LREE (Fig. 9B).

Table 4. Concentrations of trace and rare earth elements (in ppm) for Stepladder bedrock, grus, caliche, and the weathering profile. * denotes data from Modi (2011), which has a different significant values than data collected from this study. The instrument or method used for an analysis is listed with the detection limit for each element. † denotes element below detection limit. – denotes element not analyzed.

	Element	Rb	Ba	Cs	Sr	Co	Cr	Sc	Y
	Instrument	FUS-MS	FUS-ICP	FUS-MS	FUS-MS	INAA	INAA	FUS-ICP	FUS-MS
	Detection Limit	1	2	0.1	2	1	5	1	0.5
Grus	0119SL_13	107	947.0	1.3	520	†	6	4	10
Weathering profile	0119SL_0	101	1245	0.9	510	†	†	2	7.2
	0119SL_1	106	580.0	1.2	526	-	-	3	6.6
	0119SL_2	111	970.0	1.1	517	-	-	3	5.8
	0119SL_3	113	806.0	1.3	505	†	†	3	5.4
	0119SL_4	95.0	609.0	1.2	508	-	-	3	5.2
	0119SL_5	108	812.0	1.1	547	-	-	3	5.4
	0119SL_6	112	993.0	0.6	533	-	-	2	4.8
	0119SL_7	104	602.0	1.0	527	†	†	4	5.4
Bedrock	19_SL_2	127	1383	1.0	571	†	†	3	5.7
	*ST09-02	46.60	872.11	1.04	348.31	1.14	1.75	0.63	6.65
	*CF00-18	42.53	615.92	0.90	342.28	1.29	1.26	0.61	5.68
	Avg Bedrock	72.04	957.01	0.98	420.53	1.14	2.67	1.41	6.01
Caliche	19_SL_5	30.0	441.0	0.5	220	†	†	2	9.5
	*CF00-01	7.53	334.14	0.20	1208.61	4.13	13.49	2.36	2.79
	Avg Caliche	18.76	387.57	0.35	714.30	2.57	9.24	2.18	6.14

Table 4 *(cont.)*

	Element	Th	U	Pb	Zr	Hf	Nb	Ta	V
	Instrument	FUS-MS	FUS-MS	FUS-MS	FUS-ICP	FUS-MS	FUS-MS	FUS-MS	FUS-ICP
	Detection Limit	0.1	0.01	5	1	0.1	0.2	0.01	5
Grus	0119SL_13	15.2	2.06	20	187	5.8	6.7	0.38	37
Weathering profile	0119SL_0	5.48	0.86	19	100	4.0	4.1	0.26	20
	0119SL_1	8.78	1.09	20	128	3.9	5.9	0.37	28
	0119SL_2	10.9	1.37	20	127	3.9	5.7	0.35	28
	0119SL_3	9.11	1.26	20	142	3.8	7.3	0.36	25
	0119SL_4	6.83	0.91	19	112	3.2	5.1	0.27	24
	0119SL_5	10.2	1.41	19	121	3.3	5.9	0.28	26
	0119SL_6	6.02	0.89	21	125	3.6	4.7	0.23	23
	0119SL_7	12.4	1.53	20	126	3.7	6.3	0.30	29
Bedrock	19_SL_2	7.90	1.08	22	130	3.8	5.6	0.35	29
	*ST09-02	9.33	0.32	10.00	151.60	4.06	7.40	0.45	22.94
	*CF00-18	3.89	0.26	10.67	188.81	5.38	7.44	0.50	20.53
	Avg Bedrock	7.04	0.55	14.22	156.80	4.41	6.81	0.43	24.15
Caliche	19_SL_5	1.30	0.85	7.0	42.0	1.1	2.2	0.06	11
	*CF00-01	1.29	15.90	2.40	31.36	0.75	2.16	0.11	23.86
	Avg Caliche	1.29	8.38	4.70	36.68	0.93	2.18	0.08	17.43

Table 4 *(cont.)*

	Element	Tl	Ni	Cu	Zn	Ga	As	Be	Ge
	Instrument	FUS-MS	FUS-MS	FUS-MS	FUS-MS	FUS-MS	INAA	FUS-ICP	FUS-MS
	Detection Limit	5.00	20	10	30	1	0.5	1	0.5
Grus	0119SL_13	0.48	†	†	40	21	†	3	0.9
Weathering profile	0119SL_0	0.70	†	†	†	19	†	3	0.8
	0119SL_1	0.59	†	†	40	22	-	3	0.9
	0119SL_2	0.57	†	†	40	21	-	3	0.7
	0119SL_3	0.58	†	†	40	22	0.8	3	0.9
	0119SL_4	0.39	†	†	45	21	-	3	0.7
	0119SL_5	0.49	†	†	50	23	-	3	0.9
	0119SL_6	0.50	†	†	30	19	-	2	0.7
	0119SL_7	0.42	†	†	60	2.0	†	3	†
Bedrock	19_SL_2	0.51	†	†	50	20	†	3	0.7
	*ST09-02	1.95	0.86	2.20	10.64	16.68	-	2.46	-
	*CF00-18	1.82	0.79	1.79	12.30	16.44	-	2.74	-
	Avg Bedrock	1.26	7.21	4.66	24.32	17.71	-	2.73	-
Caliche	19_SL_5	0.27	20	-	-	6.0	5.0	1	-
	*CF00-01	0.90	12.58	8.53	13.85	2.99	-	0.37	-
	Avg Caliche	0.45	16.29	8.53	13.85	4.49	5.00	0.68	-

Table 4 *(cont.)*

	Element	W	La	Ce	Pr	Nd	Pm	Sm	Eu
	Instrument	FUS-MS	FUS-MS	FUS-MS	FUS-MS	FUS-MS	-	FUS-MS	FUS-MS
	Detection Limit	0.5	0.05	0.05	0.01	0.05	-	0.01	0.005
Grus	0119SL_13	1.3	30.5	58.9	6.75	23.9	-	3.76	0.84
Weathering profile	0119SL_0	2.1	25.1	46.7	5.43	19.6	-	3.13	0.85
	0119SL_1	1.7	30.9	55.3	5.86	19.8	-	2.93	0.67
	0119SL_2	3.7	27.4	50.3	5.73	18.8	-	2.96	0.75
	0119SL_3	5.6	24.8	46.7	4.97	17.7	-	2.65	0.69
	0119SL_4	2.1	20.8	40.0	4.35	15.1	-	2.52	0.63
	0119SL_5	0.9	25.0	45.6	4.87	16.8	-	2.58	0.67
	0119SL_6	1.1	16.8	34.1	3.78	14.2	-	2.37	0.69
	0119SL_7	0.9	28.1	53.3	5.44	18.7	-	2.79	0.60
Bedrock	19_SL_2	†	25.6	48.9	4.96	17.2	-	2.63	0.62
	*ST09-02	1.95	32.13	42.92	7.16	24.68	-	3.68	0.77
	*CF00-18	0.07	18.25	20.02	3.96	13.92	-	2.36	0.61
	Avg Bedrock	0.84	25.33	37.28	5.36	18.60	-	2.89	0.67
Caliche	19_SL_5	3.6	21.40	12.9	4.49	17.8	-	3.05	0.65
	*CF00-01	0.24	9.58	20.90	2.47	9.24	-	1.52	0.32
	Avg Caliche	1.92	15.49	16.90	3.48	13.52	-	2.28	0.48

Table 4 *(cont.)*

	Element	Gd	Tb	Dy	Ho	Er	Tm	Yb	Lu	Sum REE
	Instrument	FUS-MS	FUS-MS	FUS-MS	FUS-MS	FUS-MS	FUS-MS	FUS-MS	FUS-MS	
	Detection Limit	0.01	0.01	0.01	0.01	0.01	0.005	0.01	0.002	
Grus	0119SL_13	2.64	0.39	2.05	0.36	0.97	0.14	0.94	0.140	132.28
Weathering profile	0119SL_0	1.99	0.27	1.39	0.25	0.66	0.09	0.48	0.069	106.01
	0119SL_1	1.89	0.24	1.28	0.22	0.59	0.09	0.58	0.086	120.43
	0119SL_2	1.85	0.24	1.16	0.21	0.61	0.08	0.45	0.064	110.61
	0119SL_3	1.66	0.22	1.05	0.19	0.52	0.07	0.44	0.061	101.73
	0119SL_4	1.60	0.20	0.94	0.18	0.48	0.07	0.42	0.070	87.240
	0119SL_5	1.77	0.19	0.98	0.18	0.48	0.06	0.40	0.062	99.650
	0119SL_6	1.54	0.18	0.88	0.16	0.46	0.06	0.40	0.059	75.680
	0119SL_7	1.73	0.21	1.02	0.19	0.49	0.07	0.38	0.056	113.08
Bedrock	19_SL_2	1.73	0.22	1.08	0.20	0.56	0.08	0.52	0.087	104.39
	*ST09-02	2.33	0.28	1.37	0.25	0.64	0.09	0.57	0.09	116.97
	*CF00-18	1.66	0.22	1.10	0.21	0.56	0.08	0.56	0.09	63.610
	Avg Bedrock	1.91	0.24	1.19	0.22	0.59	0.09	0.55	0.09	94.990
Caliche	19_SL_5	2.29	0.29	1.43	0.25	0.68	0.08	0.50	0.080	65.890
	*CF00-01	1.02	0.13	0.61	0.11	0.28	0.04	0.24	0.03	46.480
	Avg Caliche	1.65	0.21	1.02	0.18	0.48	0.06	0.37	0.05	56.180

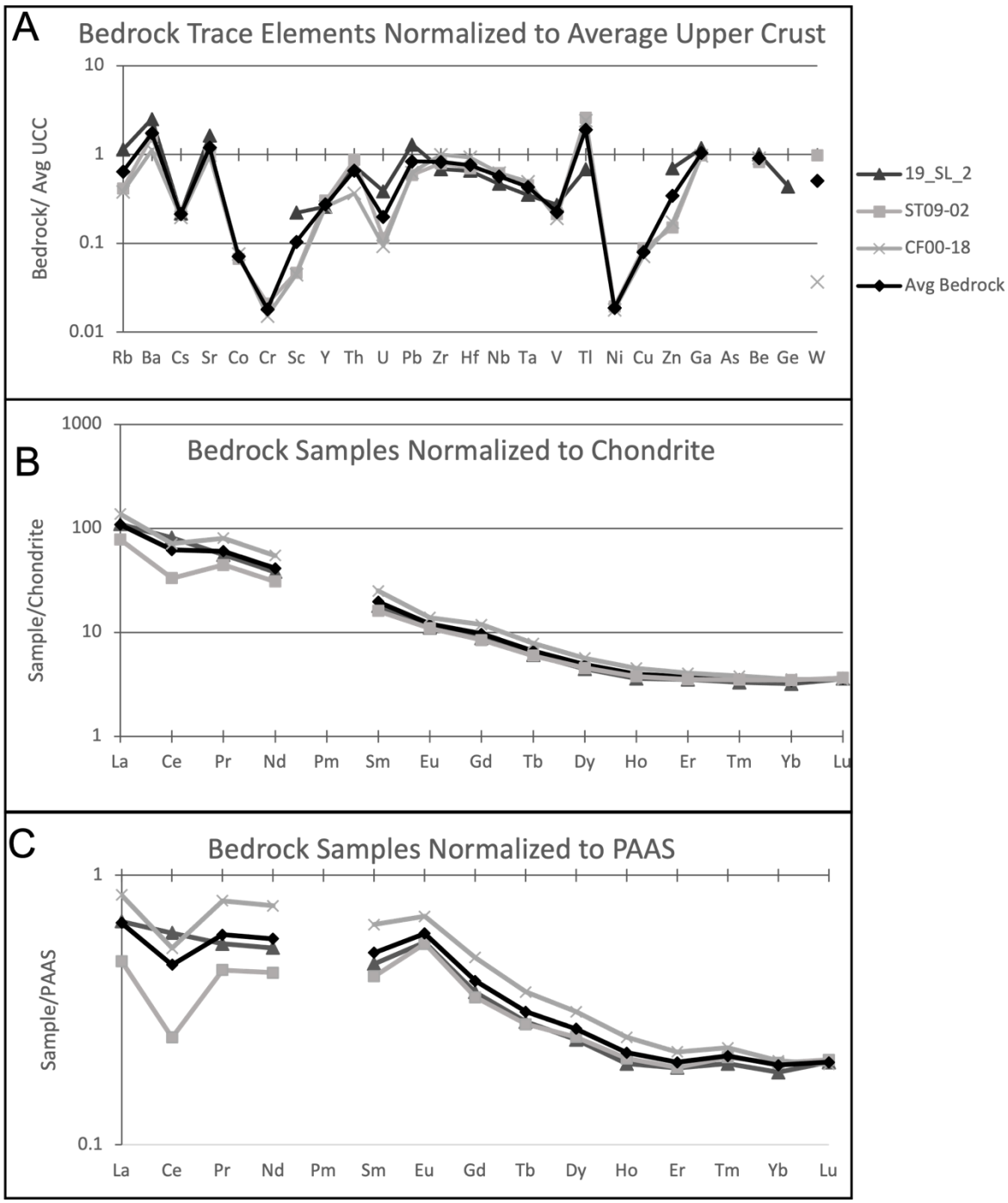


Figure 9. Trace element and rare earth element plots for unweathered Stepladder pluton. ST09-02 and CF00-18 are data from Modi (2011). (A) Trace elements normalized to McLennan (2001). (B) REEs normalized to chondrite for each bedrock sample. Chondrite values from Anders and Grevesse (1989). (C) Bedrock samples normalized to average Post-Archean Australian Average Shale (PAAS; McLennan, 1989).

Figure 9C depicts Stepladder pluton composition values normalized to Post-Archean Australian Shale (PAAS), a proxy for continental crust (Taylor and McLennan, 1985). Shale is a common normalizing factor in provenance studies because it shows fine structure in REEs that would otherwise not be observable. The overall fractionation relative to PAAS was negative (La/Lu = 3.29), but there was a slight negative to horizontal slope for the LREEs (La/Sm = 1.29) when compared to PAAS. HREEs showed a negative slope (Gd/Lu = 2.00; Fig. 9C). Data showed a negative Ce anomaly relative to PAAS with noticeable separation between sample concentration (Ce/ Ce* = 0.86; Fig. 9C). A positive PAAS-normalized Eu anomaly (Eu/Eu* = 1.33) occurred in all samples (Fig. 9C).

SECTION 6. CHARACTERIZATION OF THE STEPLADDER WEATHERING PROFILE AND GRUS

The Stepladder weathering profile through saprolite provides critical data that connect bedrock minerology and geochemistry to previously analyzed sediment. Given the expectation for limited weathering, as supported by low CIA values across all sediment grain sizes (Modi, 2011; Driscoll, 2016), saprolite was not considered as the potential source of compositional mismatches between sediment and source rock. Lacking a complete explanation for understanding the sediment geochemistry and detailed detrital zircon ages (Bonich-Wissink, 2017), it has become clear that a study of the chemical alteration of the weathering profile was necessary. Following the model set in place by Johnsson (1993), chemical weathering processes combined with mechanical weathering should precede transport.

6.1 Petrology

6.1.1 Textural Analysis

Figure 10 shows the outcrop where samples were collected for this study and images of each saprolite sample from the weathering profile. Visually, there was more iron oxidation in the samples near the top of the profile, which was noted from the increased orange coloring, in the top 40 cm of the profile (Fig. 10B – E). Fracture density data from the profile (Figs. 4, 10, 11) identified two fields: (1) from the top to ~ 40 cm depth where fracture density was high (8 – 10% of the area), and (2) below ~ 70 cm where fracture density was lower (0 – <6% of the area; Fig. 11). The connection between iron oxidation, clay accumulation, and fracture density should correspond an increase in CIA and mobility of TE and REE.

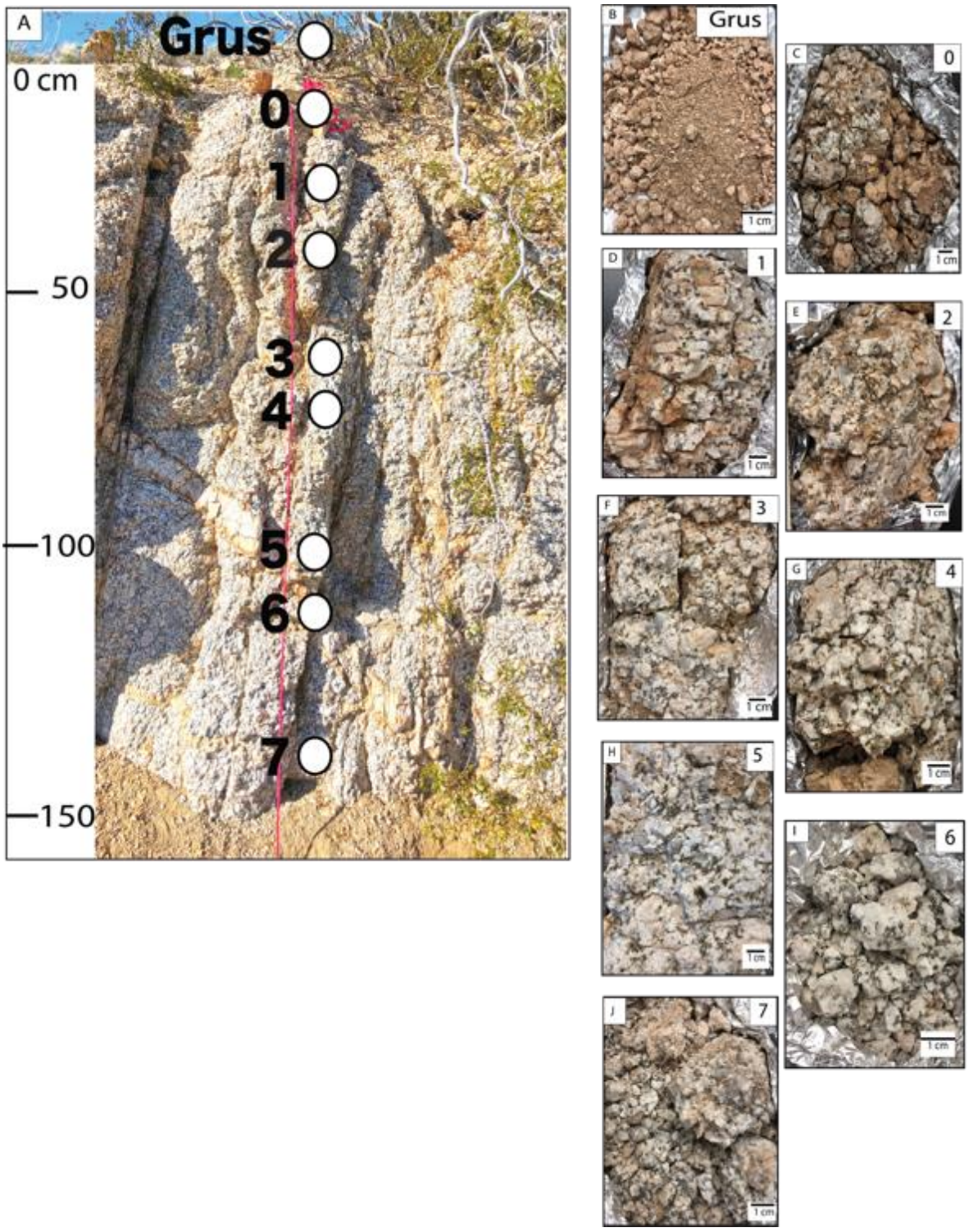


Figure 10. Samples collected from the Stepladder weathering profile. (A) Weathering profile with sample localities marked, 0 – 7 and corresponding to C – J. (B) Grus collected from the top of the weathering profile (sample 0119SL_13). (C) Sample 0119SL_0. (D) Sample 0119SL_1. (E) Sample 0119SL_2. (F) Sample 0119SL_3. (G) Sample 0119SL_4. (H) Sample 0119SL_5. (I) Sample 0119SL_6. (J) Sample 0119SL_7. Larger images of each sample can be found in Appendix A.

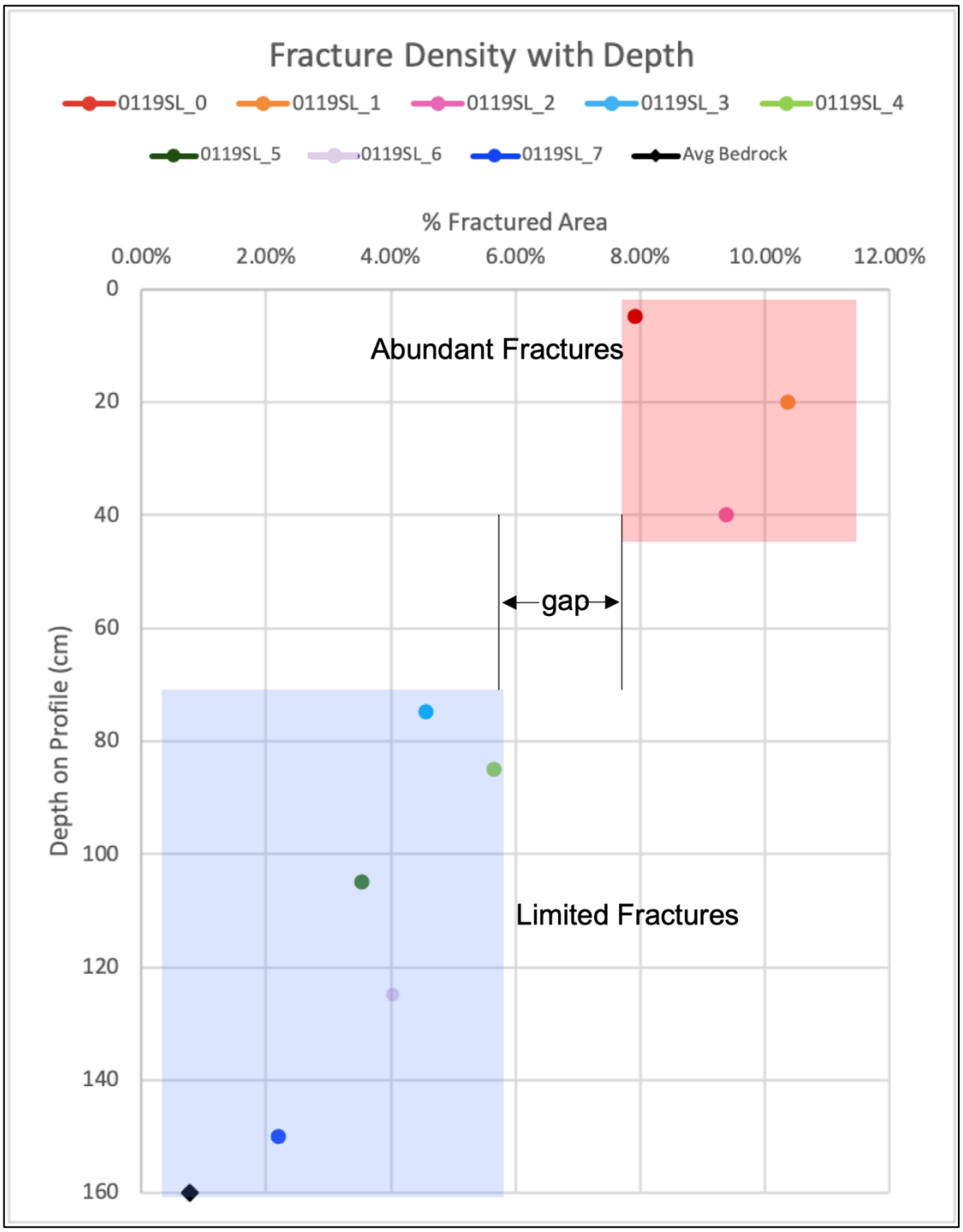


Figure 11. Percent fracture area vs. depth along the weathering profile. The red box denotes samples that had a high fracture density (> ~8 %) and individual samples are marked in warm colors. The blue box denotes samples with a low fracture density (< 6 %) and are shown with cool colors. Sample 19_SL_2 (average bedrock) is marked in black for comparison.

6.1.2 Mineralogy

Mineralogy of the saprolite weathering profile included plagioclase, quartz, potassium feldspar, and biotite as modal phases, with magnetite, apatite, zircon, titanite, hematite, and epidote as accessory phases. Figure 12 shows examples of the main phases and some accessory phases. Increased clay content on surfaces of plagioclase and K-felspar were observed throughout the profile compared to bedrock, with an increased accumulation of clay towards the top (Fig. 12C). Plagioclase was the most abundant mineral phase in the Stepladder pluton, and was the most common phase in the weathering profile. Samples throughout the weathering profile had plagioclase grains with oscillatory zoning (Fig. 12D, E) and Carlsbad twinning (Fig. 12E). Plagioclase grains also exhibited the most clay alteration in the weathering profile, including clay accumulation along twin planes, cleavage planes, zones, fractures, and patches coating the surface (Fig 12C, D). The K-feldspar in the Stepladder pluton and weathering profile existed as megacrysts (Fig. 5B) that showed perthitic texture (Fig. 12C). Clay alteration of K-feldspar also occurred along planes, fractures, and as patches (Fig. 12C, D). Biotite was located interstitially between main phases (Fig. 12A, C), but was also found as inclusions in other main phases (Fig. 12E). Biotite showed varying alteration throughout the weathering profile, including loss of pleochroism, loss of birds-eye extinction, and alteration to chlorite (Fig. 12D). Quartz in the saprolite samples exhibited no alteration relative to bedrock and undulatory extinction was seen in under polarized light. Minimal fractures were observed from quartz.

6.1.3 Evidence for Weathering

With plagioclase, there are no grains in sample 0 that have an alteration score of 1, whereas at the bottom of the profile, the frequency of 1 scores greatly increases (Fig. 13). Every

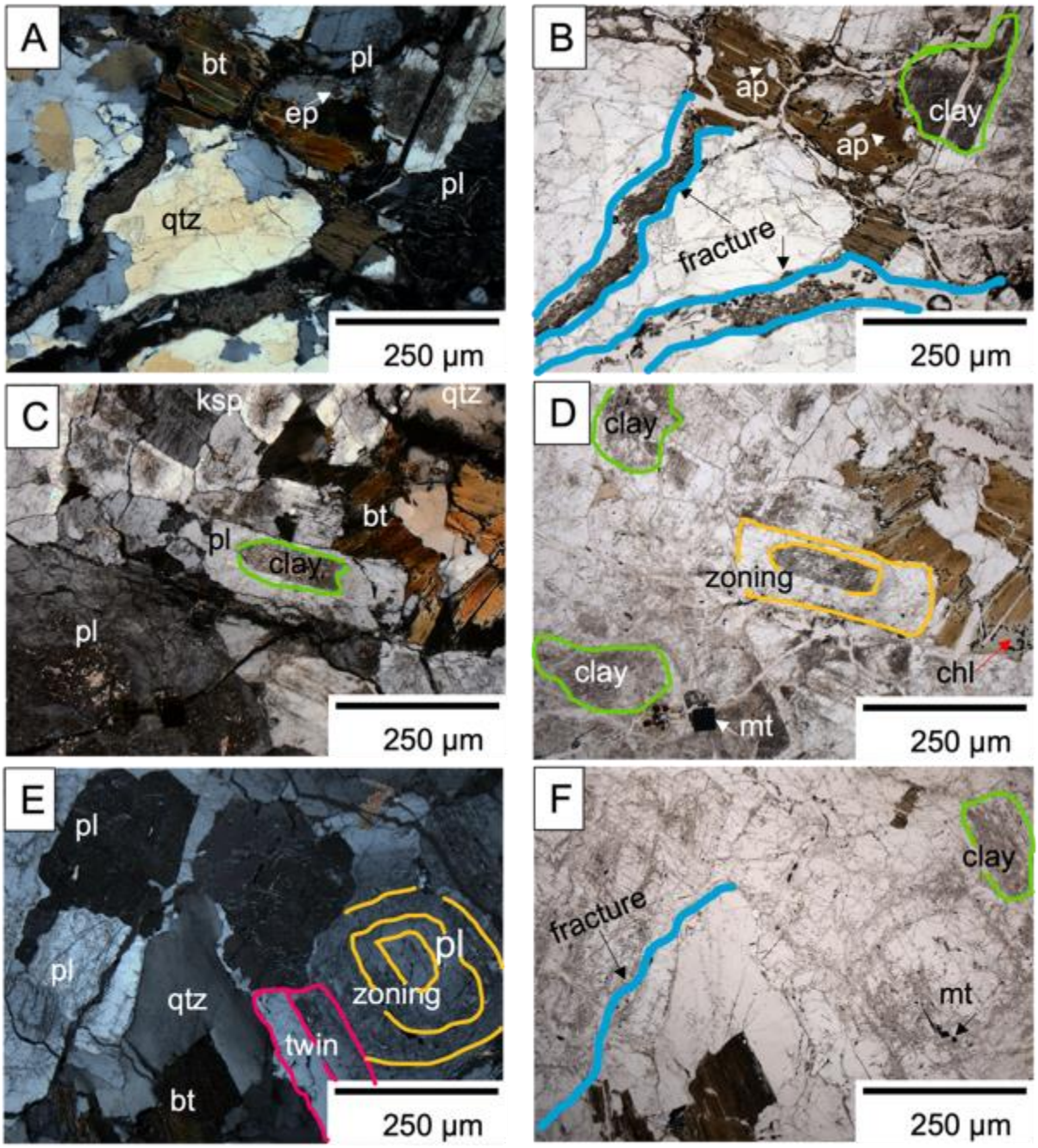


Figure 12. Photomicrographs of the main mineral phases from the Stepladder weathering profile samples. Bt = biotite, qtz= quartz, pl = plagioclase feldspar, ksp = potassium feldspar, mt =magnetite, ap = apatite, ep =epidote, chl= chlorite. Outlines in green denote clay, lines in blue denote fracturing, outlines in yellow denote zoning, and outlines in pink denote twins. (A) Sample 0119SL_0 (5 cm) in xpl. (B) Sample 0119SL_0 (5 cm) in ppl. (C) Sample 0119SL_3 (75 cm) in xpl (D) Sample 0119SL_3 (75 cm) in ppl. (E) Sample 0119SL_7 (140 cm) in xpl. (F) Sample 0119SL_7 (140 cm) in ppl.

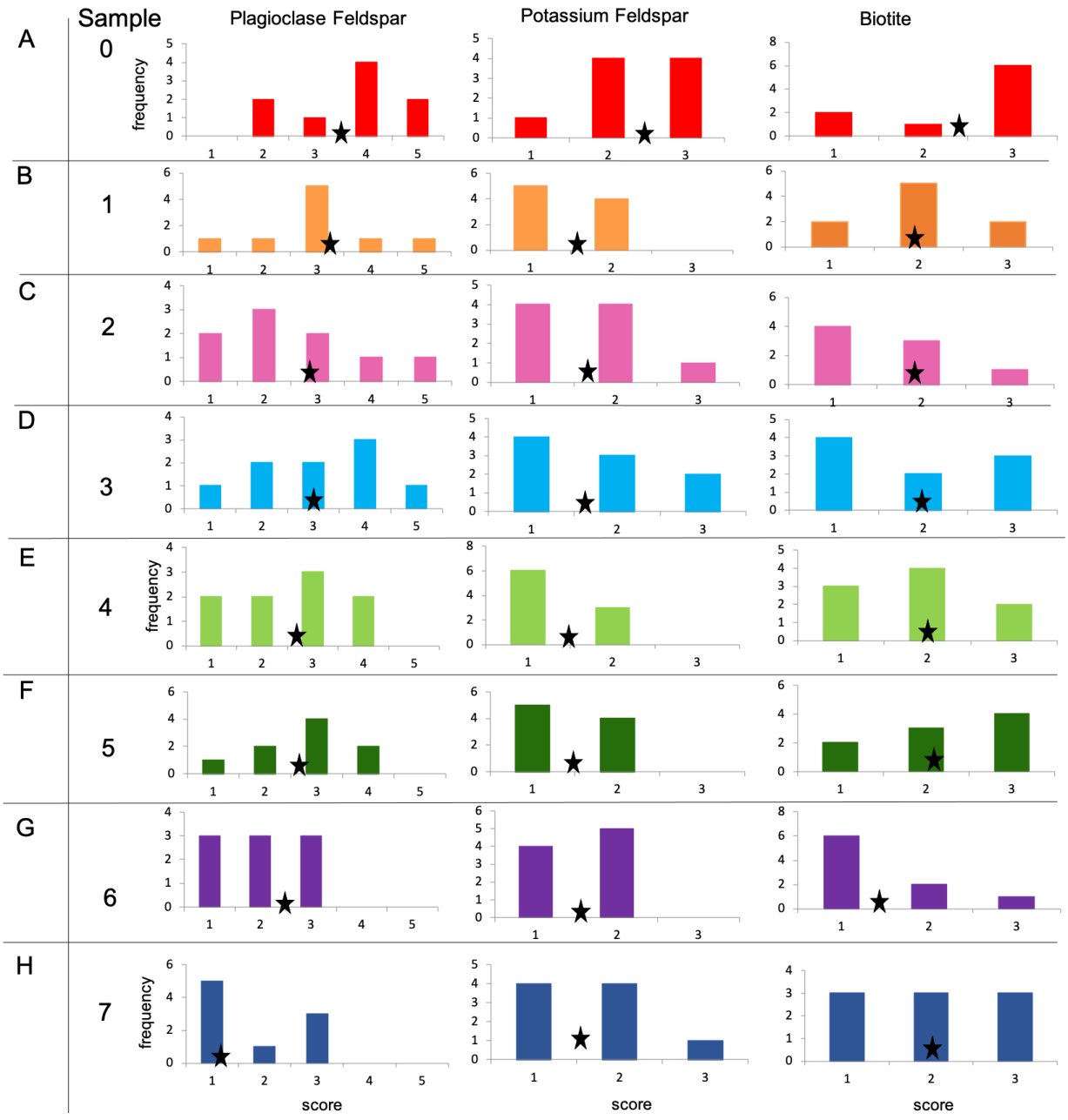


Figure 13. Distribution of scored for weathered mineral phases, plagioclase, K-feldspar, and biotite, respectively (in columns from left to right). Warm colors on the histogram represent samples with high fracture density and cool colors show low fracture density. Weathering intensity was scored on a scale of 1 to 5 for plagioclase feldspar, 1 to 3 for K-feldspar, and 1 to 3 for biotite. Black stars indicate average scores for each sample. (A) Sample 0 scores. (B) Sample 1 scores. (C) Sample 2 scores. (D) Sample 3 scores. (E) Sample 4 scores. (F) Sample 5 scores. (G) Sample 6 scores. (H) Sample 7 scores.

sample shows a 2 and 3 score for plagioclase (Fig. 13). Scoring of 4 is only seen in the upper 5 samples (5 - 105 cm) with a high frequency in sample 0 (Fig. 13A-F). A score of 5 (Table 2), is seen in the top 75 cm of the profile (Fig. 13A-D), which seems to correlate to the fracture density and clay accumulation data seen in Figures 9 and 10.

Potassium feldspar follows a similar trend to plagioclase. Data show great abundance of 1 scores (unweathered) towards the bottom of the profile, a common frequency of 2 scores throughout, and 3 scores are mostly at the top, with an isolated 3 score in sample 7 (Fig. 13). The results for potassium feldspar also match with Figures 9 and 10, showing increased weathering at the top due to increased fracture density.

Biotite has no systematic trend like plagioclase and potassium feldspar. Scores vary from 1 to 3 per sample, but most have an average score of ~2. The alteration seen (conversion to chlorite, loss of pleochroism, lowering of interference colors, and loss of birds-eye extinction) and is likely due to hydrothermal fluids during past extensional events (Banfield and Eggleton, 1988).

6.2 Geochemistry

6.2.1 Major Elements

The oxide weight percentages for major elements were plotted against depth for the weathering profile (e.g., Little and Aeolus Lee, 2006; Gong et al., 2011; Peng et al., 2014; Fig. 14). For most samples and the oxide percentages, values did not vary outside of standard deviations, which meant the oxides were not enriched or depleted compared to the average bedrock composition. However, most oxides measured from grus had different percentages compared to other samples and bedrock, with SiO_2 and Na_2O depletions and FeO, MgO, and

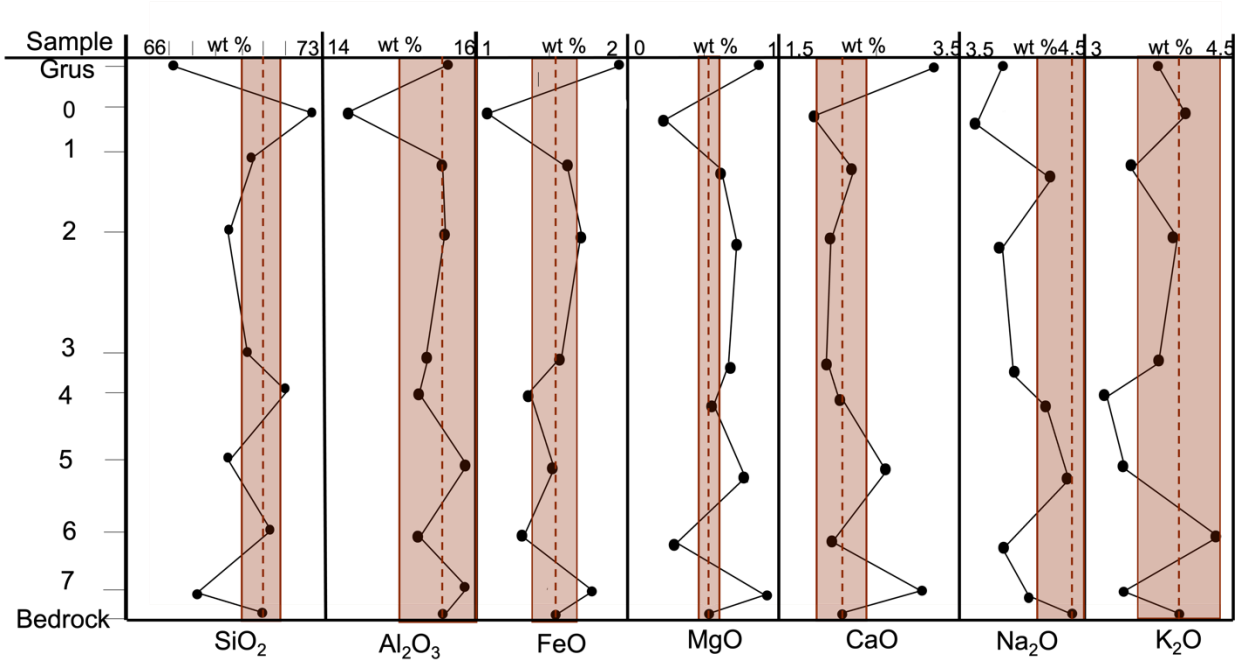


Figure 14. Major oxide weight percent (wt%) vs. depth for samples collected from the saprolite weathering profile. The red dashed lines indicate the average bedrock composition. The red shaded boxes represent one standard deviation from the average bedrock composition.

CaO enrichments. Sample 0 (5 cm) had depleted Al_2O_3, but percentages did not vary for the other samples. FeO (calculated from Fe_2O_3) was depleted in sample 0, which was unexpected given the visual appearance (oxidation) (Fig. 10C). Enrichments in MgO for samples 1, 2, 3, 5, 7 could be explained by higher proportions of biotite, although proportions of mineral phases were not quantified from the samples. Depletions for Na_2O in samples 2, 3, 6, 7 could be due to conversion of plagioclase to kaolinite. Similarly, K_2O doesn't appear to show anomalous behavior, and the few depletions seen in the lower samples could be due to a decreased concentration of potassium feldspar in those samples. Depletions in MgO and Na_2O for sample 6 could have been caused by mobile element accumulation at depth (Nesbitt and Markovics, 1997).

The CIA values for the Stepladder weathering profile range from 53.5 – 56.5 (Fig. 15A) and were indicative of mineral chemical weathering. However, in A-CN-K space (Fig. 15A and 15B) and A-CNK-FM space (Fig. 15C and 15D), which accounts for mafic components (Nesbitt & Young, 1989), the samples clustered near the fresh bedrock and there were no systematic CIA changes for the profile, regardless of evidence for hydrolysis petrographically. Increased chemical weathering effects would result in samples plotting farther from a source and scatter around the predicated weathering pathway indicated variability in source rock composition.

6.2.2 Trace Elements

Overall, weathering profile samples were depleted against bedrock, sediment, and grus, but most closely matched TE concentrations from grus (Fig. 16A – C). Figure 16A is an average Stepladder pluton normalized TE spider plot, showing Sc, U, and Pb concentration enrichments

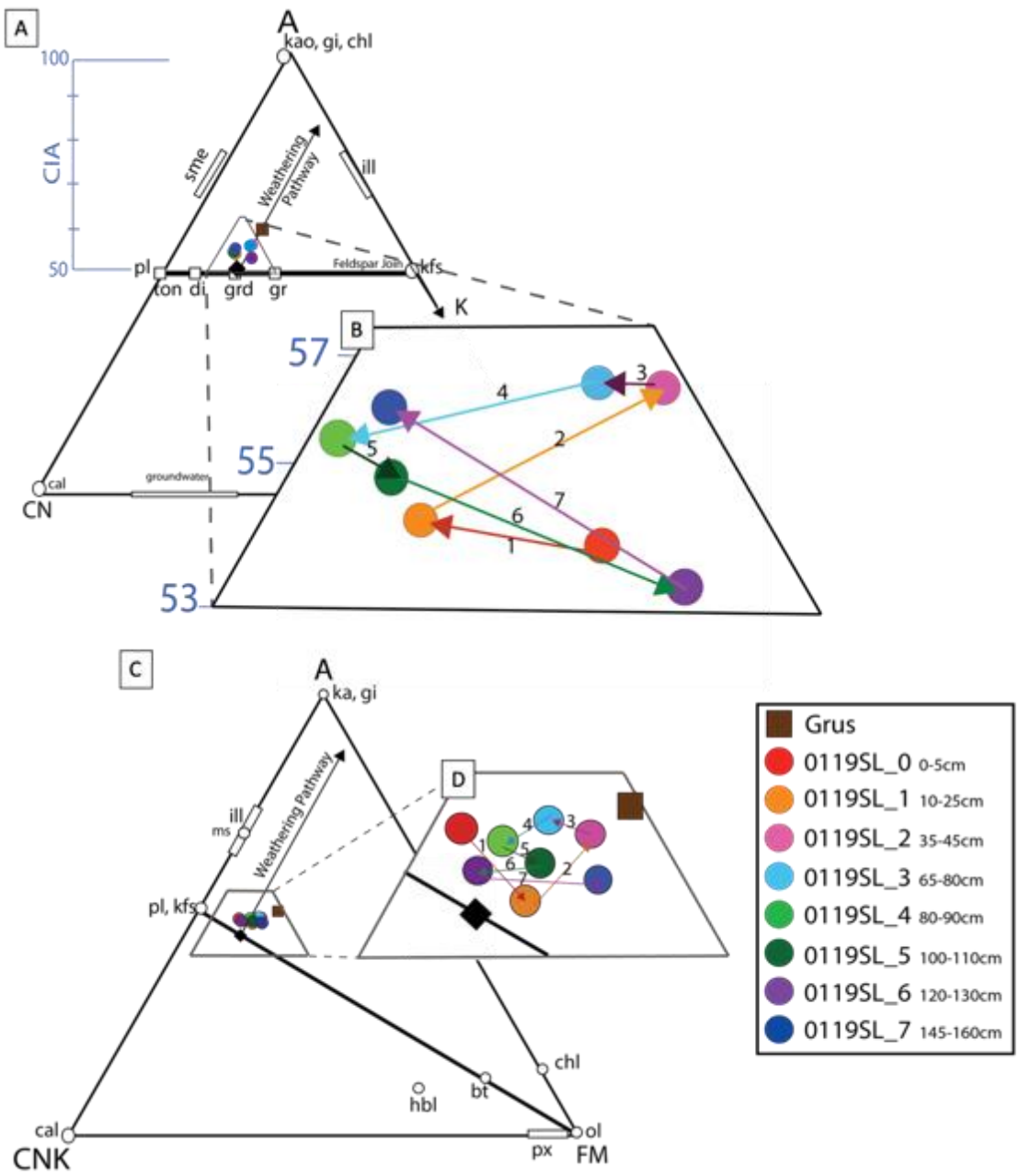


Figure 15. Plots modified from Nesbitt and Young (1984, 1989) for the Stepladder pluton and saprolite weathering profile. (A) A-CN-K plot for Stepladder bedrock (black square), weathering profile, and grus. A= Al_2O_3, CN = CaO + Na_2O, K = K_2O, kao = kaolinite, gi = gibbsite, chl = chlorite, sme = smectite, ill = illite, pl = plagioclase, kfs = potassium feldspar, ton = tonalite, di = diorite, grd = granodiorite, gr = granite, bas = basalt, cal = calcite. (B) Transition from sample to sample based on their location in the weathering profile, marked by arrows. (C) A-CNK-FM plot for Stepladder bedrock (black square), weathering profile, and grus. (D) Arrows indicate order from top of the profile (1) to bottom of the profile (7) A= Al_2O_3, CNK = CaO + Na_2O + K_2O, FM = FeO(t) + MgO, kao = kaolinite, gi = gibbsite, chl = chlorite, sme = smectite, ill = illite, ms = muscovite, pl = plagioclase, kfs = potassium feldspar, cal = calcite, hbl = hornblende, bt = biotite, px = pyroxene, ol = olivine.

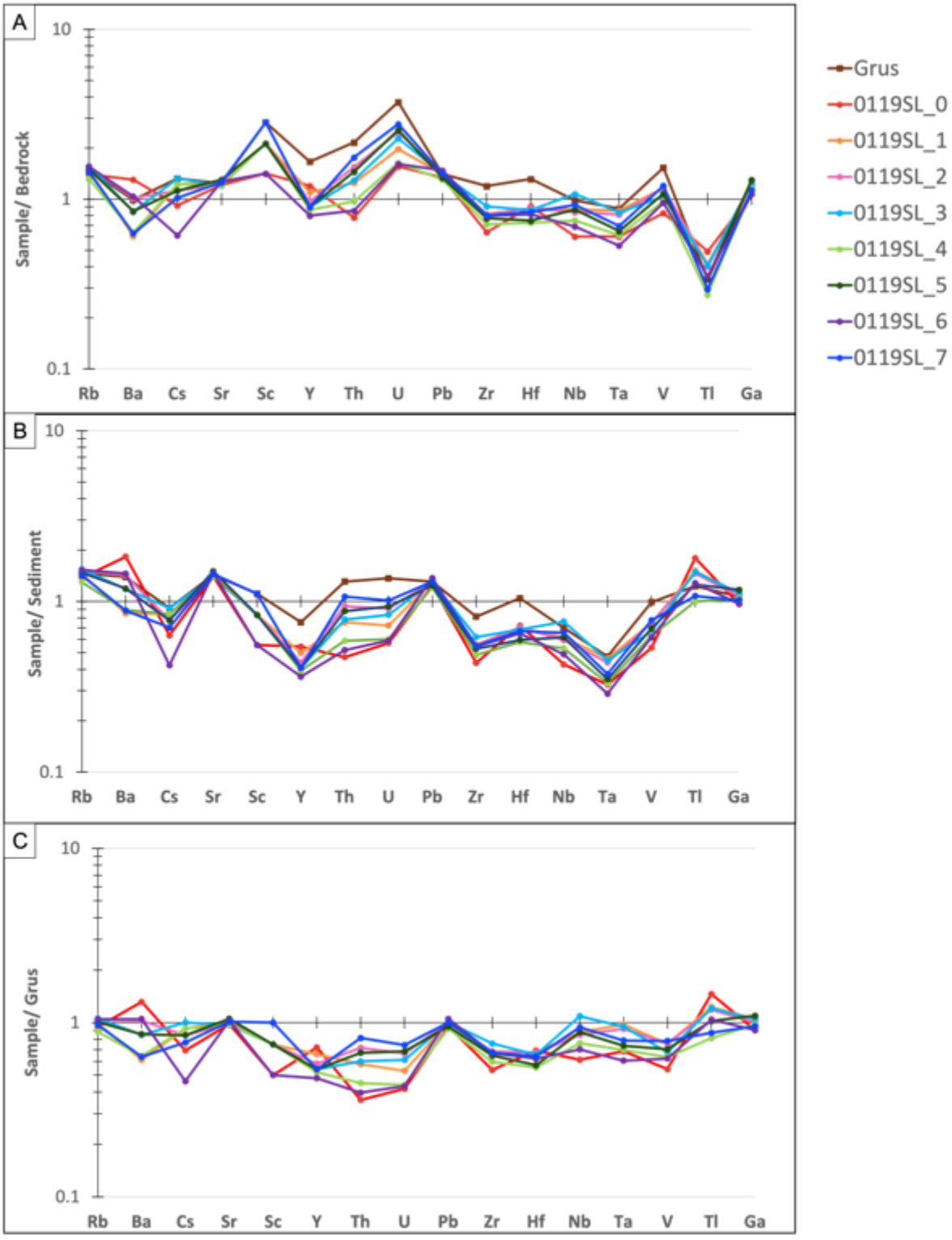


Figure 16. Trace element spider plots for stepladder weathering profile. (A) Weathering profile samples normalized to bedrock. (B) Weathering profile normalized to the average Stepladder sediment composition from Modi (2011) and Driscoll (2016). (C) The Stepladder weathering profile normalized to grus. Not shown are Co, Cr, Ni, Cu, and As because their concentrations were below detection limits.

and Zr, Hf, Ta and Tl depletions for the profile samples relative to bedrock. Some immobile elements (Zr and Hf) were depleted relative to bedrock, but their lower concentrations are likely not due to chemical weathering because of differential distribution of zircon, which is resistant to chemical weathering (Tole, 1985), in the weathering profile compared to the bedrock samples.

The TE concentrations were also normalized to average sediment data from Modi (2011) and Driscoll (2016) (Fig. 16B). Depletions, relative to an average sediment composition, were noted for Cs, Y, Zr, and Ta, and Rb, Ba, Sr, and Tl enrichments results. Grus TE compositions were more like sediment, with the exception of Ta. Lastly, weathering profile samples were normalized to grus (Fig. 16C). Minor depletions in Y, Th, U, Zr, and Hf were identified, compared to slight enrichments in Ba and Tl (Fig. 16C).

Bedrock normalized TE with depth varied for high field strength elements (HFSE), large ion lithophile elements (LILE), transition metals, and U/Th/Pb (Fig. 17). Most HFSEs showed depletions relative to bedrock, except for Y, which was depleted in the bottom 40 cm and enriched at the top of the profile (Fig. 17A). Nesbitt and Markovics (1997) show Y enrichments during weathering, which should correspond to higher fracture density and clay accumulation, which was identified from the top 40 cm of the profile (Figs. 4 and 11). Trace-element group LILE showed scatter versus depth and no strong depletions or enrichments relative to bedrock (Fig. 17B). For these mobile elements (Rb, Sr, and Ba), there likely has not been enough time to weather and move them in the profile (Cramer & Nesbitt, 1983; Middelburg et al., 1988).

For transition metals, for which this study analyzed V and Zn, there was almost no concentration variation from bedrock, although Zn concentrations increased with depth into the profile (Fig. 17C). The concentrations of U, Th, Pb (Fig. 17D) from the weathering profile

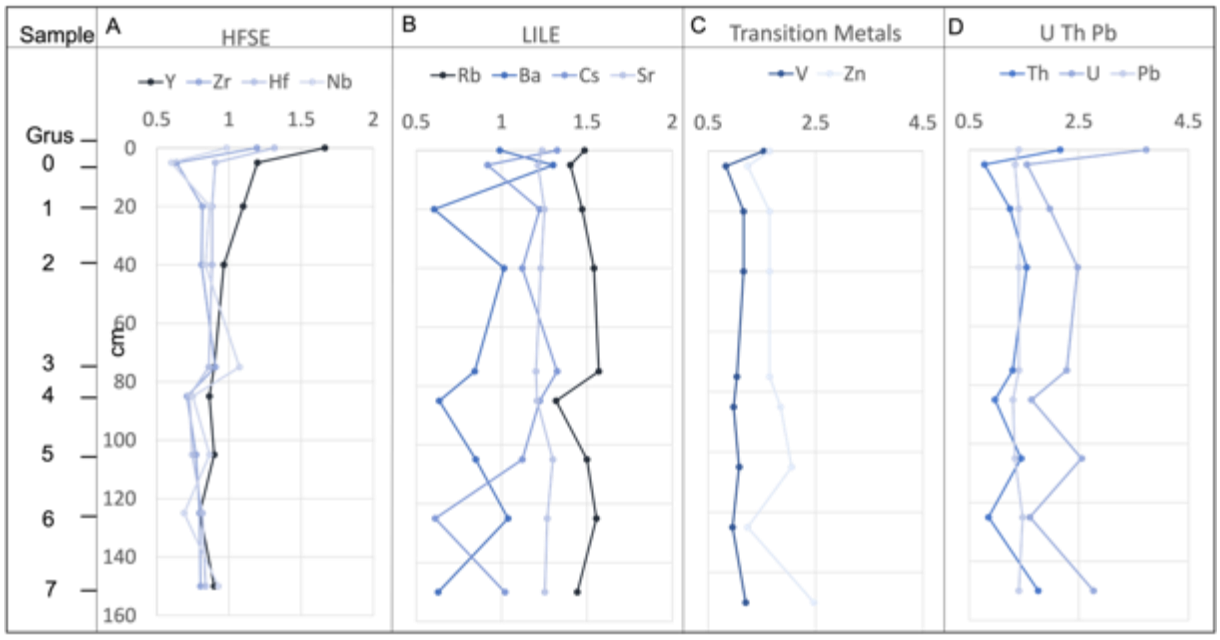


Figure 17. Bedrock-normalized trace elements vs depth (cm) for (A) high field strength elements (HFSE), Y = yttrium, Zr = zircon, Hf = hafnium, Nb = niobium. (B) large ion lithophiles elements (LILE), Rb = rubidium, Ba = barium, Cs = cesium, Sr = strontium. (C) transition metals, V = vanadium, Zn = zinc. (D) and U (uranium) Th (thorium) Pb (lead).

varied, with U and Th being enriched throughout the profile and grus, but Pb being more similar to the bedrock, likely because it is immobile.

6.2.3 Rare Earth Elements

The REE concentrations for the weathering profile (Table 4) were normalized to average Stepladder pluton bedrock, as well as average shale. The total REE concentrations for the weathering profile were like the bedrock total concentrations, although sample 6 had slightly lower total REE concentrations than bedrock (Table 4). The HREEs had slightly greater concentrations (2.01 ppm to 2.83 ppm) compared to the Stepladder pluton (2.00 ppm; Appendix B9), but the HREE slope ($Gd_{BN}/Lu_{BN} = 1.24$) is negative (Fig. 18A).

An Eu anomaly (Eu/Eu^*_{BN}; McLennan, 1989) was calculated relative to bedrock by using the following equation (Equation 6):

$$Eu^*_{BN} = (Sm_{BN} * Gd_{BN})^{1/2} \quad \text{Eq. 6}$$

All but two samples showed a positive anomaly ($Eu/Eu^*_{BN} > 1$) relative to bedrock (Fig. 16B). The two samples (1 and 7) that did not, had $Eu/Eu^*_{BN} = 0.99$ and 0.96, respectively (Appendix B9), indicating Eu concentrations like bedrock. When normalized to PAAS, the data showed a negative overall slope (Fig. 18B), which was expected because shale has higher HREE concentrations due to the presence of zircon in fine-grained sediment (Condie, 1991). A positive Eu anomaly can also result from Eu in plagioclase (Fig. 18B), which would not be in shale.

A Ce anomaly (Ce/Ce^*_{BN}); Lawrence and Kamber, 2006) was also calculated to show anomalous behavior relative to bedrock (Equation 7):

$$Ce^*_{BN} = (2*Pr_{BN} — Nd_{BN}) \quad \text{Eq. 7}$$

All weathering profile samples had a positive Ce anomaly ($Ce/Ce^*_{BN} > 1$) compared to bedrock. Cerium does not require a significant amount of chemical weathering to become mobile.

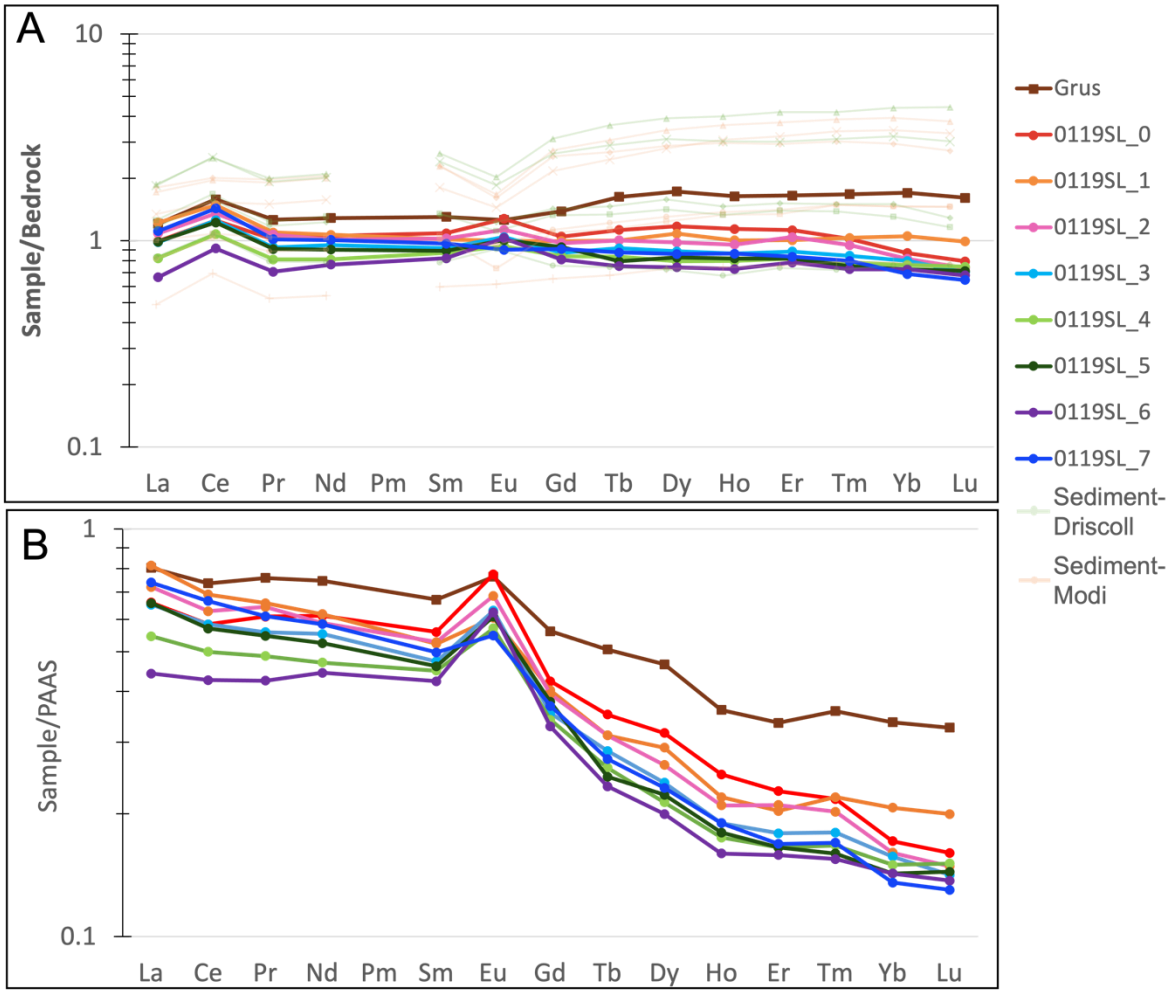


Figure 18. (A) Weathering profile rare-earth elements normalized to average bedrock. Transparent lines represent stepladder sediment from Modi (2011) and Driscoll (2016). (B) Weathering profile REEs normalized to Post-Archean Australian Shale (PAAS; McLennan, 1989).

Therefore, a positive bedrock-normalized Ce anomaly would reflect the oxidation of Ce^{3+} to Ce^{4+} (Braun and Pagel, 1994), which is insoluble.

6.3 Grus

Grus is a non-transported product produced by chemical weathering and disintegration of saprolite and directly mantles a bedrock weathering profile (Bates and Jackson, 1987). Grus was compared to transported sediment. Chemical weathering and the process of grusification may be compositionally distinguishing the bedrock from the weathering profile and resulting sediment.

6.3.1 Major Elements

The elemental composition of grus most closely matched sediment data from Modi (2011) and Driscoll (2016). In Figure 14, with the exception of SiO_2, the oxide weight percentages for grus differed from values in the weathering profile and bedrock. The major elemental compositions of grus appears to be the compositional bridge between the weathering profile and sediment. In A-CN-K and A-CNK-FM space, the grus sample was a more intensely weathered (Fig. 15), with a CIA of 60.

6.3.2 Trace Elements

Bedrock-normalized TE data for grus differed from the weathering profile, with higher Y, Zr, Hf, Nv, Cs, V, Zn, U, and Pb concentrations (Fig. 17). The grus TE composition more closely matched the weathering profile compositions compared to sediment (Fig. 16). However, the grus normalized TE plot showed similar depletions and enrichments compared to sediment, except concentrations were lower.

6.3.3 Rare Earth Elements

The grus REE concentrations were higher than from bedrock (Fig 18A). Grus most closely matched, in concentration ranges and REE spider plot shape, sediment (La/Lu = 1.28; Fig. 18A). The LREEs had a positive bedrock-normalized slope (La/Sm = 0.92), as did the HREEs (Gd/Lu = 0.86). A positive bedrock-normalized Ce anomaly is present (Ce/Ce*= 1.28), similar to the weathering profile (Fig. 18A). Contrary to the weathering profile, grus had a negative Eu anomaly (Eu/Eu* = 0.93) compared to sediment from Modi (2011) and Driscoll (2016). From the REE results (Fig. 18), as well as major and trace element results (Figs. 14 – 17), the grus composition was more similar to the transported sediment compositions from Modi (2011) and Driscoll (2016).

SECTION 7. PROVENANCE INDICATOR PLOTS

7.1 Compositional Homogeneity Within the Bedrock

Samples of the Stepladder pluton source rocks have been analyzed in several studies (Modi, 2011; Driscoll, 2016; Bonich-Wissink, 2017) and bedrock compositions have been similar, regardless of where samples came from on the pluton. These results indicate that the source is homogenous. Figure 19A shows the average Stepladder pluton bedrock normalized (ABN) plot that compares REEs versus Eu/Eu* for all bedrock composition values. Figure 19A, along with Appendix C7 and C8, show homogeneity in bedrock' compositions. Dissimilarities, then, must come from a different source or process during the creation of sediment.

7.2 Major Elements

7.2.1 A-CN-K and A-CNK-FM plots

To determine provenance from the A-CN-K plots, bulk sediment can be correlated back to a source by drawing a parallel line to the A-CN join through the sediment to the feldspar join (Fedo et al., 1995; Nesbitt and Markovics 1997). The compositions of the weathering profile samples identified the Stepladder pluton as the source (Fig. 15A). However, the sediment data from Modi (2011) and Driscoll (2016) identify a range of sources (Appendix C3), and depending on the grain size, identify granite, granodiorite, and diorite for samples that only came from a granodiorite (Appendix C3). Using A-CNK-FM plots to determine provenance by including a mafic component, the weathering profile sample data did not as identify the Stepladder granodiorite as its source; there was scattering at the FM apex (Fig. 15B).

Similarly, Modi (2011) created a Cr/V and Y/Ni mixing plot with basalt and granodiorite as end members (Fig. 20), and the plot identified a mafic end member as part of the source. Sediment data from Driscoll (2016) also identify a range of sources, and specifically the

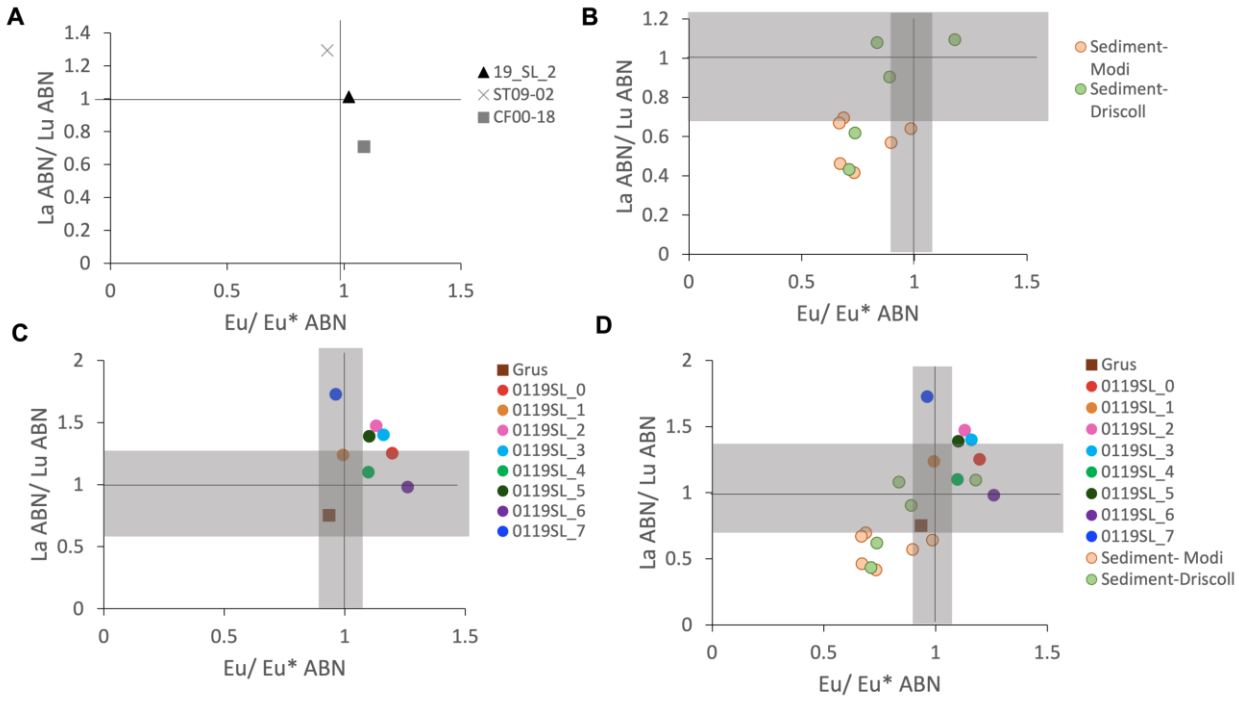


Figure 19. (A) Average bedrock normalized (ABN) total REEs vs. Eu/Eu * ABN for all bedrock samples used to create average bedrock. Data for ST09-02 and CF00-18 come from Modi (2011). The range in bedrock compositions was used to create grey boxes in all of the plots, which are effectively error bars within 0.05 of the average value. The grus and saprolite weathering profile samples are compositionally comparable to bedrock. (B) Total REEs ABN vs. Eu/Eu * ABN for sediment from Modi (2011) and Driscoll (2016). Pastel orange represents data from Modi (2011) and pastel green represents samples from Driscoll (2016). (C) Total REEs ABN vs. Eu/Eu * ABN results for the weathering profile samples and grus. (D) All samples plotted together.

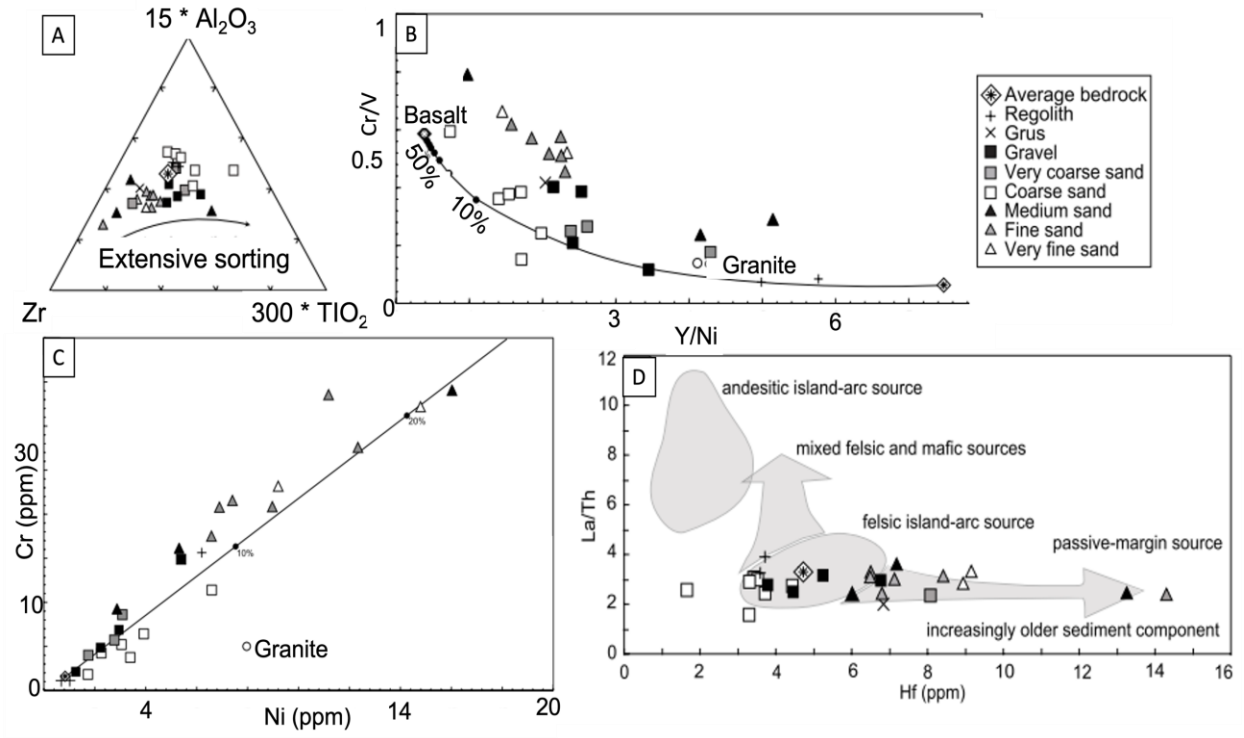


Figure 20. Figures from Modi (2011) indicating compositional variation in the sediment. (A) Zr – Al_2O_3 (x15) – TiO_2 (x300) ternary diagram from Garcia et al. (1994) showing sediment maturity. (B) Cr/V vs Y/Ni plot showing basaltic mixture present in sediment (McLennan et al., 1993) end members from Condie (1993). (C) Cr vs Ni plot also indicating multiple sources for the Stepladder sediment (Taylor and McLennan, 1985), end members from Condie (1993). (D) La/Th vs Hf plot to identify source of clastic sediment (Floyd and Leveridge, 1987).

fine-grained sediment that had been hydrodynamically sorted point to a more mafic source composition (Fig. 20B; Appendix C4). As such, these plots do not provide accurate provenance determinations and call into question the viability of this provenance plotting in cases where hydrodynamic sorting has occurred.

7.3 Trace Elements

7.3.1 Incompatible vs. Compatible Element Plots

It is also possible to compare incompatible versus compatible TE compositional data to link sediment to its bedrock source (Taylor and McLennan, 1985). Incompatible and compatible TE data provide details about source rock magma differentiation and do not change during chemical weathering. Some studies have used ratios of incompatible versus compatible concentrations to link sediment to source (e.g., McLennan et al., 1993; Vital et al., 1999; Do Campo and Guevara, 2005; Óladóttir et al., 2011; Liu et al., 2013), whereas other studies use La/Th vs. Hf data with other incompatible vs compatible TEs to identify a bedrock source for sediment (e.g., Bhatia and Taylor, 1981; Bhatia and Crook, 1986; Basto et al., 2019; Ramasamy et al., 2021). However, similar plots for the Stepladder weathering profile and sediment do not provide comparable results (Fig. 21). Specifically, the Th/Sc vs. Sc graph (Fig. 21A), the La/Th vs. Hf graph (Fig. 21B), the Th/Ta vs. Yb graph (Fig. 21C), or the SiO_2 to Zr (Fig. 21D), or Y (Fig. 21E), or Rb (Fig. 21F) graphs, all show that the weathering profile data do not match the sediment or bedrock compositions.

7.3.2 Discriminatory plots

Discrimination plots can also identify sediment sources (e.g., Bailey, 1981; Maniar and Piccoli, 1989; Pearce, 1996; Armstrong-Altrin, 2015; Laceby et al., 2015; Wang et al., 2018; Whalen and Hildebrand, 2019). Modi (2011) determined that the sorted Stepladder sediment was

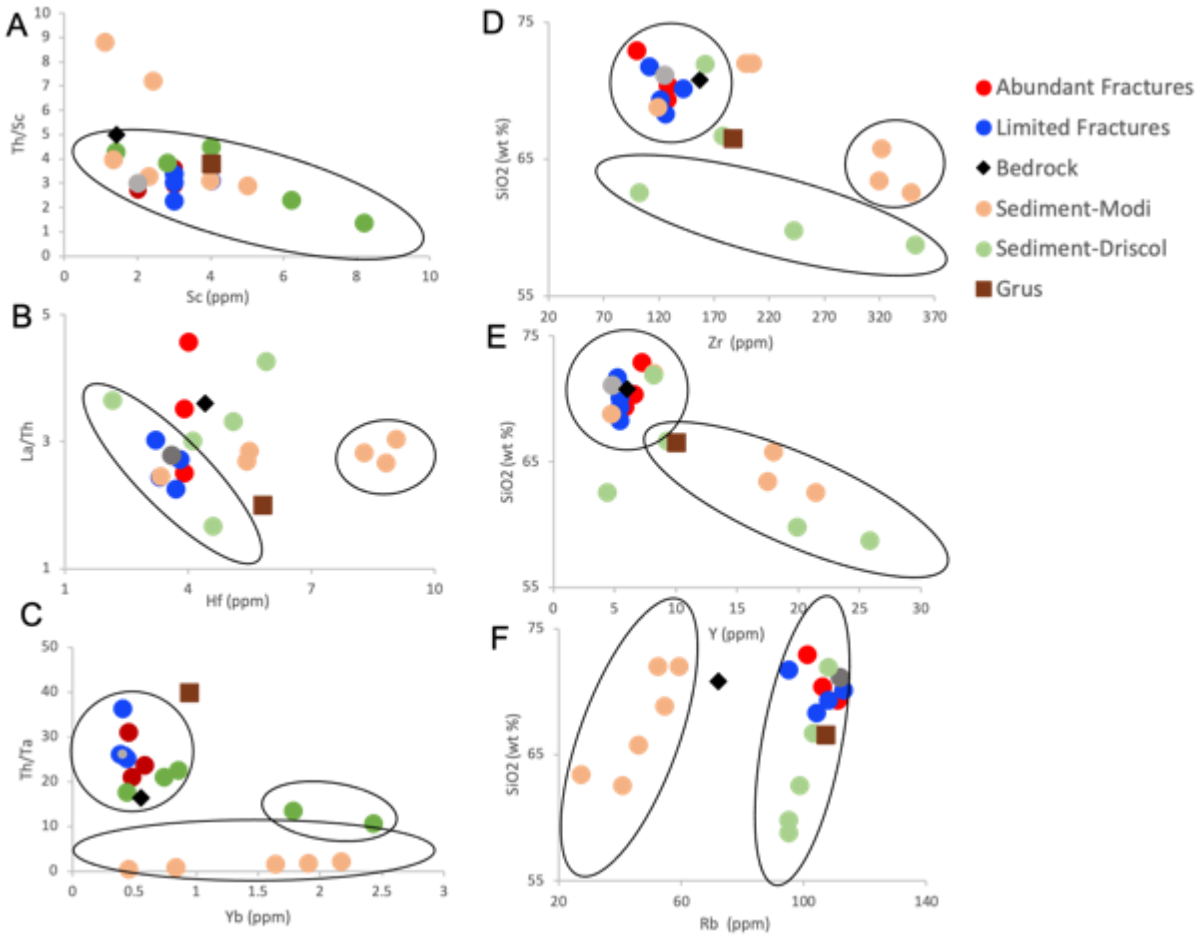


Figure 21. Ratios of incompatible and compatible trace element concentrations (in ppm). Black circles indicate groups of like patterns drawn around Stepladder pluton data, weathering profile data, and sediment data (Modi, 2011; Driscoll; 2016). (A). Th/Sc vs. Sc plot for sediment, weathering profile, grus, and bedrock. (B) La/Th vs. Hf. (C) Th/Ta vs. Yb. (D) Zr vs. SiO_2 wt% for bedrock, weathering profile, grus, and sediment. (E) Y vs. SiO_2 wt%. (F) Rb vs. SiO_2 wt%.

mature (Fig. 20A), although the plot does not provide much detail about the source, it does provide information about the sediment composition similarity, even if technically immature because of the presence of feldspars.

Another type of discrimination plot, described by Floyd and Leveridge (1987), uses the La/Th component to determine the source composition where high La/Th would indicate a mafic source, and low La/Th would reflect a felsic source. The Hf component also determines sediment recycling. Many other studies have generated a similar plot (e.g., Bhatia and Taylor, 1981; Bhatia and Crook, 1986; Basto et al., 2019; Ramasamy et al., 2021). However, the data from the weathering profile in this study and sediment data from Modi (2011) and Driscoll (2016) indicated different bedrock sources (Fig. 22), with the finer sediment being sourced from a passive margin and the bedrock, weathering profile and grus being sourced from "felsic island arcs" (Fig. 22). Differences in Stepladder sediment composition, particularly across different grain sizes, has been attributed to hydrodynamic sorting (Modi, 2011; Driscoll, 2016).

7.4 Rare Earth Elements

7.4.1 REE Normalized to Stepladder Bedrock

Bedrock-normalized REE plots are assumed to be the most accurate way to match sediment to bedrock source, especially in this case where the bedrock is known. However, the bedrock-normalized REE plot for the weathering profile does not accurately match the weathering profile, grus, or sediment to bedrock (Fig. 18A). Even more so, the weathering profile, which is thought to be the intermediary step between source and sediment, showed a different pattern to that of sediment (Fig. 18A). All components in this study are known and/or limited, so the inconsistency creates a problem in the way we identify provenance and caution must be taken when using these plots to identify an unknown source.

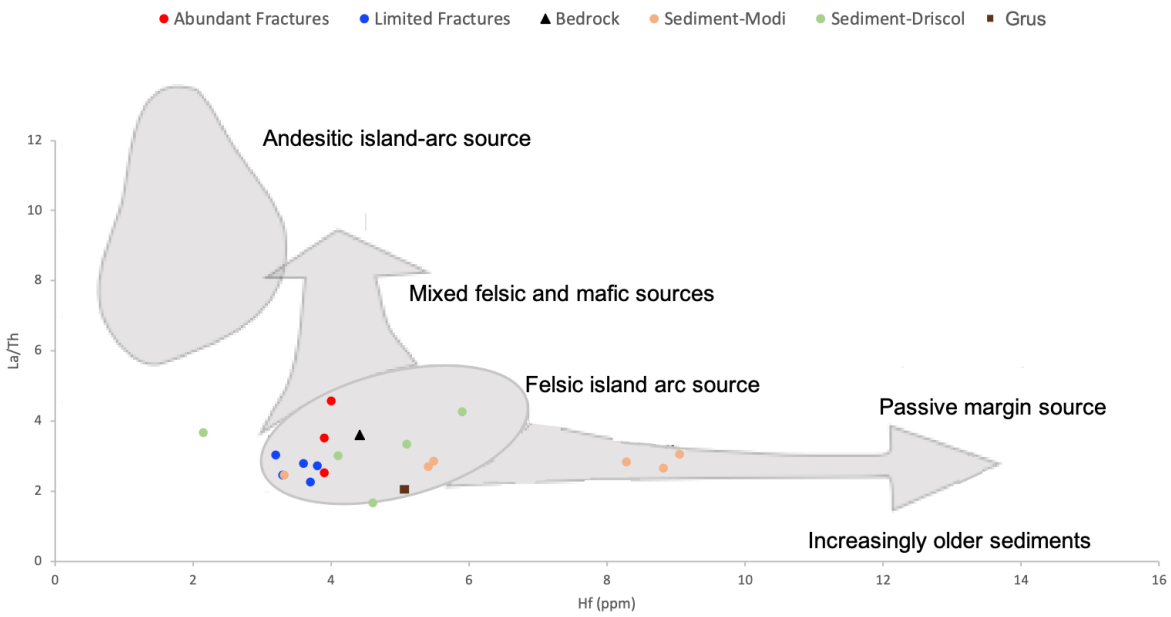


Figure 22. Plot modified from Floyd and Leveridge (1987). La/Th vs Hf ppm diagram indicating the range of sources for the Stepladder sediment (Modi, 2011; Driscoll, 2016), grus, and weathering profile into saprolite.

7.4.2 REE vs Eu/Eu*

Figures 19B – 19D compare ABN sediment, weathering profile, and grus data. Sediment (Fig. 19B) almost entirely plotted in the lower left quadrant, but the weathering profile (Fig. 19C) almost entirely plotted in the upper right quadrant. The differences between the two plotting locations indicated a compositional change from source to weathering profile to sediment, but a weathering profile is the intermediary step between bedrock and its sediment. Therefore, the different graph patterns for the ME data (Fig. 15), TE data (Fig 16A, 17), and REE data (Fig 18A) raise questions about sedimentology and geochemistry tools that attribute bedrock to sediment and associated weathering profiles. Grus more closely compositionally reflects sediment, compared to the weathering profile (Fig. 18A), and compositionally linked source and sediment (Fig. 19). Plots for LREEs vs Eu/Eu* (Appendix C10), HREEs vs Eu/Eu* (Appendix C11), and LREEs vs HREEs (Appendix C12) also support these results. Further research on the connection between grus and sediment in the Stepladder mountains needs to be investigated because these plots show that the process of grusification is potentially what is changing the composition of the sediment to be different from the bedrock.

SECTION 8. DISCUSSION

The purpose of this research was to link first-cycle sediment, which has been produced in a hot and arid climate and has had limited transport, to the Stepladder pluton source. Modi (2011) found that the transport and minimal chemical weathering processes cause the sediment to reflect a different source rock than the Stepladder granodiorite, and Driscoll (2016) concluded that sediment compositionally changes immediately upon separation from bedrock and during transport due to hydrodynamic sorting. This study tested how chemical weathering in a saprolite weathering profile formed on the pluton can lead to sediment compositional changes. The saprolite weathering profile, with CIA values ranging from 53.5- 56.5, has experienced chemical weathering, with a predicted weathering pathway of systematic replacement of Ca and Na for Al with increasing distance from the bedrock. But, the sediment from Modi (2011) and Driscoll (2016) do not plot along this trendline. Consequently, the chemical weathering processes between bedrock and sediment are more complex than initially perceived. Grus, a non-transported byproduct of chemical weathering of saprolite, had a CIA of 60 and remained on the expected weathering pathway. Grus must play a greater role in connecting the chemical dissimilarities from weathering profile to sediment and needs to be investigated further.

In the introduction, two possible explanations for the development of the weathering profile were discussed. The first is an extremely weathered profile, where the upper portion of the weathering profile has been eroded away, leaving only zone 4; the second represents a weathering profile that is in equilibrium with modern arid climate, resulting in a minimally weathered profile (zone 4). While this study was not focused on determining which explanation was correct, it did indicate that limited chemical weathering has occurred. Regardless, the two

plausible explanations would yield the same results for derived sediment. Further work would need to be done if age of the weathering profile wanted to be known.

Mechanical weathering, based on fracture density, was also analyzed to account for the physical breakup of a source rock to produce sediment. Initially, mechanical weathering was thought to be associated with chemical weathering because, if fracture density increases, and more water can pass through the material, then this would lead to increased chemical weathering, which would be quantified by CIA values. Fracture density was greatest in the top 40 cm of the weathering profile, but CIA values did not correlate to fracturing along the profile. Separation between mechanical weathering and CIA indicate a decoupling of physical and chemical processes in the Stepladder pluton.

Previous work has used provenance indicator plots as a tool to identify sediment sources (McLennan et al., 1993; Hassan et al, 1999; Roser and Korsch, 1999; Vital et al., 1999; Cullers, 2000; Do Campo and Guevara, 2005; Das et al., 2006; Blake et al., 2017). However, even in a simplified setting, weathering profile samples and sediment do not compositionally match the known bedrock source in trace elements and rare earth elements. In most instances where provenance determination is needed, sediment composition has been altered by weathering, transport, and diagenesis. Therefore, it is unclear how compositional plots and ratios can be used to interpret provenance accurately.

Implications for this study provide a cautionary tale for relying on bulk geochemistry of sediment to determine provenance. Methods and diagrams used on this thesis research, and that have been applied in many other studies, are meant to account for the effects of chemical weathering, mechanical weathering, transport, and lithification. In the case of the Stepladder pluton, the sediment produced is single-sourced, first-cycle, has undergone limited transport, and

limited chemical weathering, yet geochemical provenance reconstruction tools cannot accurately identify the Stepladder granodiorite as the source. Even more so, the weathering profile, which was the focus of this study, differs in a way that also does not reflect the sediment to bedrock compositional changes. Considering a weathering profile is thought to be the intermediary step between bedrock and sediment, the results (deviation from bedrock and sediment in provenance indicator plots) from this study complicate that understanding. Grus appears to be the potential compositional link between bedrock, weathering profile, and sediment and needs to be further analyzed to see its effects in a provenance reconstruction. This study brings to light the following question: if such a simplified setting cannot accurately identify source, then how reliable are results from studies where multiple cycles of sediment are produced, in addition to experiencing more extreme chemical weathering, and larger distances of transport? Consequently, the research conducted in the Stepladder mountains over multiple studies, continue to indicate that using geochemical tools as the only means to reconstruct provenances may not yield accurate results, and other methods would need to be used in conjunction.

SECTION 9. SUMMARY AND CONCLUSIONS

The Stepladder mountains, located in the Mojave Desert in southeastern California, provided an excellent location to test how clastic sediments acquire their composition in an arid environment. This study on a modern weathering profile that forms on top of a granodiorite (74 Ma Stepladder pluton) was designed to test whether the composition of the profile, from which overlying sediments are derived, can explain why trace and rare earth element compositions between sediments and fresh bedrock do not match well. This study has four main conclusions:

1. Nine samples of a modern weathering profile developed on the Stepladder pluton were collected from an ~ 1.5 m tall road-cut exposure. The samples were analyzed for their physical properties related to weathering. Fracture abundances and mineral weathering intensity are broken into two groups, an upper from the ground surface to 70 cm depth, and a second lower one below 70 cm. Area-normalized fracture density for samples from the upper group range between 10.4% to 7.9%, but the lower section fracture density ranges between 5.6% and 2.2%. Mineral weathering intensity for each sample is based on alteration of plagioclase, potassium feldspar, and biotite phases, all of which are susceptible to hydrolysis. Samples above the 70 cm depth break scored an average of 3.1/5 for plagioclase, 1.8/3 for potassium feldspar, and 2.0/3 for biotite. Below the 70 cm break those phases scored an average 2.44/5 for plagioclase, 1.5/3 for potassium feldspar, and 1.9/3 for biotite.
2. Although textural features identify a distinct break in physical weathering, major-element geochemistry as shown in Al_2O — CaO* + Na_2O— K_2O (A-CN-K) compositional space indicates minimal alteration (i.e., main phases remain intact, original igneous texture present, minor clay accumulation) from hydrolysis has occurred. Chemical index of

alteration (CIA) values range from ~50 to 53, which are values expected for unweathered continental crustal rocks. The CIA values show a little scatter that does not follow predicted, and well established, chemical weathering trends. Instead of showing an increase in CIA from bottom to top of the profile, the samples show a random pattern. The low CIA values show minor weathering has occurred, but the data do not show systemic changes due to the limited weathering, which makes connecting weathering profile to source more difficult than expected. The data show minor enrichments in trace elements relative to bedrock for Rb (avg. 1.47), Sr (avg. 1.24), Cs (avg. 1.07), U (avg. 2.10) and Th (avg. 1.24). There are also minor depletions relative to bedrock for Ba (avg. 0.86), Zr (avg. 0.76), Y (avg. 0.95), and Hf (avg. 0.83). Total REE for the weathering profile relative to bedrock reflects a negative slope (average $La_{BN}/Lu_{BN} = 1.31$). Separation in REE relative to bedrock are also seen with a negative HREE slope (average $Gd_{BN}/Lu_{BN} = 1.2$), varying LREE slope ($La_{BN}/Sm_{BN} = 0.8$-1.2), and a small positive europium anomaly (average $Eu_{BN}/Eu_{BN}^{*} = 1.16$) in all but two samples. Results indicate a notable change has occurred in the chemistry of the Stepladder weathering profile from the pluton, even when very limited chemical weathering has taken place.

3. Grus, non-transported product produced by the chemical weathering and disintegration of saprolite, lies directly on top of the Stepladder weathering profile. Grus shows a connecting pathway between bedrock to sediment in major-, trace-, and rare earth-elements. The CIA of grus is 60, and plots along the predicted weathering pathway in A-CN-K space. Trace elements show similar enrichments ($Cs_{BN} = 1.32$, $Sc_{BN} = 2.83$, $Y_{BN} = 1.66$, $Th_{BN} = 2.16$, $U_{BN} = 3.73$, $Zr_{BN} = 1.19$, and $Hf_{BN} = 1.31$) and depletions ($Ba_{BN} = 0.99$ and $Tl_{BN} = 0.33$) to sediment. Rare earth-element plots show a greater concentration of

grus than that of bedrock and the weathering profile. Total REE for grus reflects a positive slope ($La_{BN}/Lu_{BN} = 0.75$) with a greater positive slope in HREE ($Gd_{BN}/Lu_{BN} = 0.86$) than LREE ($La_{BN}/Sm_{BN} = 0.93$). Grus shows the strongest connection between bedrock and sediment when REEs were analyzed.

4. The Stepladder weathering profile does not provide a compositional "link" between sediment and bedrock, a hypothesis considered for this research. Grus, essentially non-transported rubble sitting on the profile appears to be the closest connection between sediment and bedrock. The weathering profile differs from bedrock in major elements, trace elements, and rare earth elements. Petrographically, there is separation between weathering profile and bedrock, seen via increased fracturing and clay concentration. Because of this, provenance indicator plots may not be as reliable as previously thought. Many of these plots do not correctly identify the Stepladder pluton as the source for both weathering profile and sediment.

REFERENCES

ActLabs, 2021, Geochemistry schedule of services & fees. p. 1-44, https://actlabs.com/wp-content/uploads/2021/07/Actlabs-Schedule-of-Services-USD-2021.pdf.

Allen, C. M., 1992, A nested diapir model for the reversely zoned Turtle Pluton, southeastern California: Transactions of the Royal Society of Edinburgh: Earth Sciences, v. 83, p. 179-190.

Anders, E., and Grevesse, N., 1989, Abundances of the elements: Meteoritic and solar: Geochimica et Cosmochimica Acta, v. 53, p. 197–214.

Anderson, J. L., 1983, Proterozoic anorogenic granite plutonism of North America: Geological Society of America Memoir, v. 161, p. 133-154.

Anderson, J.L., and Bender, E.E., 1989, Nature and origin of Proterozoic A-type granitic magmatism in the southwestern United States of America: Lithos, v. 23, p. 19–52.

Anderson, J.L., and Cullers, R.L., 1999, Paleo- and Mesoproterozoic granite plutonism of Colorado and Wyoming: Rocky Mountain Geology, v. 34, p. 149–164.

Armstrong, R.L.E.E., and Higgins, R.E., 1973, K-Ar dating of the beginning of Tertiary volcanism in the Mojave Desert, California: GSA Bulletin, v. 844, p. 1095–1100.

Armstrong-Altrin, J.S., 2015, Evaluation of two multidimensional discrimination diagrams from beach and deep-sea sediments from the Gulf of Mexico and their application to Precambrian clastic sedimentary rocks: International Geology Review, v. 57, p. 1446–1461.

Bailey, J.C., 1981, Geochemical criteria for a refined tectonic discrimination of orogenic andesites: Chemical Geology, v. 32, p. 139–154.

Banfield, F., and Eggleton, R.A., 1988, Transmission electron microscope study of biotite weathering: Clays and Clay Minerals, v. 36, p. 47–60.

Banfield, J.F., and Eggleton, R.A., 1990, Analytical transmission electron microscope studies of plagioclase, muscovite, and K-feldspar weathering: Clays and Clay Minerals, v. 38, p. 77–89.

Barth, P., Wooden, L., Coleman, D.S., and Fanning, C.M., 2000, Geochronology of the Proterozoic basement of southwesternmost North America, and the origin and evolution of the Mojave crustal province: Tectonics, v. 19, p. 616–629.

Barth, A.P., Wooden, J.L., Coleman, D.S., and Vogel, M.B., 2009, Assembling and disassembling California: A Zircon and monazite geochronologic framework for

Proterozoic crustal evolution in Southern California: The Journal of Geology, v. 117, p. 221–239.

Basto, C.F., Caxito, F. de A., do Vale, J.A.R., Silveira, D.A., Rodrigues, J.B., Alkmim, A.R., Valeriano, C. de M., and Santos, E.J. dos, 2019, An Ediacaran back-arc basin preserved in the Transversal Zone of the Borborema Province: Evidence from geochemistry, geochronology and isotope systematics of the Ipueirinha Group, NE Brazil: Precambrian Research, v. 320, p. 213–231.

Bates, R. L., and Jackson, J. A., 1987, Glossary of geology.

Bhatia, M.R., and Crook, K.A.W., 1986, Trace element characteristics of graywackes and tectonic setting discrimination of sedimentary basins: Contributions to Mineralogy and Petrology, v. 92, p. 181–193.

Bhatia, M.R., and Taylor, S.R., 1981, Trace-element geochemistry and sedimentary provinces: A study from the Tasman Geosyncline, Australia: Chemical Geology, v. 33, p. 115–125.

Bird, P., 1998, Kinematic history of the Laramide orogeny in latitudes 35-49N, western United States: Tectonics, v. 17, p. 780–801.

Bjorkum, P.A., and Gjelsvik, N., 1988, An Isochemical Model for Formation of Authigenic Kaolinite, K-Feldspar, and Illite in Sediments: Journal of Sedimentary Petrology, v. 58, p. 506–511.

Blake, J.M., Peters, S.C., and Johannesson, K.H., 2017, Application of REE geochemical signatures for Mesozoic sediment provenance to the Gettysburg Basin, Pennsylvania: Sedimentary Geology, v. 349, p. 103–111.

Bonich-Wissink, M.B., 2017, Isotopic characterization of bedrock, sediments, and minerals as provenance tools: Examples from an inselberg in the Mojave Desert of SE California.

Braun, J.J., and Pagel, M., 1994, Geochemical and mineralogical behavior of REE, Th and U in the Akongo lateritic profile (SW Cameroon): Catena, v. 21, p. 173–177.

Burchfiel, B. C., and Davis, G. A., 1981, Mojave Desert and environments, in Ernst, W. G., ed., The geotectonic development of California (Rubey Volume 1): Englewood Cliffs, New Jersey, Prentice-Hall, p. 217-252

Chappell, B. W. and White, A. J. R., 1974, Two contrasting granite types, in Pacific Geol., v. 8, p. 173–174.

Condie, K.C., 1991, Another look at rare earth elements in shales: Geochimica et Cosmochimica Acta, v. 55, p. 2527–2531.

Condie, K.C., Boryta, M.D., Liu, J., and Qian, X., 1992, The origin of khondalites: geochemical evidence from the Archean to Early Proterozoic granulite belt in the North China craton: Precambrian Research, v. 59, p. 207–223.

Condie, K.C., 1993, Chemical composition and evolution of the upper continental crust: Contrasting results from surface samples and shales: Chemical Geology, v. 104, p. 1–37.

Cox, R., Lowe, D.R., and Cullers, R.L., 1995, The influence of sediment recycling and basement composition on evolution of mudrock chemistry in the southwestern United States: Geochimica et Cosmochimica Acta, v. 59, p. 2919–2940.

Cramer, J.J., and Nesbitt, H.W., 1983, Mass-balance relations and trace-element mobility during continental weathering of various igneous rocks: Sciences Geologiques - Memoire, v. 73, p. 63–73.

Cullers, R.L., Basu, A., and Suttner, L.J., 1988, Geochemical Signature of Provenance in Sand-Size Material in Soils and Stream Sediments Near the Tobacco Root batholith, Montana, USA: Chemical Geology, v. 70, p. 335–348.

Cullers, R.L., 2000, The geochemistry of shales, siltstones and sandstones of Pennsylvanian-Permian age, Colorado, USA: Implications for provenance and metamorphic studies: Lithos, v. 51, p. 181–203.

Das, B.K., AL-Mikhlafi, A.S., and Kaur, P., 2006, Geochemistry of Mansar Lake sediments, Jammu, India: Implication for source-area weathering, provenance, and tectonic setting: Journal of Asian Earth Sciences, v. 26, p. 649–668.

Descourvieres, C., Douglas, G., Leyland, L., Hartog, N., and Prommer, H., 2011, Geochemical reconstruction of the provenance, weathering, and deposition of detrital-dominated sediments in the Perth Basin: The Cretaceous Leederville Formation, south-west Australia: Sedimentary Geology, v. 236, p. 62–76.

Dewitt, E.D., Armstrong, R.L., Sutter, J.F., and Zartman, R.E., 1984, U-Th-Pb, Rb-Sr, and Ar-Ar mineral and whole-rock isotopic systematics in a metamorphosed granitic terrane, southeastern California: GSA Bulletin, v. 95, p. 723–739.

Do Campo, M., and Ribeiro Guevara, S., 2005, Provenance analysis and tectonic setting of late Neoproterozoic metasedimentary successions in NW Argentina: Journal of South American Earth Sciences, v. 19, p. 143–153.

Driscoll, C., 2016, Role of sorting on the composition of siliciclastic sediment: Implications for interpreting provenance after limited transport in an arid climate: University of Tennessee-Knoxville, p. 1–107.

Duebendorfer, E.M., Chamberlain, K.R., and Jones, C.S., 2001, Paleoproterozoic tectonic history of the Cerbat Mountains northwestern Arizona: Implications for crustal assembly in the

southwestern United States: Bulletin of the Geological Society of America, v. 113, p. 575–590.

Eker, C.S., Sipahi, F., and Kaygusuz, A., 2012, Trace and rare earth elements as indicators of provenance and depositional environments of Lias cherts in Gumushane, NE Turkey: Chemie der Erde, v. 72, p. 167–177.

Eswaran, H., and Heng, Y.Y., 1976, The Weathering of Biotite in a Profile on Gneiss in Malaysia: Geoderma, p. 9–20.

Fedo, C.M., Nesbitt, H.W., and Young, G.M., 1995, Unravelling the effects of potassium metasomatism in sedimentary rocks and paleosols, with implications for paleoweathering conditions and provenance: Geology, v. 23, p. 921–924.

Fedo, C.M., Young, G.M., Nesbitt, H.W., and Hanchar, J.M., 1997, Potassic and sodic metasomatism in the Southern Province of the Canadian Shield: Evidence from the Paleoproterozoic Serpent Formation, Huronian Supergroup, Canada: Precambrian Research, v. 84, p. 17–36.

Fedo, C.M., and Cooper, J.D., 2001, Sedimentology and sequence stratigraphy of Neoproterozoic and Cambrian units across a craton-margin hinge zone, southeastern California, and implications for the early evolution of the Cordilleran margin: Sedimentary Geology, v. 141–142, p. 501–522.

Fedo, C.M., Sircombe, K.N., and Rainbird, R.H., 2003, Detrital zircon analysis of the sedimentary record: Reviews in Minerology and Geochemistry, v. 53, p. 277–303.

Fedo, C.M., McGlynn, I.O., and McSween, H.Y., 2015, Grain size and hydrodynamic sorting controls on the composition of basaltic sediments: Implications for interpreting martian soils: Earth and Planetary Science Letters, v. 423, p. 67–77.

Floyd, P. A., and Leveridge, B. E., 1987, Tectonic environment of the Devonian Gramscatho basin, south Cornwall: framework mode and geochemical evidence from turbiditic sandstones: Journal of the Geological Society, v.144, p. 531-542.

Foster, D.A., Harrison, T.M., Miller, C.F., and Keith, A.H., 1990, The 40Ar/30Ar Thermochronology of the Eastern Mojave Desert, California, and adjacent Western Arizona with implications for the evolution of metamorphic core complexes: Journal of Geophysical Research, v. 95, p. 20,005-20,024.

Foster, D.A., Miller, D.S., and Miller, C.F., 1991, Tertiary extension in the Old Woman Mountains area, California: Evidence from apatite fission track analysis: Tectonics, v. 10, p. 875–886.

Foster, D.A., Miller, C.F., Harrison, T.M., and Hoisch, T.D., 1992, 40 Ar/ 39 Ar thermochronology and thermobarometry of metamorphism, plutonism, and tectonic

denudation in the Old Woman Mountains area, California: Geological Society of America Bulletin, v. 104, p. 176–191.

Fralick, P., 2003, Geochemistry of clastic sedimentary rocks ratio techniques, p. 85–103.

Frost, B.R., Barnes, C.G., Collins, W.J., Arculus, R.J., Ellis, D.J., and Frost, C.D., 2001, A geochemical classification for granitic rocks: Journal of Petrology, v. 42, p. 2033–2048.

Garcia, D., Fonteilles, M., and Moutte, J., 1994, Sedimentary fractionations between Al, Ti, and Zr and the genesis of strongly peraluminous granites: The Journal of Geology, v.102, p. 411-422.

Gerber, M.E., Miller, C.F., Wooden, J.L. and Foster, D.A., 1991. Plutonism at the eastern edge of the Cordilleran Jurassic magmatic belt, Mojave Desert, California: Geol. Soc. Am., Abstr. Prog., 23: A249.

Gong, Q., Deng, J., Yang, L., Zhang, J., Wang, Q., and Zhang, G., 2011, Behavior of major and trace elements during weathering of sericite–quartz schist: Journal of Asian Earth Sciences, v. 42, p. 1–13.

Goodge, J.W., and Vervoort, J.D., 2006, Origin of Mesoproterozoic A-type granites in Laurentia: Hf isotope evidence: Earth and Planetary Science Letters, v. 243, p. 711–731.

Govindaraju, K., 1994, 1994 Compilation of Working Values and Sample Description for 383 Geostandards: Geostandards Newsletter, v. 18, p. 1–158.

Hassan, S., Ishiga, H., Roser, B.P., Dozen, K., and Naka, T., 1999, Geochemistry of Permian-Triassic shales in the Salt Range, Pakistan: Implications for provenance and tectonism at the Gondwana margin: Chemical Geology, v. 158, p. 293–314.

Hemley, J.J., and Jones, W.R., 1964, Chemical aspects of hydrothermal alteration with emphasis on hydrogen metasomatism: Economic Geology, v. 59, p. 538–569.

Hereford, R., Webb, R.H., and Longpré, C.I., 2006, Precipitation history and ecosystem response to multidecadal precipitation variability in the Mojave Desert region, 1893-2001: Journal of Arid Environments, v. 67, p. 13–34.

Howard, K.., and John, B.E., 1987, Crustal extension along a rooted system of imbricate low-angle faults: Colorado River extensional corridor, California and Arizonal: Continental Extensional Tectonics, v. 28, p. 299–311.

Johnsson, M.J., 1993, The system controlling the composition of clastic sediments: Geological Society of America, Special paper 284, p. 1–19.

Johnsson, M.J., Stallard, R.F., and Meade, R.H., 1988, First-cycle quartz arenites in the Orinoco river basin, Venezuela and Colombia: The Journal of Geology, v. 96, p. 263–277.

Kastner, M., and Siever, R., 1979, Low temperature feldspars in sedimentary rocks: American Journal of Science, v. 279, p. 435- 479.

Kingsbury, J.A., Miller, C.F., Wooden, J.L., and Harrison, T.M., 1993, Monazite paragenesis and U-Pb systematics in rocks of the eastern Mojave Desert, California, U.S.A.: implications for thermochronometry: Chemical Geology, v. 110, p. 147–167.

Laceby, J.P., McMahon, J., Evrard, O., and Olley, J., 2015, A comparison of geological and statistical approaches to element selection for sediment fingerprinting: Journal of Soils and Sediments, v. 15, p. 2117–2131.

Lawrence, M.G., and Kamber, B.S., 2006, The behaviour of the rare earth elements during estuarine mixing-revisited: Marine Chemistry, v. 100, p. 147–161.

Little, M.G., and Aeolus Lee, C.T., 2006, On the formation of an inverted weathering profile on Mount Kilimanjaro, Tanzania: Buried paleosol or groundwater weathering?: Chemical Geology, v. 235, p. 205–221.

Liu, B., Wang, Y., Su, X., and Zheng, H., 2013, Elemental geochemistry of northern slope sediments from the South China Sea: Implications for provenance and source area weathering since Early Miocene: Geochemistry, v. 73, p. 61–74.

Maniar, P.D., and Piccolli, P.M., 1989, Tectonic discrimination of granitoids: GSA Bulletin, v. 101, p. 635–643.

Mangold, N., Baratoux, D., Arnalds, O., Bardintzeff, J.M., Platevoet, B., Grégoire, M., and Pinet, P., 2011, Segregation of olivine grains in volcanic sands in Iceland and implications for Mars: Earth and Planetary Science Letters, v. 310, p. 233–243.

McLennan, S. M., and Taylor, S. R., 1980, Th and U in sedimentary rocks: crustal evolution and sedimentary recycling: Nature, v. 285, p. 621-624.

McLennan, S. M., 1989. Rare earth elements in sedimentary rocks; influence of provenance and sedimentary processes. Reviews in Mineralogy and Geochemistry, v. 21, no. 1, p. 169-200.

McLennan, S. M., McCulloch, M. T., Taylor, S. R., and Maynard, J. B., 1989, Effects of sedimentary sorting on neodymium isotopes in deep-sea turbidites: Nature, v. 337, p. 547-549.

McLennan, S.M., 1993, Weathering and global denudation: Journal of Geology, v. 101, p. 295–303.

McLennan, S. M., Hemming, S., McDaniel, D. K., and Hanson, G. N., 1993, Geochemical approaches to sedimentation, provenance, and tectonics: Special Papers-Geological Society of America, p. 21.

McLennan, S. M., 2001, Relationships between the trace element composition of sedimentary rocks and upper continental crust: Geochemistry, Geophysics, Geosystems, v. 2.

McLennan, S.M., Taylor, S.R. and Hemming, S.R., 2006, Composition, differentiation, and evolution of continental crust: Constraints from sedimentary rocks and heat flow: Evolution and Differentiation of the Continental Crust: Cambridge University Press, pp. 92-134.

Medaris, L.G., Boerboom, T.J., Jicha, B.R., and Singer, B.S., 2015, Metasaprolite in the McGrath Gneiss, Minnesota, USA: Viewing Paleoproterozoic weathering through a veil of metamorphism and metasomatism: Precambrian Research, v. 257, p. 83–93.

Middelburg, J.J., van der Weijden, C.H., and Woittiez, J.R.W., 1988, Chemical processes affecting the mobility of major, minor and trace elements during weathering of granitic rocks: Chemical Geology, v. 68, p. 253–273.

Miller, C.F., and Wooden, J.L., 1994, Anatexis, hybridization and the modification of ancient crust: Mesozoic plutonism in the Old Woman Mountains area, California: Lithos, v. 32, p. 111–133.

Miyashiro, A., 1970, Volcanic rock series in island arcs and active continental margins.: American Journal of Science, v. 274, p. 321–355.

Modi, A.L., 2011, Processes controlling the composition of first-cycle sediments deposited in an arid-climate, with implications for provenance reconstruction studies: University of Tennessee- Knoxville, 1–165 p.

Munksgaard, N.C., Lim, K., and Parry, D.L., 2003, Rare earth elements as provenance indicators in North Australian estuarine and coastal marine sediments: Estuarine, Coastal and Shelf Science, v. 57, p. 399–409.

Nesbitt, W.H., and Young, G.M., 1982, Early Proterozoic climates and plate motions inferred from major element chemistry of lutites: Nature, v. 299, p. 715–717.

Nesbitt, H.W., and Young, G.M., 1984, Prediction of some weathering trends of plutonic and volcanic rocks based on thermodynamic and kinetic considerations: Geochimica et Cosmochimica Acta, v. 48, p. 1523–1534.

Nesbitt, H.W., and Young, G.M., 1989, Formation and Diagenesis of Weathering Profiles, v. 97, p. 129–147.

Nesbitt, H.W., 1992, Diagenesis and metasomatism of weathering profiles, with emphasis on Precambrian paleosols: Weathering, soils & paleosols, p. 127–152.

Nesbitt, H.W., and Young, G.M., 1996, Petrogenesis of sediments in the absence of chemical weathering: Effects of abrasion and sorting on bulk composition and mineralogy: Sedimentology, v. 43, p. 341–358.

Nesbitt, H.W., and Markovics, G., 1997, Weathering of granodioritic crust, long-term storage of elements in weathering profiles, and petrogenesis of siliciclastic sediments: Geochimica et Cosmochimica Acta, v. 61, p. 1653–1670.

Nichols, G. J., 2005, Sedimentary evolution of the Lower Clair Group, Devonian, west of Shetland: climate and sediment supply controls on fluvial, aeolian and lacustrine deposition.: Geological Society of London, Petroleum Geology Conference series v. 6, n. 1, p. 957-967.

Norton, K.P., Molnar, P., and Schlunegger, F., 2014, The role of climate-driven chemical weathering on soil production: Geomorphology, v. 204, p. 510–517.

Novoselov, A.A., and de Souza Filho, C.R., 2015, Potassium metasomatism of Precambrian paleosols: Precambrian Research, v. 262, p. 67–83.

Óladóttir, B.A., Sigmarsson, O., Larsen, G. and Devidal, J.L., 2011, Provenance of basaltic tephra from Vatnajökull subglacial volcanoes, Iceland, as determined by major-and trace-element analyses, The Holocene, v. 21, i. 7, p.1037-1048.

Oliva, P., Viers, J., and Dupré, B., 2003, Chemical weathering in granitic environments: Chemical Geology, v. 202, p. 225–256.

Peacock, M. A.,1931, Classification of igneous rock series: The Journal of Geology, v. 39, p. 54-67.

Pearce, J.A., 1996, A user's guide to basalt discrimination diagrams, Trace element geochemistry of volcanic rocks: applications for massive sulphide exploration, Geological Association of Canada, Short Course Notes, v. 12, p. 79-113.

Peng, B., Rate, A., Song, Z., Yu, C., Tang, X., Xie, S., Tu, X., and Tan, C., 2014, Geochemistry of major and trace elements and Pb–Sr isotopes of a weathering profile developed on the Lower Cambrian black shales in central Hunan, China: Applied Geochemistry, v. 51, p. 191–203.

Prave, A.R., 1999, Two diamicties, two cap carbonates, two 13C excursions, two rifts: The Neoproterozoic Kingston Peak Formation, Death Valley, California: Geology, v. 27, p. 339–342.

Rainbird, R.H., Nesbitt, H.W., and Donaldson, J.A., 1990, Formation and diagenesis of a sub-Huronian saprolith: Comparison with a modern weathering profile: The Journal of Geology, v. 98, p. 801–822.

Ramasamy, N., Franz L., K., Jong, J., Muthuvairavasamy, R., Muhammad, A.A., Dayong, V., Shanmugarajah, L., Vusak, N., Sivanasvaran, K., and Kinanthi, D., 2021, Geochemistry of the Palaeocene-Eocene Upper Kelalan Formation, NW Borneo: Implications on

palaeoweathering, tectonic setting, and provenance: Geological Journal, v. 56, p. 2500–2527.

Roser, B. P., and Korsch, R. J., 1999, Geochemical characterization, evolution and source of a Mesozoic accretionary wedge: the Torlesse terrane, New Zealand.: Geological Magazine, v.136, n. 5, p. 493-512.

Schlesinger, W.H., 1982, Carbon storage in the caliche of arid soils: a case study from Arizona: Soil Science., v. 133, p. 247–255.

Schoenborn, W.A., and Fedo, C.M., 2011, Provenance and paleoweathering reconstruction of the Neoproterozoic Johnnie Formation, southeastern California: Chemical Geology, v. 285, p. 231–255.

Shand, S. J., 1943, Eruptive rocks: their genesis, composition, classification, and their relation to ore deposits with a chapter on meteorites, No. 552.

Service, N.P., 2016, Weather: Mojave National Preserve, https://www.nps.gov/moja/planyourvisit/weather.htm.

Spencer, J.E., 1985, Miocene low-angle normal faulting and dike emplacement, Homer Mountain and surrounding areas, southeastern California and southernmost Nevada (USA): Geological Society of America Bulletin, v. 96, p. 1140–1155.

“Stepladder Weathering Profile.” 34 º 41’05.15” N and 114 º 50’19.69” W. Google Earth. June 15, 2017. October 2019.

Stewart, A.D., 1990, Geochemistry, provenance and climate of the Upper Proterozoic Stoer Group in Scotland: Scottish Journal of Geology, v. 26, p. 89 LP – 97.

Stoffer, P. W., 2004, Desert landforms and surface processes in the Mojave National Preserve and vicinity, No. 2004-1007.

Streckeisen, A., 1976, To each plutonic rock its proper name: Earth Science Reviews, v. 12, p. 1–33, doi:10.1016/0012-8252(76)90052-0.

Strickland, B.A., Wooden, J.L., Mattinson, C.G., Ushikubo, T., Miller, D.M., and Valley, J.W., 2013, Proterozoic evolution of the Mojave crustal province as preserved in the Ivanpah Mountains, southeastern California: Precambrian Research, v. 224, p. 222–241.

Suttner, L. J., Basu, A., and Mack, G. H., 1981, Climate and the origin of quartz arenites.: Journal of Sedimentary Research, v. 5, 1 n. 4, p. 1235-1246.

Taylor, S. R., and McLennan, S. M., 1985, The continental crust: its composition and evolution.

Thyne, G., Boudreau, B.P., Ramm, M., and Midtbø, R.E., 2001, Simulation of potassium feldspar dissolution and illitization in the Statfjord Formation, North Sea: AAPG Bulletin, v. 85, p. 621–635.

Tole, M.P., 1985, The kinetics of dissolution of zircon ($ZrSiO_4$): Geochimica et Cosmochimica Acta, v. 49, p. 453–458.

U.S. Climate Data., 2019., Temperature- Precipitation- Sunshine- Snowfall., https://www.usclimatedata.com/climate/mojave/california/united-states/usca0715

Um, I. kwon, Choi, M.S., Bahk, J.J., and Song, Y.H., 2013, Discrimination of sediment provenance using rare earth elements in the Ulleung basin, East Japan Sea: Marine Geology, v. 346, p. 208–219.

Van de Kamp, P.C., and Leake, B.E., 1997, Mineralogy, geochemistry, provenance and sodium metasomatism of Torridonian rift basin clastic rocks, NW Scotland: Scottish Journal of Geology, v. 33, p. 105–124.

Vital, H., Stattegger, K., and Garbe-Schoenberg, C. D., 1999, Composition and trace-element geochemistry of detrital clay and heavy-mineral suites of the lowermost Amazon River; a provenance study: Journal of Sedimentary Research, v. 69, n. 3, p. 563-575.

Wang, W., Cawood, P.A., Pandit, M.K., Zhou, M.-F., and Zhao, J.-H., 2018, Evolving passive- and active-margin tectonics of the Paleoproterozoic Aravalli Basin, NW India: GSA Bulletin, v. 131, p. 426–443.

Whalen, J.B., and Hildebrand, R.S., 2019, Trace element discrimination of arc, slab failure, and A-type granitic rocks: Lithos, v. 348–349, p. 105-179.

Wooden, J.L., and Miller, D.M., 1990, Chronologic and isotopic framework for Early Proterozoic crustal evolution in the eastern Mojave Desert Region, SE California: Journal of Geophysical Research, v. 95, p. 20,133-20,146.

Xiong, S., Ding, Z., Zhu, Y., Zhou, R., and Lu, H., 2010, A ~6Ma chemical weathering history, the grain size dependence of chemical weathering intensity, and its implications for provenance change of the Chinese loess-red clay deposit: Quaternary Science Reviews, v. 29, p. 1911–1922.

Zen, E. A., 1988, Phase relations of peraluminous granitic rocks and their petrogenetic implications: Annual Review of Earth and Planetary Sciences, v. 16, p. 21-51.

Zhang, Y., Pe-Piper, G., and Piper, D.J.W., 2014, Sediment geochemistry as a provenance indicator: Unravelling the cryptic signatures of polycyclic sources, climate change, tectonism and volcanism: Sedimentology, v. 61, p. 383–410.

APPENDICES

APPENDIX A
Supplementary Images



Appendix A 1. Hand sample of 0119SL_13, grus.



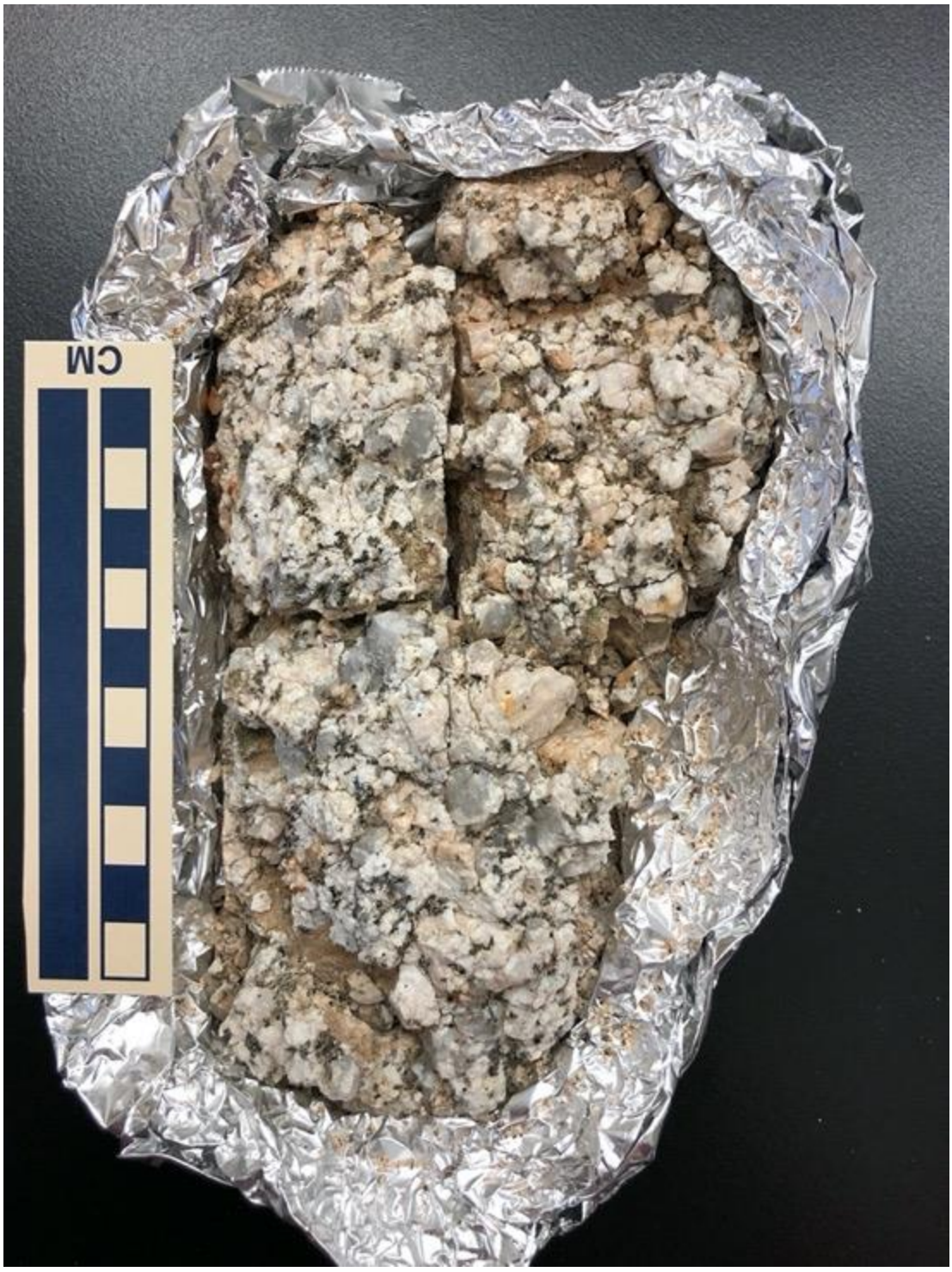
Appendix A 2. Hand sample of 0119SL_0.



Appendix A 3. Hand sample of 0119SL_1.



Appendix A 4. Hand sample of 0119SL_2.



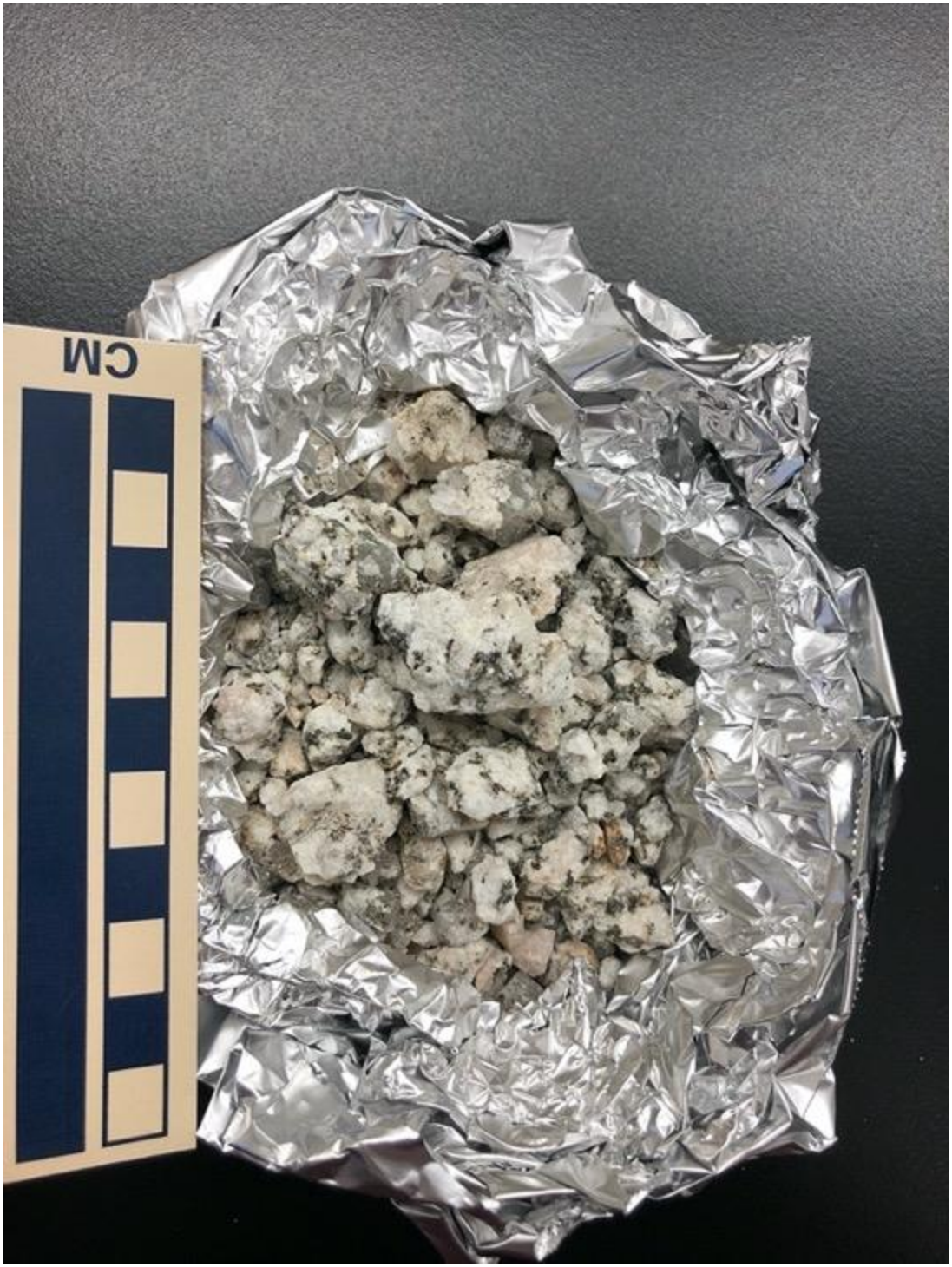
Appendix A 5. Hand sample of 0119SL_3.



Appendix A 6. Hand sample of 0119SL_4



Appendix A 7. Hand sample of 0119SL_5.



Appendix A 8. Hand sample of 0119SL_6.



Appendix A 9. Hand sample of 0119SL_7.



Appendix A 10. Hand sample of 19_SL_2.



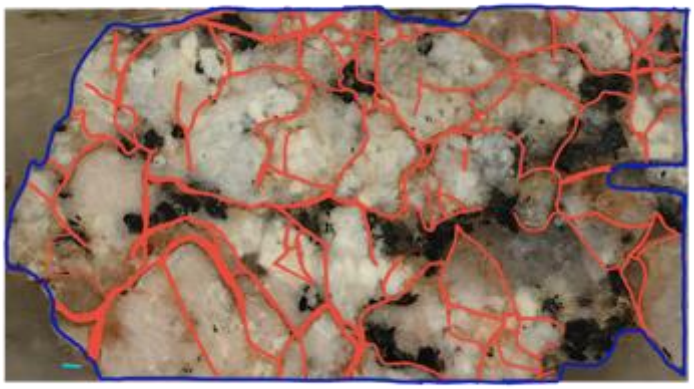
Appendix A 11. Cone and quartering method



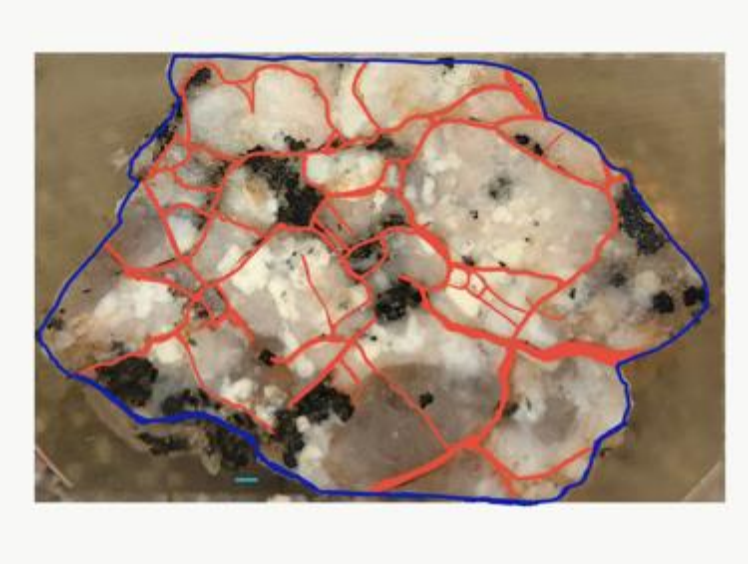
Appendix A 12. Sample in ceramic dish before and after powdering.



Appendix A 13. Fracture lines on sample 0119SL_0



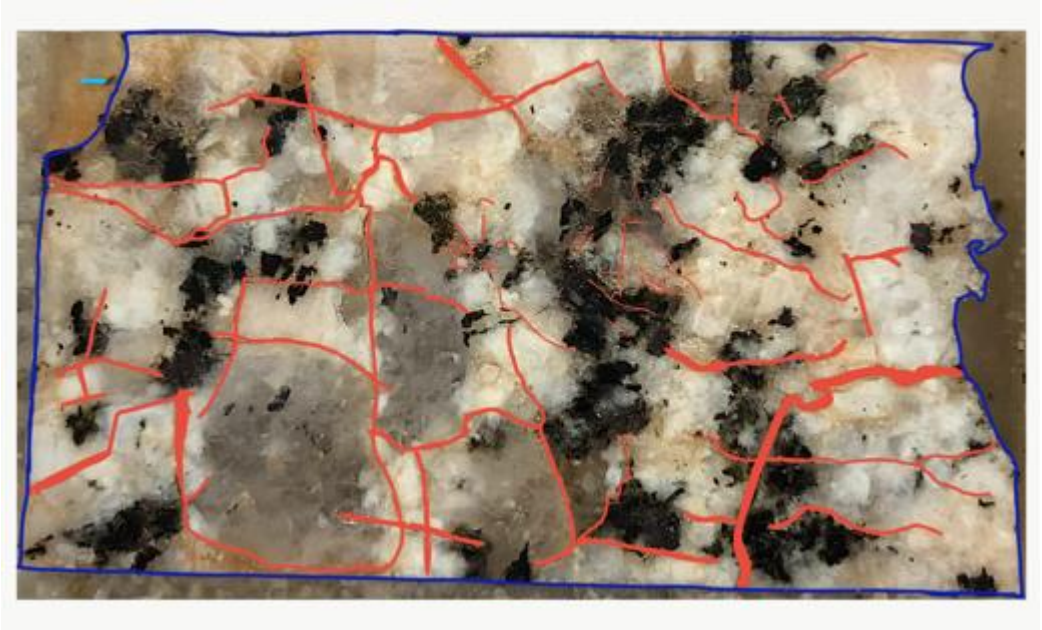
Appendix A 14. Fracture lines on sample 0119SL_1



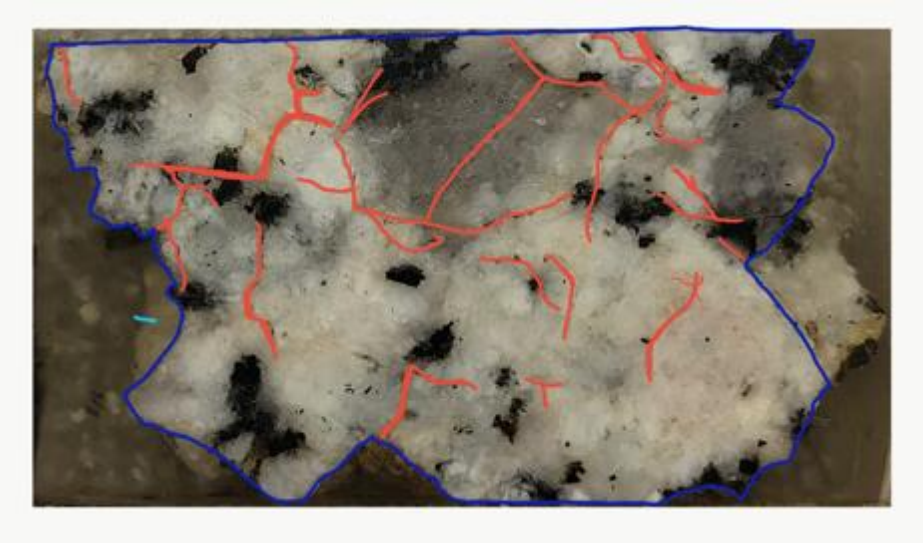
Appendix A 15. Fracture lines on sample 0119SL_2



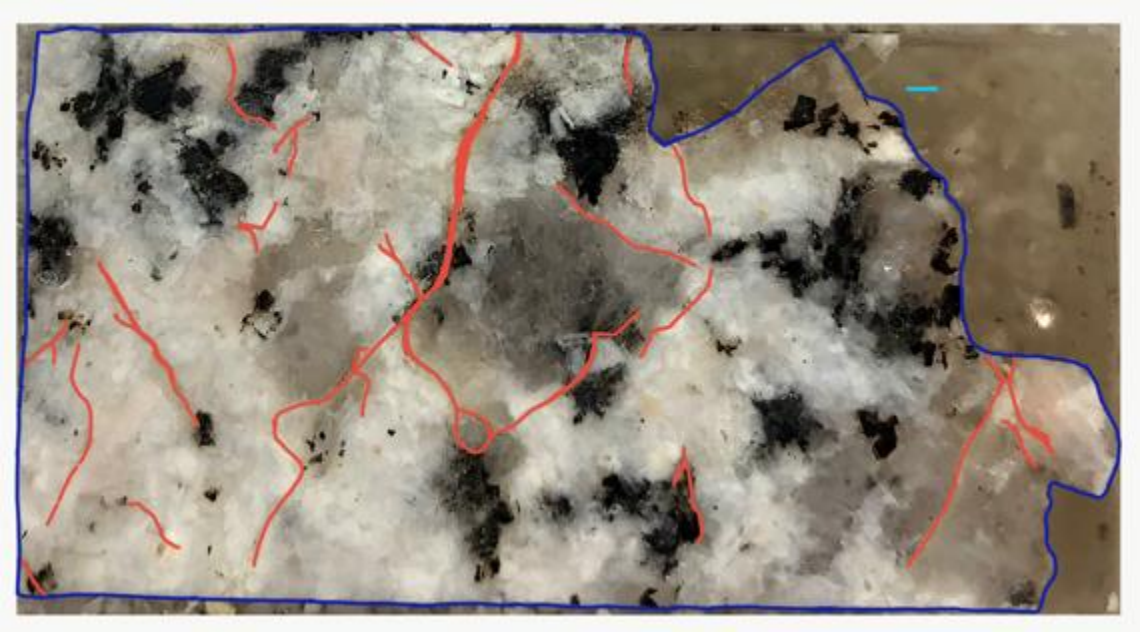
Appendix A 16. Fracture lines on sample 0119SL_3



Appendix A 17. Fracture lines on sample 0119SL_4



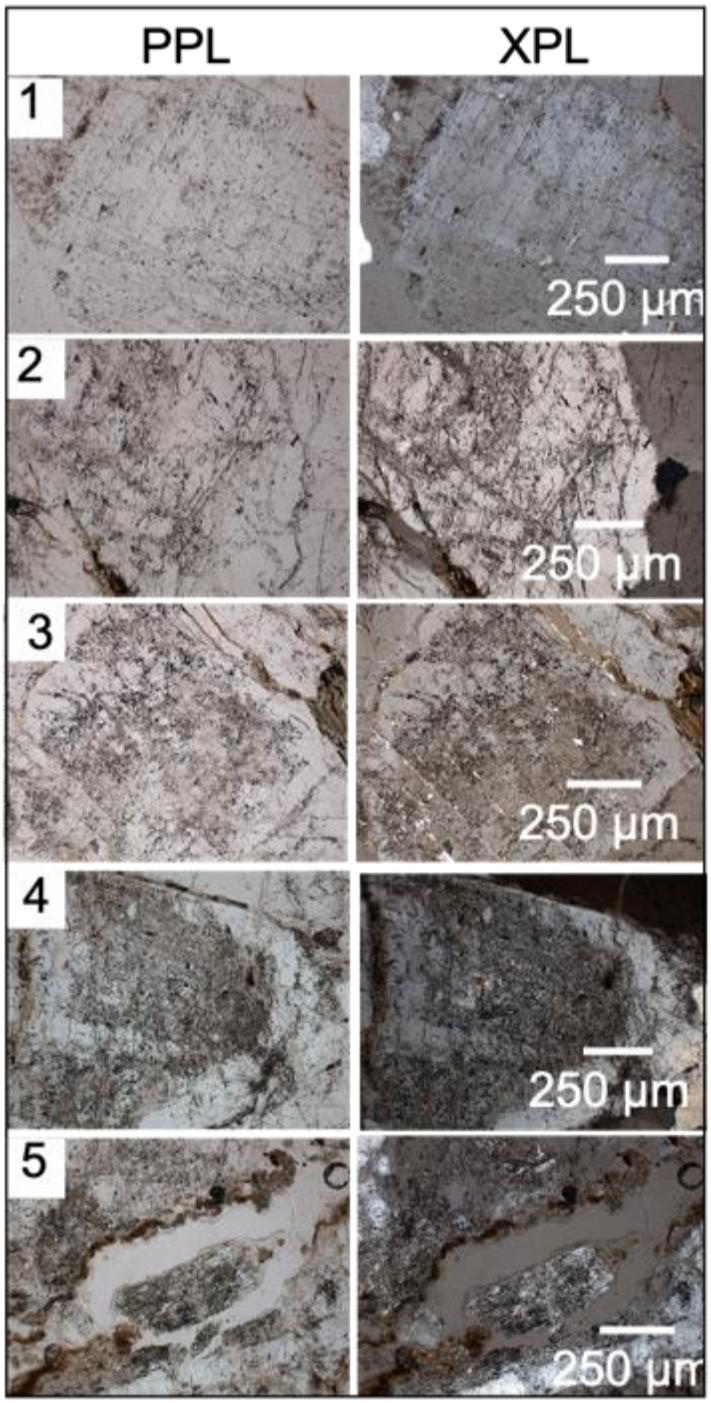
Appendix A 18. Fracture lines on sample 0119SL_5



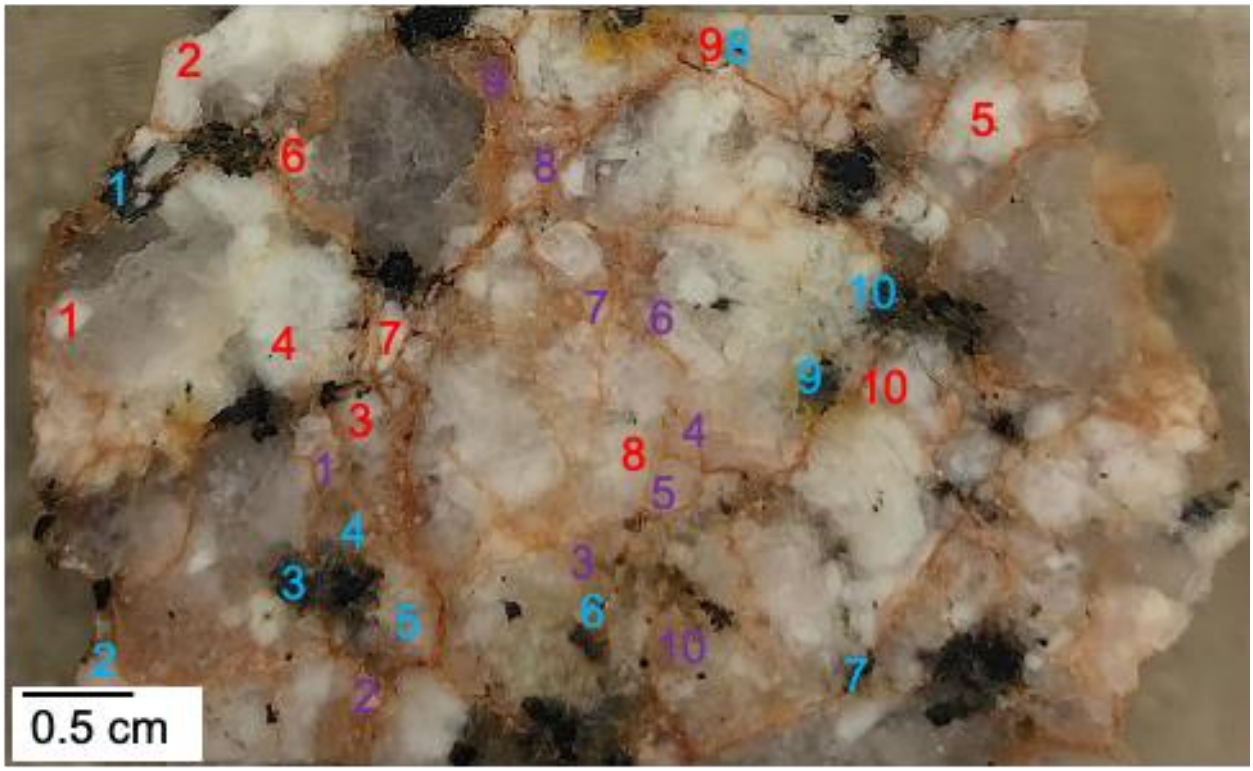
Appendix A 19. Fracture lines on sample 0119SL_7



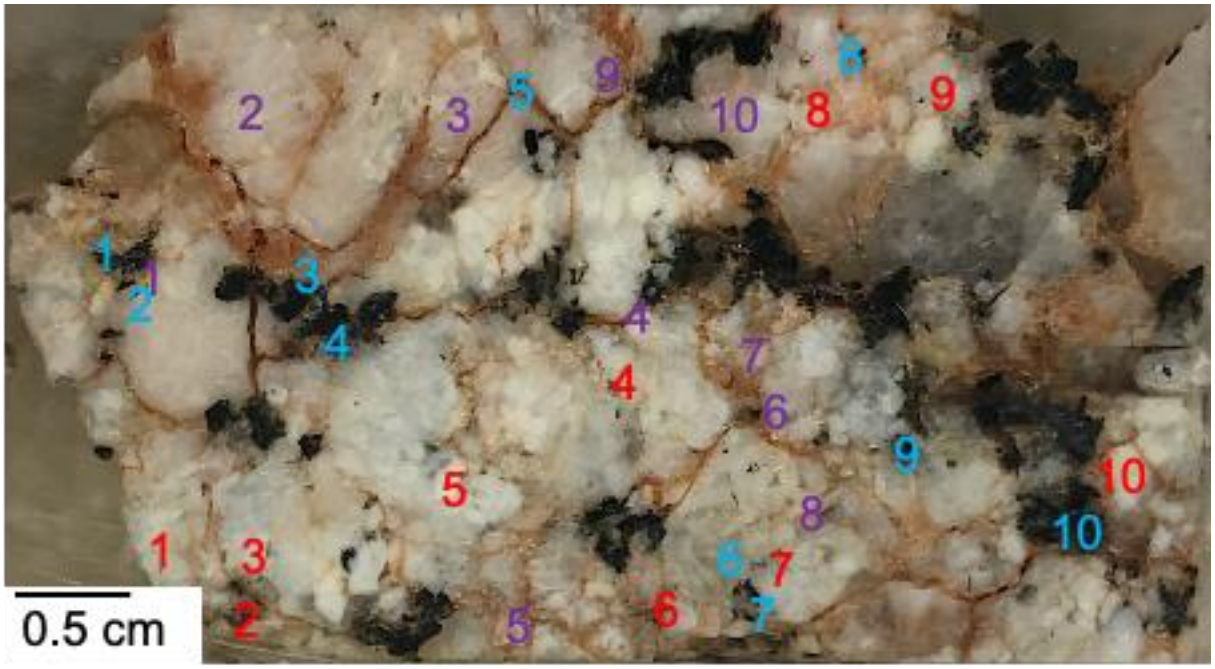
Appendix A 20. Fracture lines on sample 19_SL_2



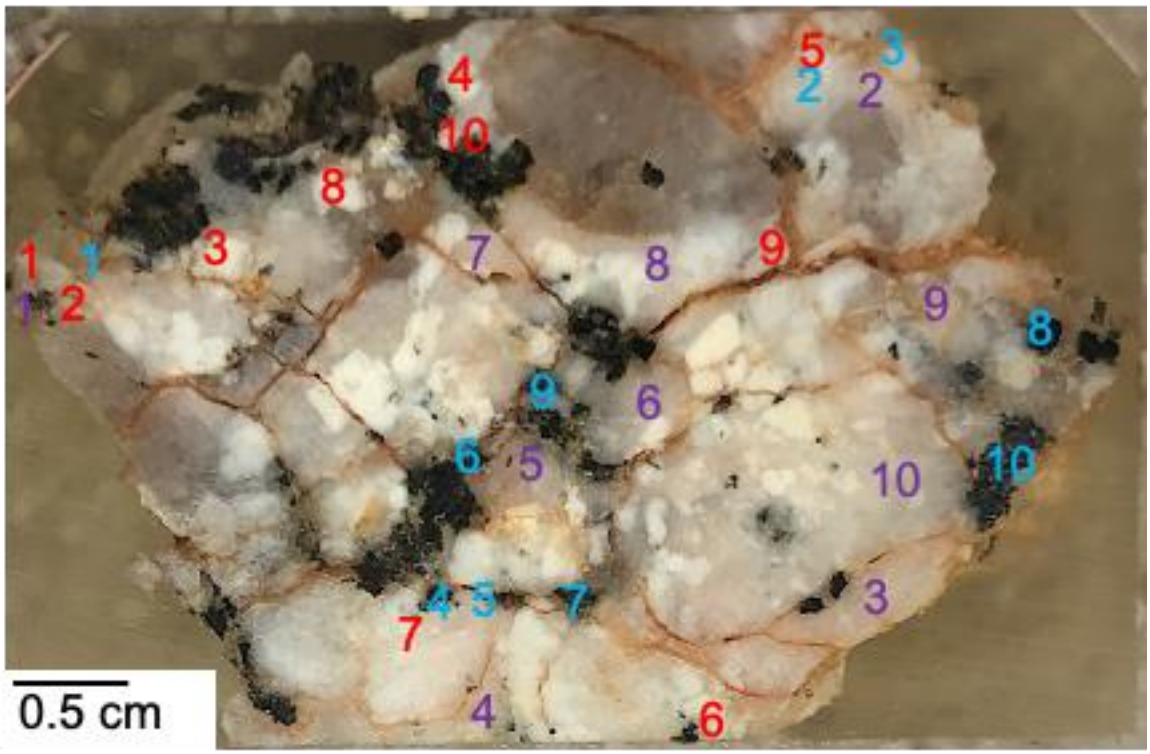
Appendix A 21. Plagioclase feldspar grains found throughout different samples that were used as a baseline for scoring weathered grains. PPL left side, XPL right side. Numbers on the PPL photomicrograph correspond to intensity values each grain would be scored.



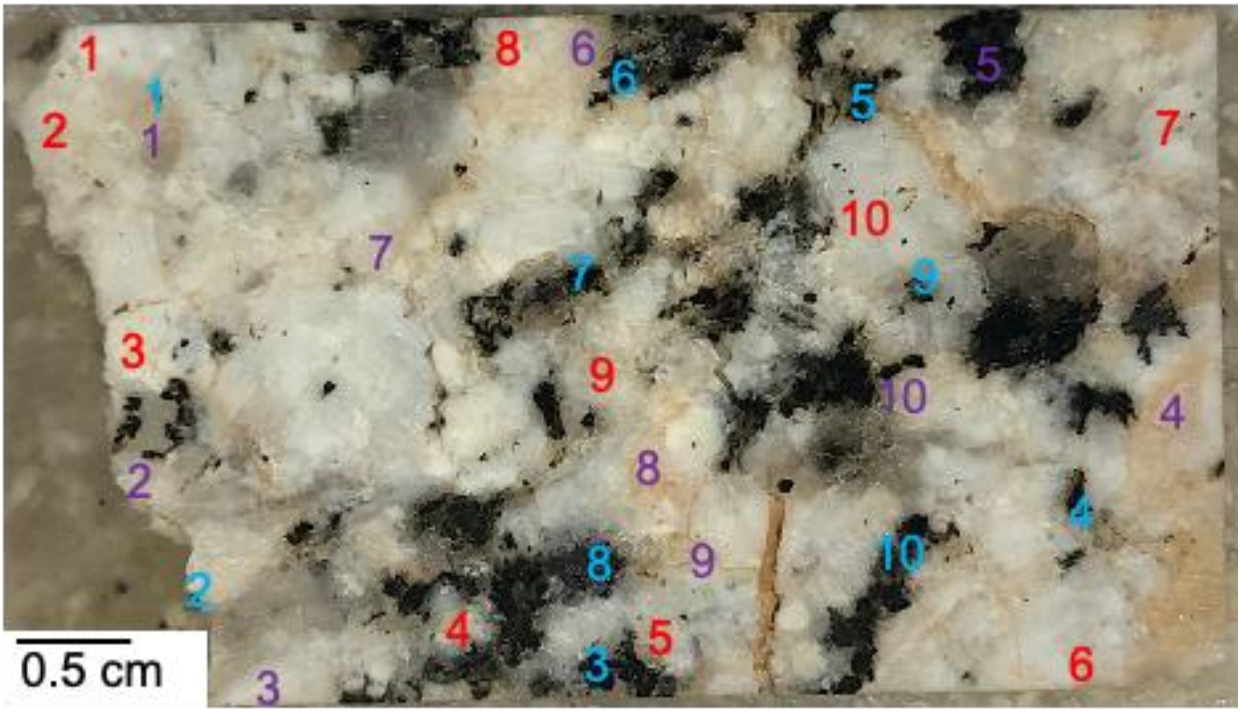
Appendix A 22. Location of where each mineral was found when collecting weathering scores for sample 0119SL_0. Blue = biotite, red = plagioclase, purple = potassium feldspar.



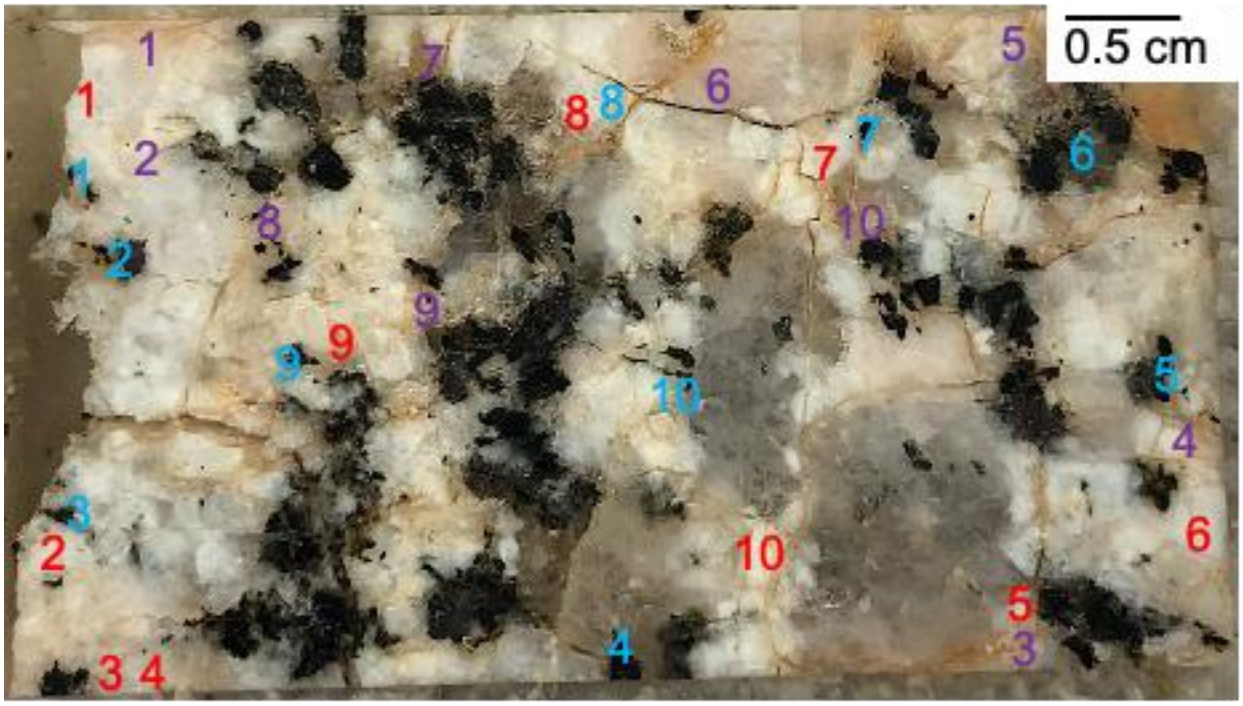
Appendix A 23. Location of where each mineral was found when collecting weathering scores for sample 0119SL_1. Blue = biotite, red = plagioclase, purple = potassium feldspar.



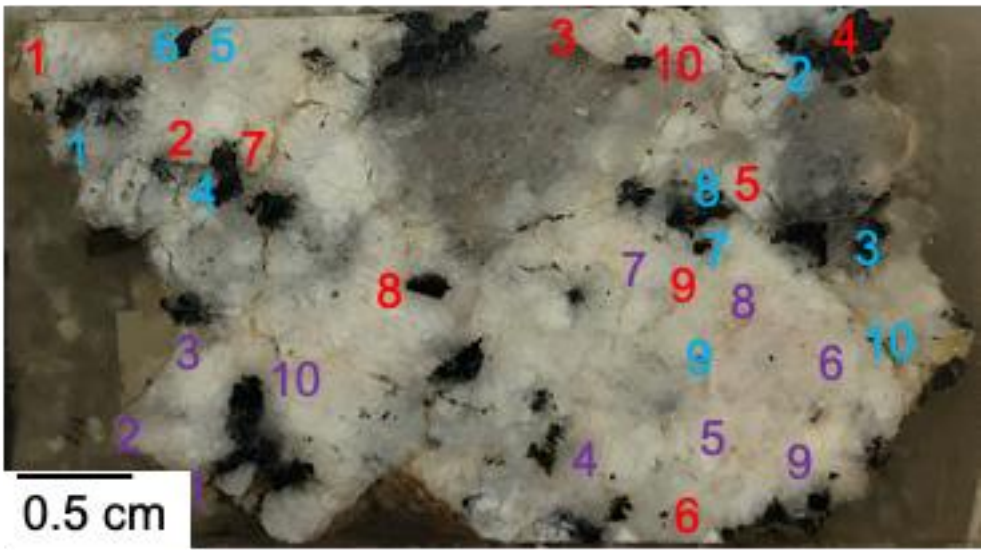
Appendix A 24. Location of where each mineral was found when collecting weathering scores for sample 0119SL_2. Blue = biotite, red = plagioclase, purple = potassium feldspar.



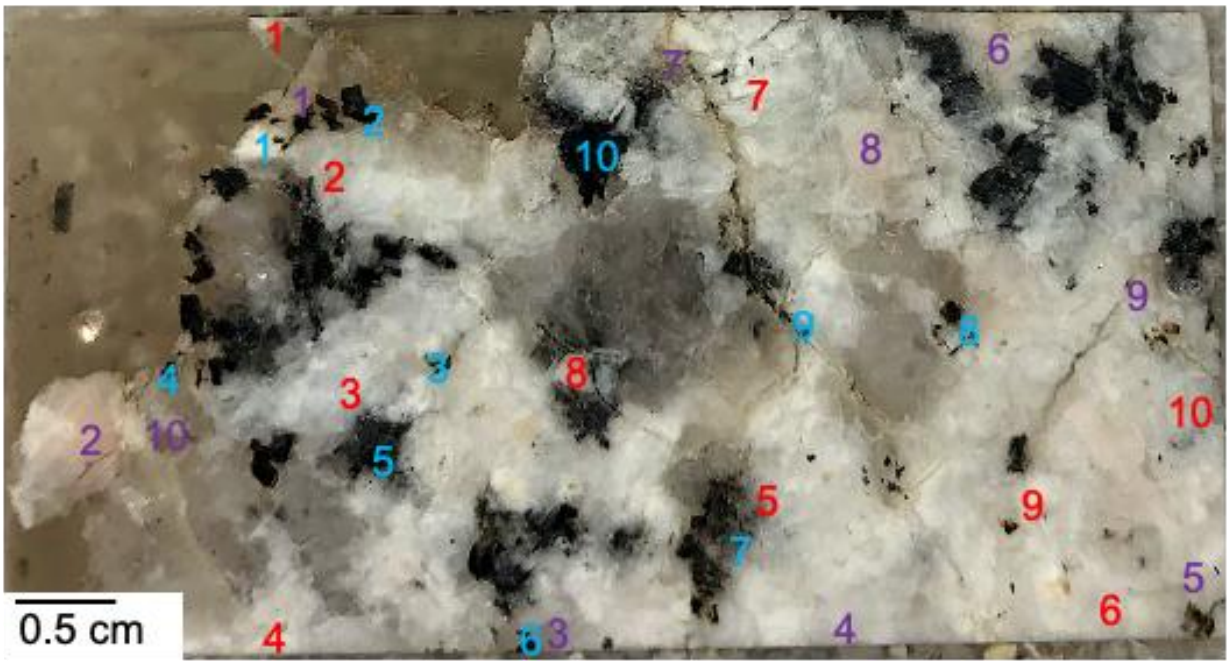
Appendix A 25. Location of where each mineral was found when collecting weathering scores for sample 0119SL_3. Blue = biotite, red = plagioclase, purple = potassium feldspar.



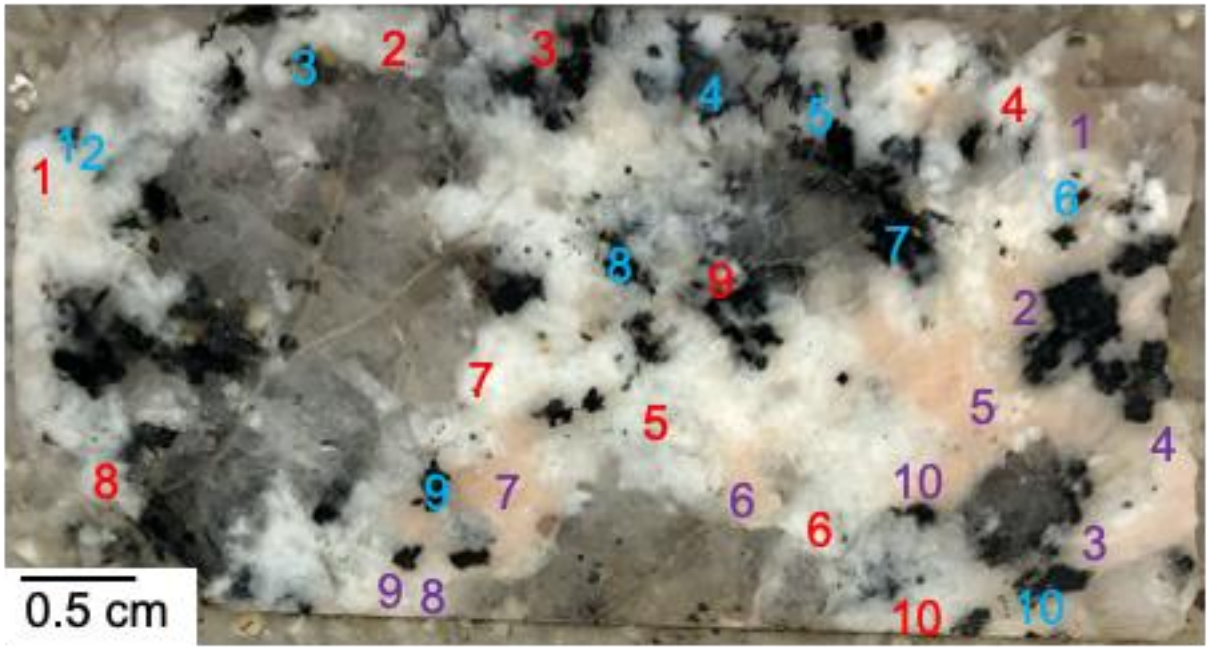
Appendix A 26. Location of where each mineral was found when collecting weathering scores for sample 0119SL_4. Blue = biotite, red = plagioclase, purple = potassium feldspar.



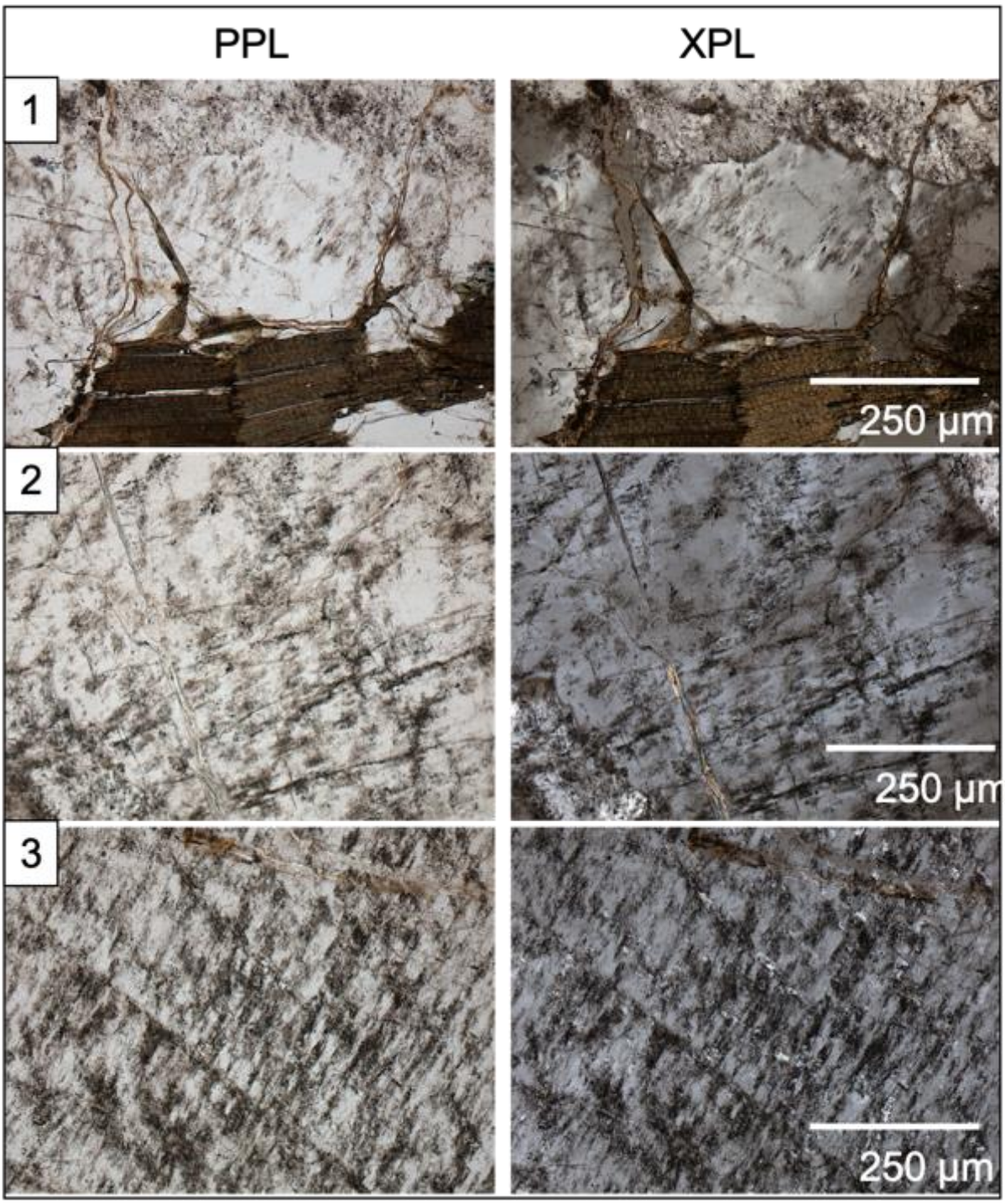
Appendix A 27. Location of where each mineral was found when collecting weathering scores for sample 0119SL_5. Blue = biotite, red = plagioclase, purple = potassium feldspar.



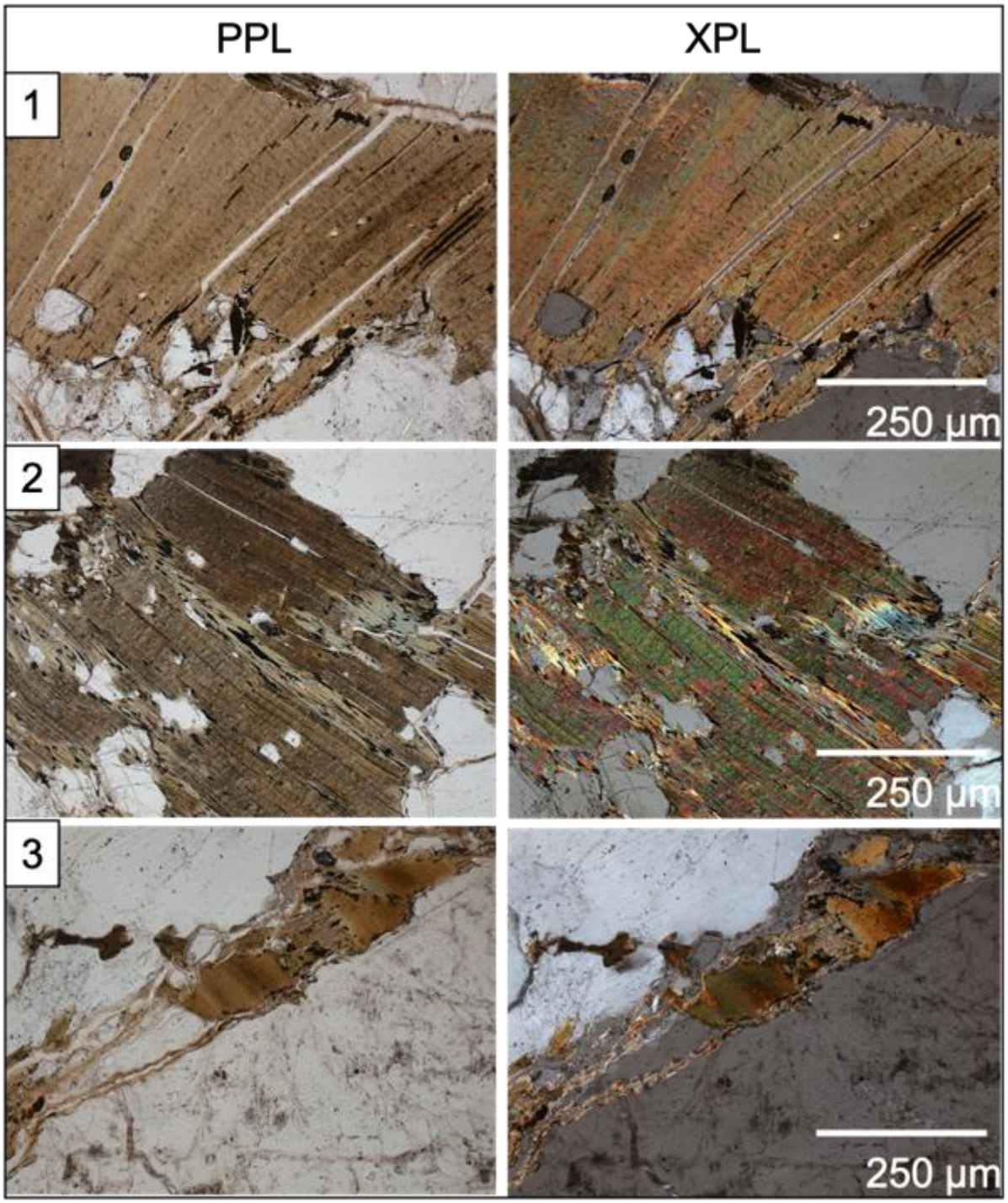
Appendix A 28. Location of where each mineral was found when collecting weathering scores for sample 0119SL_7. Blue = biotite, red = plagioclase, purple = potassium feldspar.



Appendix A 29. Location of where each mineral was found when collecting weathering scores for sample 19_SL_2. Blue = biotite, red = plagioclase, purple = potassium feldspar.



Appendix A 30. Potassium feldspar grains found throughout different samples that were used as a baseline for scoring weathered grains. PPL left side, XPL right side. Numbers on the PPL photomicrograph correspond to intensity values each grain would be scored. Scoring criteria described in description category to the left.



Appendix A 31. Biotite grains used as a baseline for scoring weathering intensity. PPL left side, XPL right side. Numbers on the PPL photomicrograph correspond to intensity values each grain would be scored

APPENDIX B
Supplementary Tables

Appendix B 1. Table of standards and standard error for major elements to test instrumentation used for this study. Sample 0119SL_04 has been shortened to 4.

Sample	SiO2	TiO2	Al2O3	Fe2O3(T)	FeO(T)	MnO	MgO	CaO	Na2O	K2O	P2O5
4	71.42	0.32	15.46	1.58	1.42	0.03	0.59	2.15	4.34	3.25	0.12
duplicate	72.08	0.31	15.18	1.57	1.41	0.03	0.58	2.15	4.26	3.20	0.11
smp/dup	0.99	1.02	1.02	1.01	1.01	1.00	1.02	1.00	1.02	1.02	1.09
% error	0.92	1.60	1.84	0.64	0.64	0	1.72	0	1.88	1.56	9.09
19_SL_2	69.85	0.34	16.22	1.93	1.74	0.04	0.53	2.13	4.08	4.60	0.13
duplicate	70.09	0.33	15.76	1.91	1.72	0.04	0.50	2.08	3.98	4.48	0.10
smp/dup	1.00	1.03	1.03	1.01	1.01	1.03	1.06	1.02	1.03	1.03	1.30
% error	0.34	3.20	2.84	1.04	1.04	2.50	5.66	2.35	2.45	2.61	23.08
RGM_1	72.89	0.27	14.13	1.92	1.73	0.04	0.27	1.22	4.05	4.40	0.04
USGS Std	73.45	0.27	13.72	1.86	1.67	0.04	0.28	1.15	4.07	4.30	0.05
smp/std	0.99	1.01	1.03	1.03	1.03	1.14	0.98	1.06	1.00	1.02	0.83
% error	0.76	1.50	2.99	3.23	3.23	13.89	1.82	6.09	0.49	2.33	16.67

Appendix B 2 Table of standards and standard error for trace elements to test instrumentation used for this study. * indicates values below detection limit and are listed at the detection limit value. – denotes element not analyzed.

Element	4	duplicate	smp/ dup	% error	19_SL_2	duplicate	smp/ dup	% error	RGM_1	USGS std	smp/ std	% error
Rb	97.00	93.00	1.04	4.12	127.00	126.00	1.01	0.79	151.00	149.00	1.01	1.34
Ba	608.00	609.00	1.00	0.16	1383.00	1334.00	1.04	3.54	857.00	807.00	1.06	6.20
Cs	1.20	1.20	1.00	0	1.00	1.00	1.00	0	9.50	9.60	0.99	1.04
Sr	511.00	505.00	1.01	1.17	571.00	546.00	1.05	4.38	110.00	108.00	1.02	1.85
Sc	3.00	3.00	1.00	0	3.00	2.00	1.50	33.33	5.00	4.40	1.14	13.64
Y	5.30	5.10	1.04	3.77	5.70	5.90	0.97	3.51	22.50	25.00	0.90	10
Th	6.68	6.98	0.96	4.49	7.90	7.71	1.02	2.41	14.50	15.10	0.96	3.97
U	0.95	0.86	1.10	9.47	1.08	1.11	0.97	2.78	5.90	5.80	1.02	1.72
Pb	19.00	18.00	1.06	5.26	22.00	22.00	1.00	0	24.00	24.00	1.00	0
Zr	118.00	105.00	1.12	11.02	130.00	118.00	1.10	9.23	204.00	219.00	0.93	6.85
Hf	3.30	3.10	1.06	6.06	3.80	3.30	1.15	13.16	5.90	6.20	0.95	4.84
Nb	4.80	5.40	0.89	12.50	5.60	5.90	0.95	5.36	7.00	8.90	0.79	21.35
Ta	0.26	0.27	0.96	3.85	0.35	0.39	0.90	11.43	0.83	0.95	0.87	12.63
V	25.00	22.00	1.14	12.00	29.00	27.00	1.07	6.90	15.00	13.00	1.15	15.38
Tl	0.43	0.35	1.23	18.60	0.51	0.50	1.02	1.96	0.81	0.93	0.87	12.90
Ni	*20.00	*20.00	-	-	*20.00	*20.00	-	-	*20.00	4.40	-	-
Cu	*10.00	*10.00	-	-	*10.00	*10.00	-	-	10.00	11.60	0.86	-
Zn	40.00	50.00	0.80	25.00	50.00	50.00	1.00	0	30.00	32.00	0.94	6.25
Ga	21.00	20.00	1.05	4.76	20.00	21.00	0.95	5	16.00	15.00	1.07	6.67
As	-	-	-	-	*0.50	-	-	-	-	3.00	-	-
Be	3.00	3.00	1.00	-	3.00	3.00	1.00	-	3.00	1.89	1.59	-
Ge	0.60	0.70	0.86	-	0.70	0.80	0.88	-	0.80	1.30	0.62	-
W	2.20	2.00	1.10	-	*0.50	*0.50	-	-	*0.50	1.50	-	-

Appendix B 3. Table of standards and standard error for rare earth elements to test instrumentation used for this study. – denotes element not analyzed.

Element	4	duplicate	smp/ dup	% error	19_SL_2	duplicate	smp/ dup	% error	RGM_ 1	USGS std	smp/ std	% error
La	20.30	21.20	0.96	4.43	25.60	28.50	0.90	11.33	23.70	24.00	0.99	1.25
Ce	39.20	40.80	0.96	4.08	48.90	53.90	0.91	10.22	46.40	47.00	0.99	1.28
Pr	4.28	4.41	0.97	3.04	4.96	5.62	0.88	13.31	5.38	4.70	1.14	14.47
Nd	15.20	14.90	1.02	1.97	17.20	19.20	0.90	11.63	18.00	19.00	0.95	5.26
Pm	-	-	-	-	-	-	-	-	-	-	-	-
Sm	2.65	2.38	1.11	10.19	2.63	2.60	1.01	1.14	4.05	4.30	0.94	5.81
Eu	0.60	0.65	0.92	8.29	0.62	0.69	0.89	11.94	0.56	0.66	0.85	14.55
Gd	1.75	1.45	1.21	17.14	1.73	1.79	0.97	3.47	3.73	3.70	1.01	0.81
Tb	0.20	0.20	1.00	0	0.22	0.22	1.00	0.00	0.61	0.66	0.92	7.58
Dy	0.95	0.93	1.02	2.11	1.08	1.14	0.95	5.56	3.56	4.08	0.87	12.75
Ho	0.17	0.18	0.94	5.88	0.20	0.20	1.00	0.00	0.72	0.95	0.76	24.21
Er	0.50	0.46	1.09	8.00	0.56	0.51	1.10	8.93	2.25	2.60	0.87	13.46
Tm	0.07	0.06	1.20	16.44	0.08	0.07	1.11	10.00	0.34	0.37	0.93	7.03
Yb	0.46	0.38	1.21	17.39	0.52	0.50	1.04	3.85	2.42	2.60	0.93	6.92
Lu	0.07	0.06	1.03	3.03	0.09	0.09	1.02	2.30	0.39	0.41	0.96	3.90

Appendix B 4. Fracture percentage calculations. Sample 6 is grayed out due to disintegration during transport, data collected represents one small piece that remained cohesive.

	Depth (cm)	Whole Area (mm^2)	Fracture Area (mm^2)	Percentage
0119SL_0	5	402.92	31.911	7.92%
0119SL_1	20	900.194	93.41	10.38%
0119SL_2	40	410.242	38.53	9.39%
0119SL_3	75	533.476	24.365	4.57%
0119SL_4	85	1343.145	76.06	5.66%
0119SL_5	105	600.87	21.33	3.55%
0119SL_6	125	357.354	14.461	4.05%
0119SL_7	150	764.773	16.838	2.20%
Fresh Bedrock		805.523	6.367	0.79%

Appendix B 5. Average plus standard deviation of weathering score for each mineral phase. Pl = plagioclase feldspar, Ksp = potassium feldspar, Bt= biotite. Note that plagioclase was rated on a scale of 1-5 and ksp and bt were scored on a 1-3 scale.

	Pl (1-5)	Ksp (1-3)	Bt (1-3)
0119SL_0	3.5 ± 1.1	2.4 ± 0.7	2.3 ± 0.9
0119SL_1	3.1 ± 1.0	1.5 ± 0.5	1.9 ± 0.7
0119SL_2	2.7 ± 1.3	1.6 ± 0.7	1.8 ± 0.7
0119SL_3	3 ± 1.2	1.7 ± 0.8	2 ± 0.9
0119SL_4	2.6 ± 1.0	1.4 ± 0.5	2 ± 0.8
0119SL_5	2.7 ± 0.9	1.4 ± 0.5	2.1 ± 0.8
0119SL_6	2.2 ± 1.0	1.5 ± 0.5	1.4 ± 0.7
0119SL_7	1.7 ± 0.9	1.6 ± 0.7	2 ± 0.8
Bedrock	1.2 ± 0.4	1.4 ± 0.5	2 ± 0.8

Appendix B 6. A-CN-K and A-CNK-FM data points in molar proportions. CaO* = CaO – (10/3) * P_2O_5 – CO_2.

		A	CN	K		A	CNK	FM	
	CaO*	CIA			Sum				Sum
0119SL_13	0	60.05	24.24	15.71	100.00	50.57	33.64	15.79	100.00
0119SL_0	0.02	53.69	29.52	16.79	100.00	48.86	42.14	9.00	100.00
0119SL_1	0.02	54.48	32.30	13.22	100.00	47.89	40.01	12.10	100.00
0119SL_2	0.01	56.54	28.03	15.43	100.00	49.06	37.71	13.23	100.00
0119SL_3	0.01	56.37	28.52	15.11	100.00	49.24	38.10	12.66	100.00
0119SL_4	0.02	55.03	32.43	12.54	100.00	48.90	39.96	11.14	100.00
0119SL_5	0.02	54.91	32.36	12.73	100.00	48.30	39.66	12.04	100.00
0119SL_6	0.02	53.57	29.58	16.85	100.00	48.40	41.95	9.65	100.00
0119SL_7	0.02	55.76	31.67	12.57	100.00	47.98	38.06	13.96	100.00
Fresh Bedrock									
19_SL_2	0.03	51.54	32.64	15.82	100.00	45.98	43.24	10.79	100.00
ST09-02*	0.03	50.14	37.06	12.81	100.00	44.47	44.23	11.30	100.00
CF00-18*	0.04	49.67	38.03	12.29	100.00	44.30	44.88	10.83	100.00
Avg Bedrock	0.04	50.46	35.88	13.66	100.00	44.93	44.11	10.97	100.00

Appendix B 7. Percent CO_2 mixing model using caliche (30.6 ppm $CO_{2)}$ and bedrock (0 ppm $CO_{2)}$.

%Caliche	% Bedrock	%C02	%Caliche	% Bedrock	%C02	%Caliche	% Bedrock	%C02	%Caliche	% Bedrock	%C02
0	1	0	0.0235	0.9765	0.7191	0.047	0.953	1.4382	0.075	0.925	2.295
0.001	0.999	0.0306	0.024	0.976	0.7344	0.048	0.952	1.4688	0.076	0.924	2.3256
0.002	0.998	0.0612	0.025	0.975	0.765	0.049	0.951	1.4994	0.077	0.923	2.3562
0.003	0.997	0.0918	0.0255	0.9745	0.7803	0.05	0.95	1.53	0.078	0.922	2.3868
0.004	0.996	0.1224	0.026	0.974	0.7956	0.051	0.949	1.5606	0.079	0.921	2.4174
0.005	0.995	0.153	0.027	0.973	0.8262	0.052	0.948	1.5912	0.08	0.92	2.448
0.006	0.994	0.1836	0.028	0.972	0.8568	0.053	0.947	1.6218	0.081	0.919	2.4786
0.0065	0.9935	0.1989	0.029	0.971	0.8874	0.054	0.946	1.6524	0.082	0.918	2.5092
0.007	0.993	0.2142	0.03	0.97	0.918	0.055	0.945	1.683	0.083	0.917	2.5398
0.008	0.992	0.2448	0.031	0.969	0.9486	0.056	0.944	1.7136	0.084	0.916	2.5704
0.009	0.991	0.2754	0.032	0.968	0.9792	0.057	0.943	1.7442	0.085	0.915	2.601
0.0095	0.9905	0.2907	0.0325	0.9675	0.9945	0.058	0.942	1.7748	0.086	0.914	2.6316
0.01	0.99	0.306	0.033	0.967	1.0098	0.059	0.941	1.8054	0.087	0.913	2.6622
0.011	0.989	0.3366	0.034	0.966	1.0404	0.06	0.94	1.836	0.088	0.912	2.6928
0.012	0.988	0.3672	0.035	0.965	1.071	0.061	0.939	1.8666	0.089	0.911	2.7234
0.013	0.987	0.3978	0.036	0.964	1.1016	0.062	0.938	1.8972	0.09	0.91	2.754
0.014	0.986	0.4284	0.037	0.963	1.1322	0.063	0.937	1.9278	0.091	0.909	2.7846
0.015	0.985	0.459	0.038	0.962	1.1628	0.064	0.936	1.9584	0.0915	0.9085	2.7999
0.016	0.984	0.4896	0.039	0.961	1.1934	0.065	0.935	1.989	0.092	0.908	2.8152
0.017	0.983	0.5202	0.04	0.96	1.224	0.066	0.934	2.0196	0.093	0.907	2.8458
0.018	0.982	0.5508	0.0405	0.9595	1.2393	0.067	0.933	2.0502	0.094	0.906	2.8764
0.019	0.981	0.5814	0.041	0.959	1.2546	0.068	0.932	2.0808	0.095	0.905	2.907
0.0195	0.9805	0.5967	0.042	0.958	1.2852	0.069	0.931	2.1114	0.096	0.904	2.9376
0.02	0.98	0.612	0.043	0.957	1.3158	0.07	0.93	2.142	0.097	0.903	2.9682
0.0205	0.9795	0.6273	0.044	0.956	1.3464	0.071	0.929	2.1726	0.098	0.902	2.9988
0.021	0.979	0.6426	0.0445	0.9555	1.3617	0.072	0.928	2.2032	0.099	0.901	3.0294
0.022	0.978	0.6732	0.045	0.955	1.377	0.073	0.927	2.2338	0.1	0.9	3.06
0.023	0.977	0.7038	0.046	0.954	1.4076	0.074	0.926	2.2644			

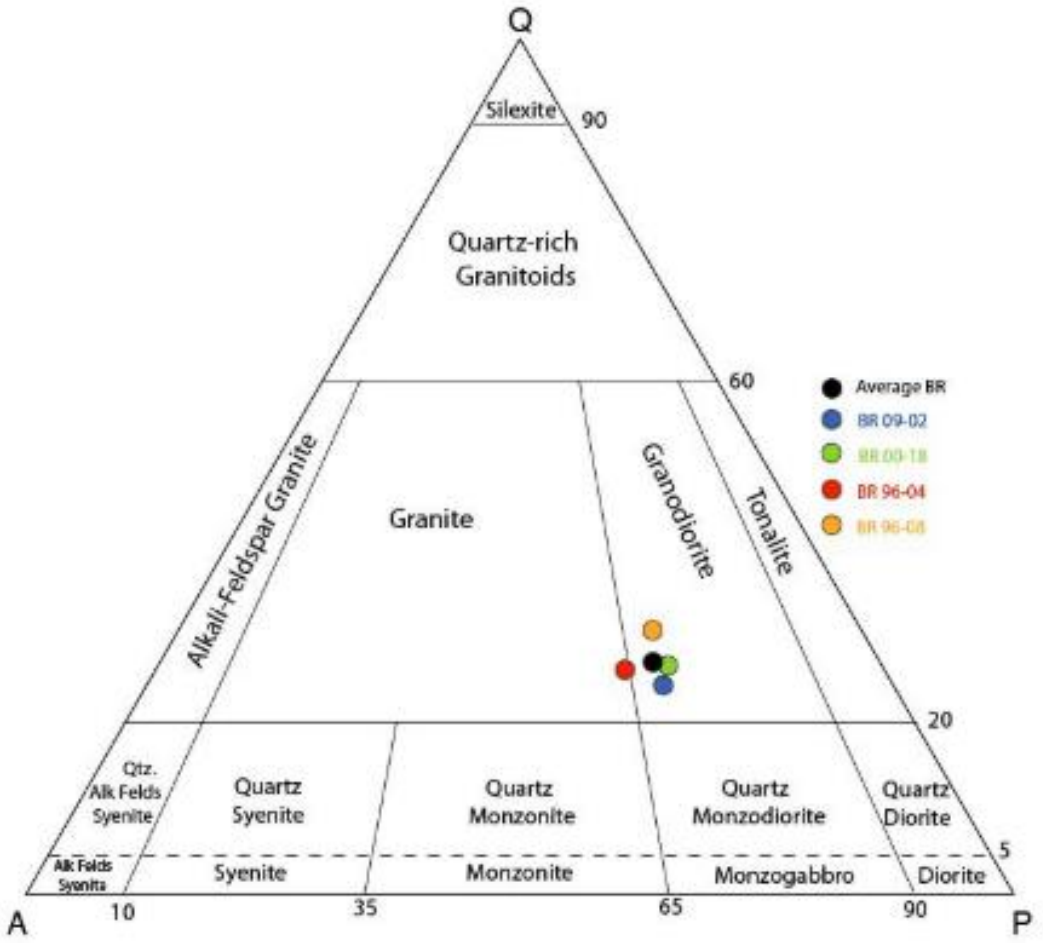
Appendix B 8. Values calculated for determining stepladder granite compositional name.

Sample	SiO2	A/CNK	A/NK	Fe #	ASI	MALI
0119SL_13	66.56	1.45	2.05	0.72	1.48	4.49
0119SL_0	72.94	1.48	1.84	0.73	1.50	5.80
0119SL_1	70.40	1.55	1.99	0.74	1.57	5.61
0119SL_2	69.36	1.59	2.01	0.73	1.61	5.77
0119SL_3	70.15	1.57	1.97	0.72	1.59	5.81
0119SL_4	71.75	1.58	2.04	0.71	1.62	5.38
0119SL_5	69.37	1.53	2.02	0.70	1.56	5.37
0119SL_6	71.11	1.47	1.84	0.75	1.50	6.27
0119SL_7	68.31	1.51	2.09	0.69	1.55	4.71
19_SL_2	69.85	1.50	1.87	0.77	1.53	6.55
ST09-02*	70.71	1.47	1.83	0.75	1.49	6.30
CF00-18*	71.84	1.45	1.86	0.71	1.48	5.84
Avg Bedrock	70.80	1.47	1.85	0.74	1.50	6.23
19_SL_5	13.51	0.08	1.96	0.61	0.08	-41.86
CF00-01*	26.02	0.06	3.90	0.19	0.06	-30.82
Avg Caliche	19.77	0.07	2.36	0.28	0.07	-36.34

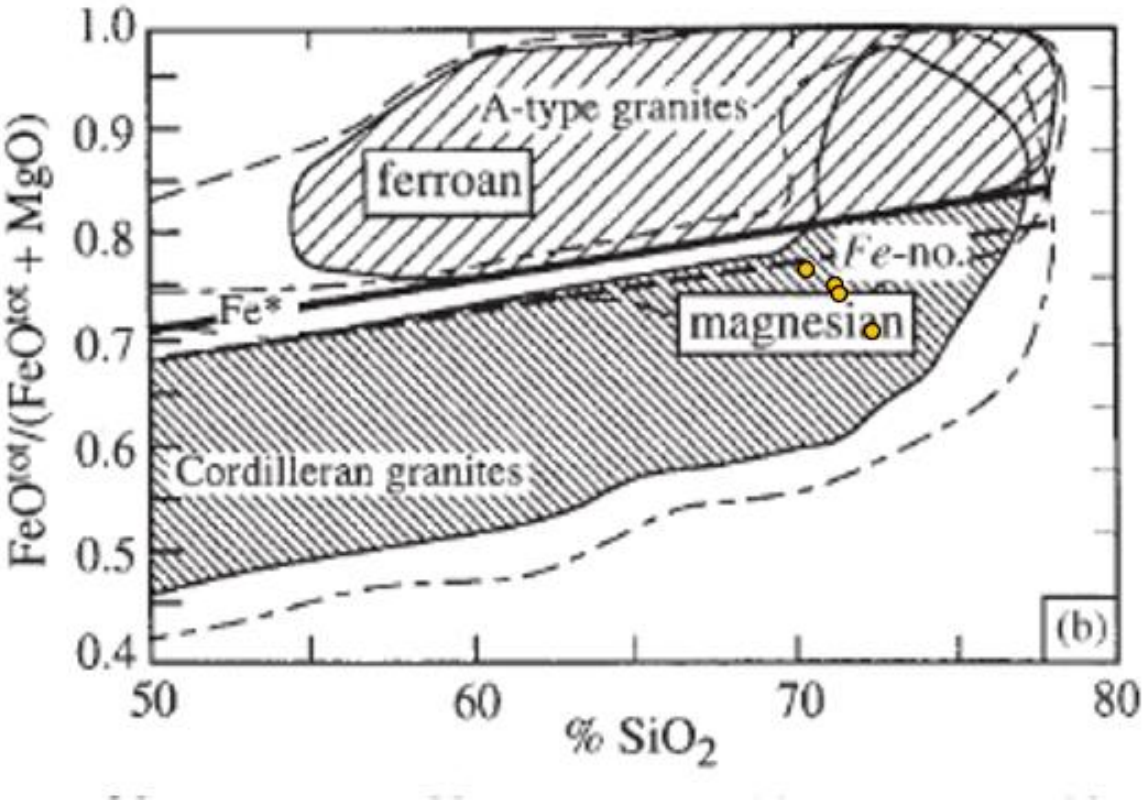
Appendix B 9. Bedrock normalized (BN) REE values for stepladder weathering profile, grus and caliche. † indicates values from Modi (2011).

		Eu/Eu^*_{BN}	$LREE_{BN}$	$HREE_{BN}$	Ce/Ce^*_{BN}
Grus	0119SL_13	0.94	0.93	0.86	1.28
Weathering Profile	0119SL_0	1.20	0.92	1.32	1.29
	0119SL_1	0.99	1.20	1.00	1.32
	0119SL_2	1.13	1.06	1.32	1.20
	0119SL_3	1.16	1.07	1.24	1.39
	0119SL_4	1.10	0.94	1.13	1.32
	0119SL_5	1.10	1.11	1.30	1.34
	0119SL_6	1.26	0.81	1.19	1.41
	0119SL_7	0.96	1.15	1.41	1.40
Caliche	19_SL_5	0.86	0.80	1.40	0.48
	CF00-01†	0.90	0.72	1.37	1.32
	Avg Caliche	0.87	0.77	1.39	0.79

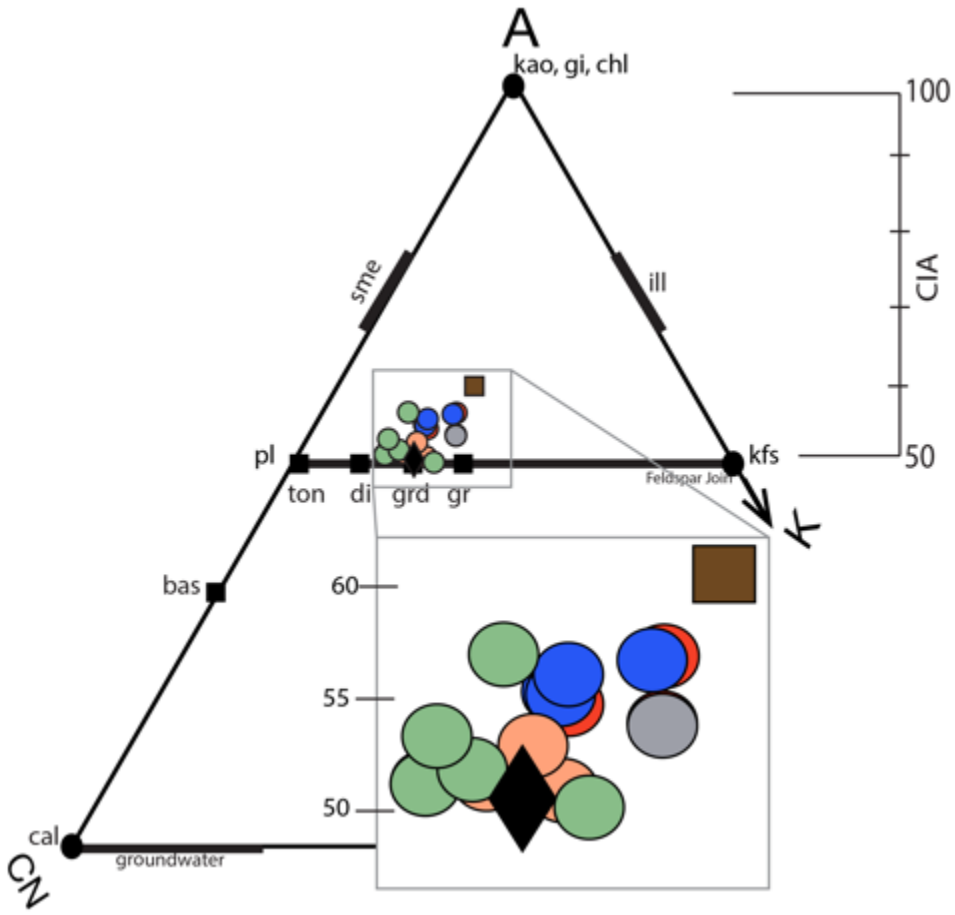
APPENDIX C
Supplementary Figures



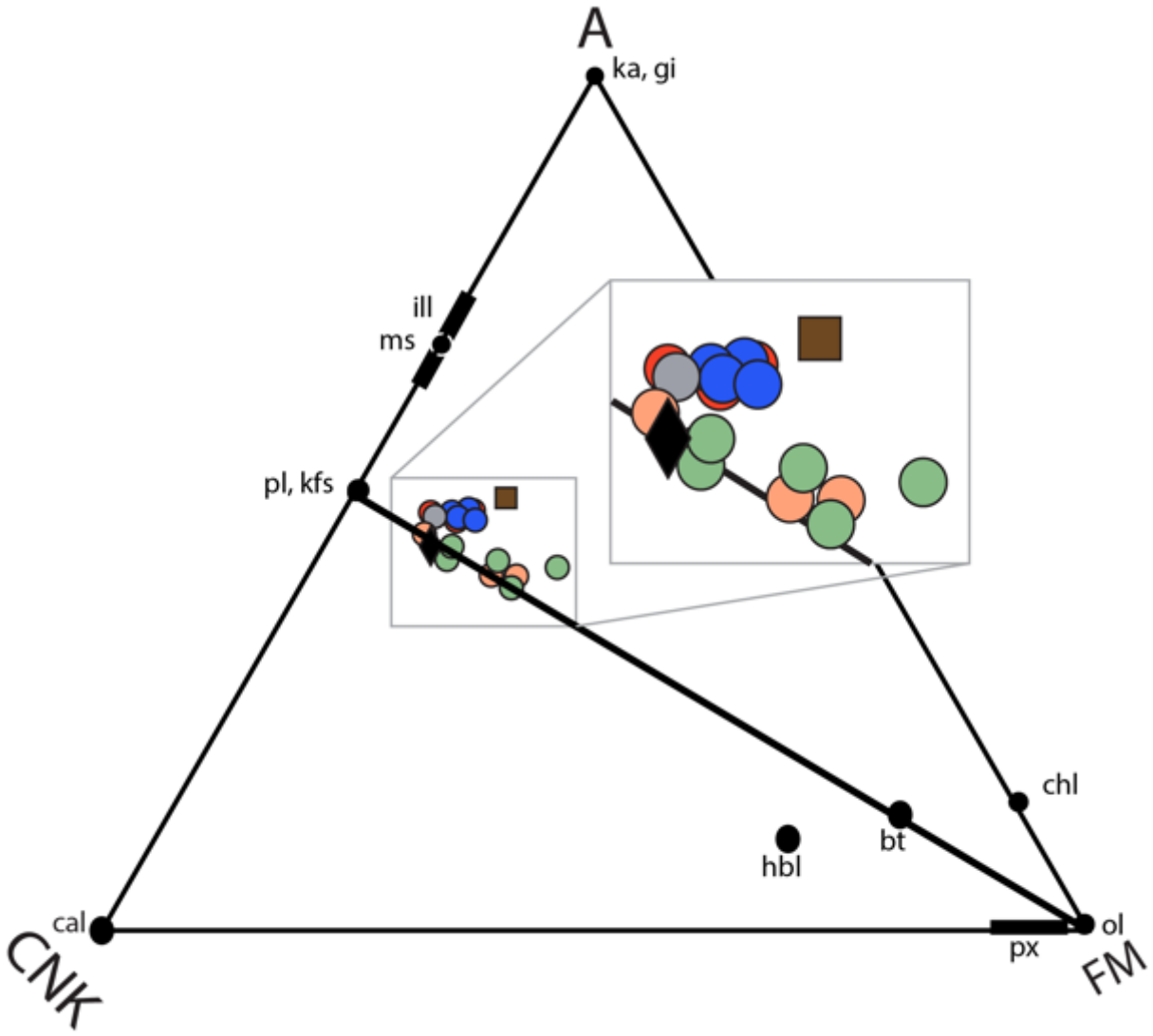
Appendix C 1. QAP diagram (Streckieson, 1976) showing bedrock composition for the Stepladder pluton. Figure from Modi (2011).



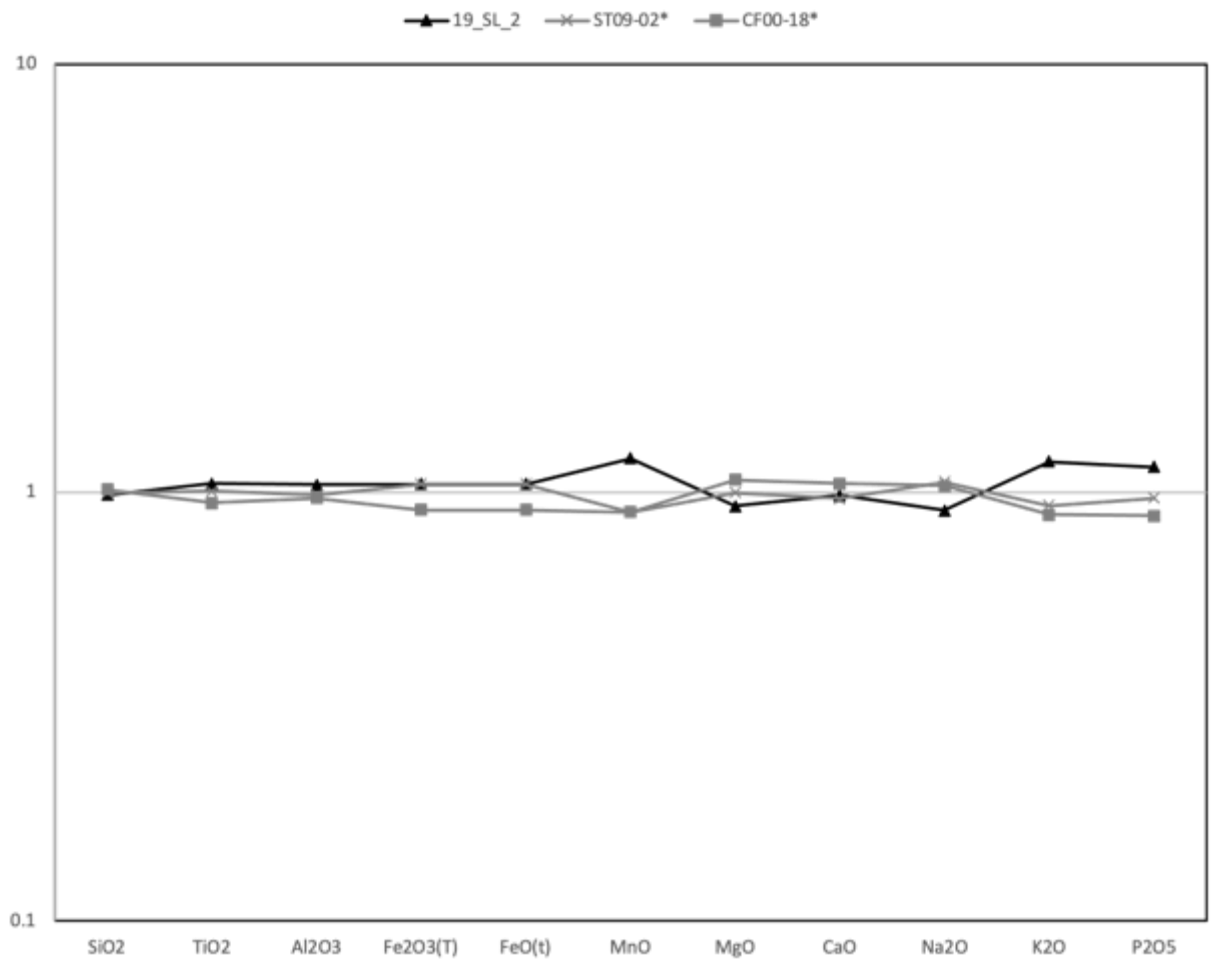
Appendix C 2. Granite type SiO_2 vs FeO.



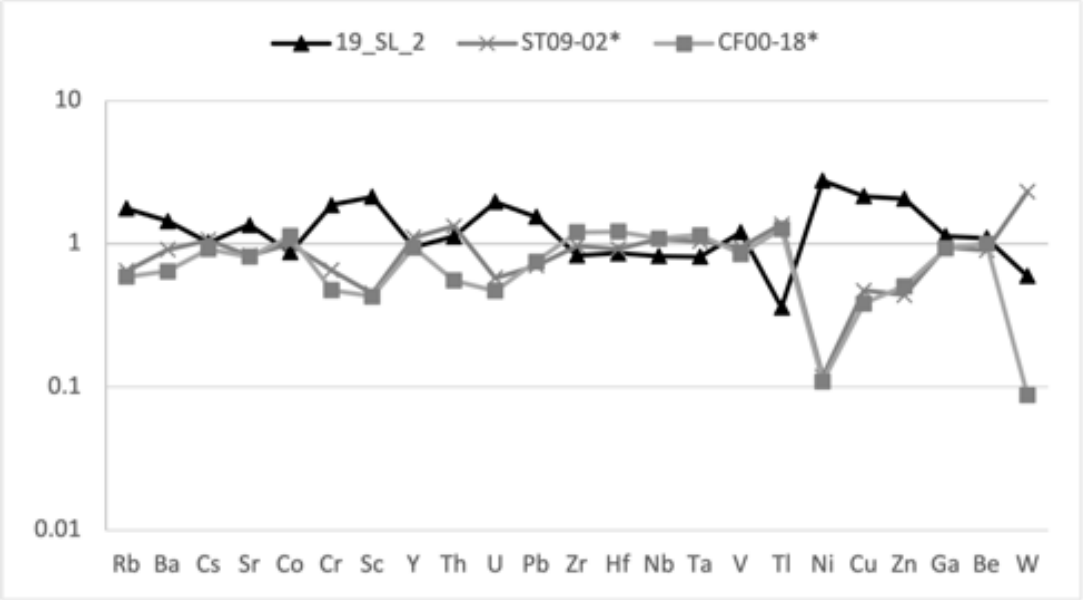
Appendix C 3. A-CN-K plot for sediment (Modi, 2011; Driscoll; 2016) and weathering profile data.



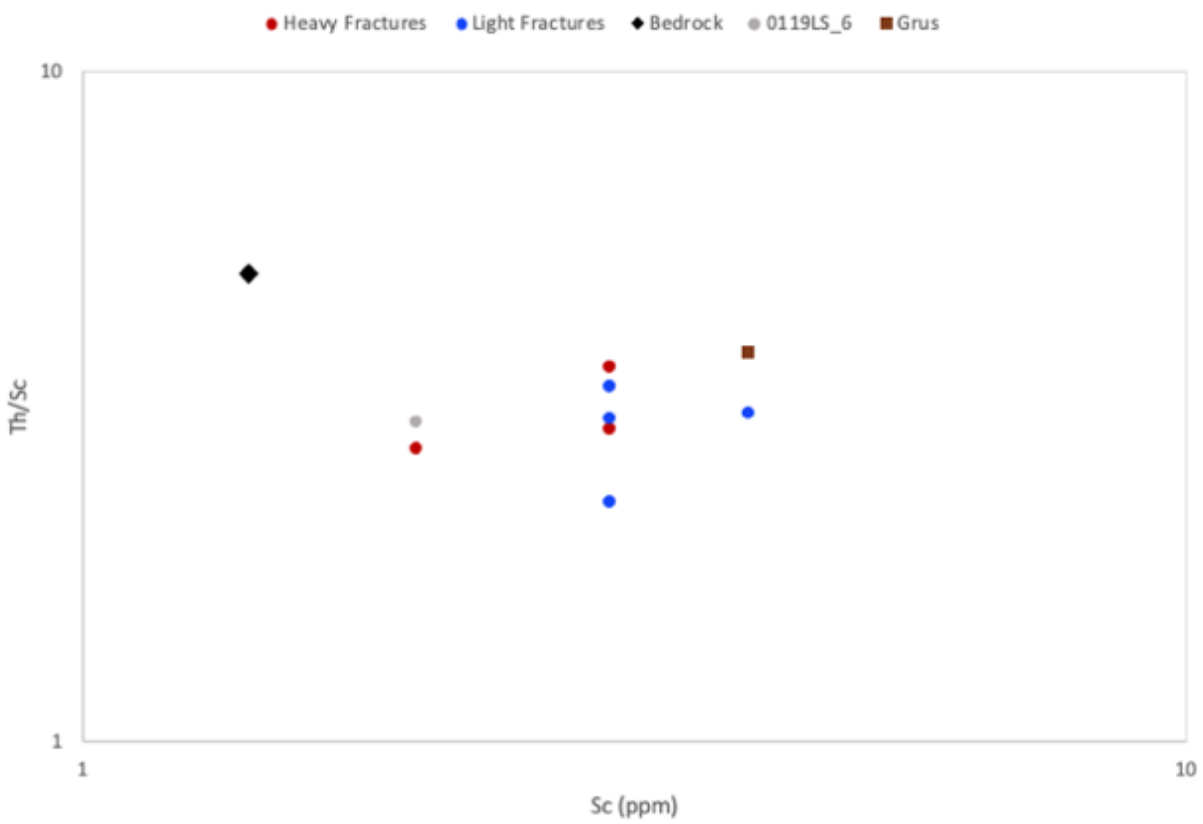
Appendix C 4. A-CNK-FM with Modi (2011) and Driscoll (2016) sediment values along with the weathering profile and grus from this study. Note the colors for weathering profile are in blue and red, matching low fracture density and high fracture density, respectfully. Sediment from Modi (2011) is in salmon and Driscoll (2016) is in light green. 0119SL_6 is in grey since no fracture density could be done on that sample.



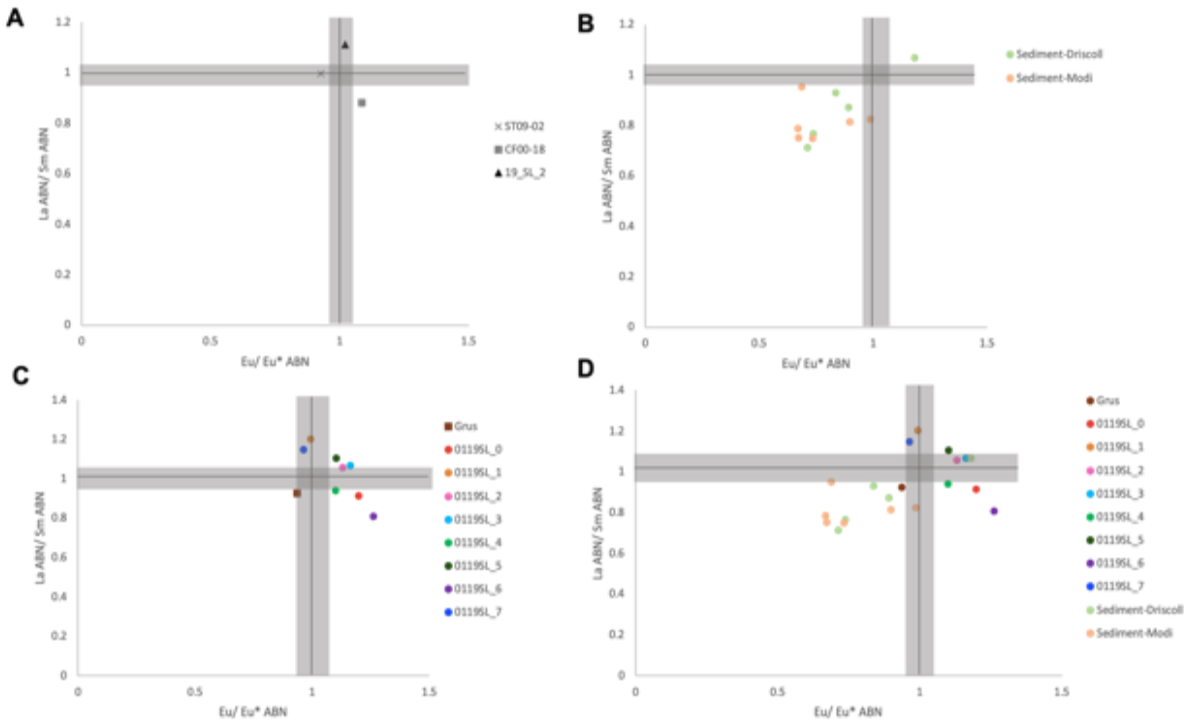
Appendix C 5. Average bedrock normalized bedrock REEs. * indicates samples from Modi (2011).



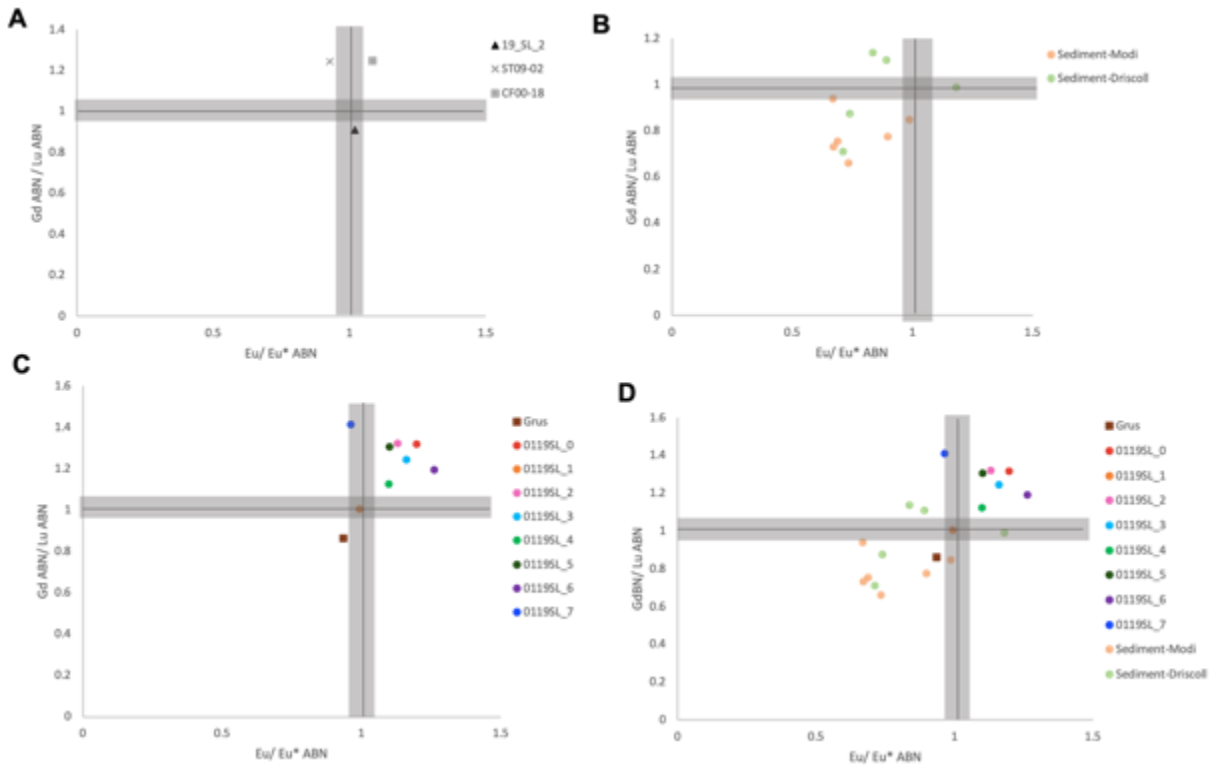
Appendix C 6. Average bedrock normalized bedrock values. Variation in samples is most likely due to values being at or near detection limits. * indicates samples from Modi (2011).



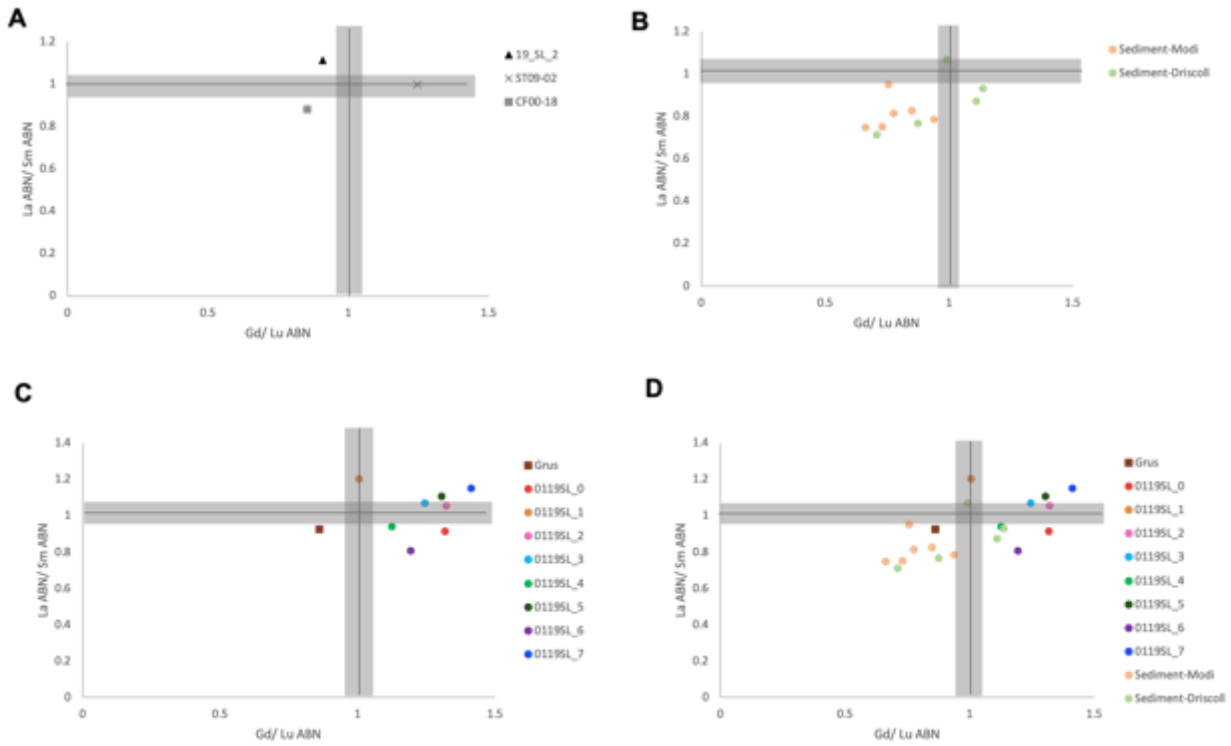
Appendix C 7. Th/Sc vs Sc trace-element plot. Note the colors for weathering profile are in blue and red, matching low fracture density and high fracture density, respectfully. 0119SL_6 is in grey since no fracture density could be done on that sample.



Appendix C 8. Eu/Eu* vs La/Sm for all sediment (Modi, 2011; Driscoll; 2016) and weathering profile data.



Appendix C 9. Eu/Eu* vs Gd/Lu for all sediment (Modi, 2011; Driscoll; 2016) and weathering profile data.



Appendix C 10. Gd/Lu vs La/Sm for all sediment (Modi, 2011; Driscoll; 2016) and weathering profile data.

VITA

Kristan L Watkins was born in November of 1995 in Redlands, California. She graduated high school in 2013 from Citrus Valley High School in Redlands, CA, and was among the first four-year graduating class. She was accepted into San Diego State University to pursue a Bachelor of Science degree in geology and graduated with cum laude honors in 2018. While at San Diego State, she was an undergraduate researcher focused on sedimentology. This research experience led her to the University of Tennessee, Knoxville, to pursue a Master of Science degree in the Department of Earth and Planetary Sciences working with Dr. Chris Fedo. She defended her thesis in December of 2021, and received a M.S. degree in Geology.